Stony Brook University

Investigations of Non-noble Metal Based Oxynitrides and Nitrides as Electrocatalysts for Oxygen Reduction Reaction and Hydrogen Evolution Reaction

A Dissertation Presented

by

Bingfei Cao

to

The Graduate School

in Partial Fulfillment of the

Requirements

for the Degree of

Doctor of Philosophy

in

Chemistry

Stony Brook University

August 2014

Stony Brook University

The Graduate School

Bingfei Cao

We, the dissertation committee for the above candidate for the

Doctor of Philosophy degree, hereby recommend

acceptance of this dissertation.

Peter G. Khalifah – Dissertation Advisor
Professor, Department of Chemistry

Stanislaus S. Wong - Chairperson of Defense
Professor, Department of Chemistry

John B. Parise – Third Member of Academic Committee
Professor, Department of Chemistry and Geosciences

Dario Stacchiola– Outside Member
Associate Chemist, Chemistry Department, Brookhaven National Laboratory

This dissertation is accepted by the Graduate School

Charles Taber
Dean of the Graduate School

Abstract of the Dissertation

Investigations of Non-noble Metal Based Oxynitrides and Nitrides as Electrocatalysts for Oxygen Reduction Reaction and Hydrogen Evolution Reaction

by

Bingfei Cao

Doctor of Philosophy

in

Chemistry

Stony Brook University

2014

Hydrogen fuel cells are expected to be a key energy conversion technology in the future due to their high efficiency. However, traditional Pt electrocatalysts used in fuel cells are limited in both their cost and availability. It is therefore desirable to develop non-noble metal cathode catalysts as alternatives for the oxygen reduction reaction (ORR) of fuel cells. In this study, binary and ternary molybdenum oxynitrides and nitrides have been designed as electrocatalysts for ORR in fuel cells.

Ammonia-treated carbon-supported cobalt molybdenum oxynitrides ($Co_xMo_{1-x}O_yN_z/C$) with rock salt structure have been investigated. These oxynitrides show moderate activity in acidic electrolyte and excellent activity in alkaline electrolyte. It is found that synthesis temperature and composition impact the catalytic activity. $Co_{0.50}Mo_{0.50}O_yN_z/C$ treated at 823 K exhibits the highest ORR activity in both electrolytes. This oxynitride demonstrates reasonable stability during long-term operation in either medium. X-ray diffraction (XRD), X-ray absorption spectroscopy (XAS) and transmission electron microscopy (TEM) studies indicate that ionic

cobalt is doped into the rock salt structure, though some metallic cobalt is also produced as a byproduct during the ammonolysis. The formation of bimetallic cobalt molybdenum oxynitride is responsible for the ORR activity.

The ORR activities of binary molybdenum nitrides with two different crystal structures illustrate that hexagonal molybdenum nitrides (δ-MoN and Mo_5N_6) exhibit enhanced activity over Mo_2N with the rock salt type cubic structure. In order to further enhance the activity, bimetallic $Co_{0.6}Mo_{1.4}N_2$ was synthesized via a two-step solid state reaction. This hexagonal ternary nitride contains four-layered stacking sequence with alternating layers of transition metals in octahedral and trigonal prismatic coordination. The octahedral sites contain a mixture of divalent Co and trivalent Mo, while the trigonal prismatic sites contain Mo with a higher oxidation state. $Co_{0.6}Mo_{1.4}N_2$ shows a better ORR activity than δ-MoN. In addition, $Co_{0.6}Mo_{1.4}N_2$ is demonstrated to be a highly active and stable electrocatalyst for hydrogen evolution reaction (HER) in acid solution.

Dedicated to My Parents

Table of Contents

List of Figures

List of Tables

List of Abbreviations

AFC	Alkaline fuel cell
CV	Cyclic voltammetry
DFT	Density functional theory
DMFC	Direct methanol fuel cell
DOS	Density of states
EDX	Energy-dispersive X-ray spectroscopy
EELS	Electron energy loss spectrometer
EXAFS	Extended X-ray absorption fine structure
GC	Glassy carbon
HER	Hydrogen evolution reaction
HOR	Hydrogen oxidation reaction
LDOS	Local density of states
MCFC	Molten carbonate fuel cell
ORR	Oxygen reduction reaction
PAFC	Phosphoric acid fuel cell
PEMFC	Proton exchange membrane fuel cell
PTFE	Polytetraluroroethylene
RDE	Rotating disk electrode
RRDE	Rotating ring-disk electrode
SEM	Scanning electron microscopy

SOFC	Solid oxide fuel cell
STEM	Scanning transmission electron microscopy
TEM	Transmission electron microscopy
TDOS	Total density of states
XANES	X-ray absorption near-edge structure spectroscopy
XRD	X-ray diffraction
XPS	X-ray photoelectron spectroscopy

Acknowledgments

First, I would like to thank my advisor Dr. Peter Khalifah for his guidance and support throughout my PhD career. Without his assistance, I would not complete any research project. I would also like to thank Dr. Stanislaus Wong and Dr. John Parise for their serving on committee.

I would also like to thank all my past and present fellow group members Dr. Limin Wang, Dr. Yuri Janssen, Dr. Polina Burmistrova, Andrew Malingowski, Alexandra Reinert, Diane Colabello, Shujie Hu, Shouhang Bo, Jue Liu, Xiaoya Wang, Huafeng Huang and Jeffery Ma for offering invaluable assistance during my research. It has been a pleasure to work within the group.

I would like to express my gratitude to Dr. Radoslav Adzic's research group in Brookhaven National Laboratory for sharing their expertise in electrochemistry. I would like to acknowledge Dr. Gabriel Veith for XPS measurements; Dr. Joerg Neuefeind and Dr. Mikhail Feygenson for neutron diffraction measurements; Dr. Rosa Diaz and Dr. Eric Stach for TEM experiments.

I am extremely grateful to all of my friends for their continous encouragement and support. Special thanks to Yu Zhang for providing me insightful ideas and sharing these five years with me, to Shujie Hu for her encouragement and discussions during lunch time, to Chloe Gu and Junyan Xie for all the joyous trips in the US.

Finally, I would like to thank my parents for their trust, love and understanding over the past six years.

Publications

B.Cao, G.Veith, J. Neuefeind, R. Adzic, P. Khalifah, *J. Am. Chem. Soc*. **2013**, *135*, 19186.

B.Cao, G.Veith, R.Diaz, J.Liu, E.Stach, R.Adzic, P.Khalifah, *Angew. Chem. Int. Ed.* **2013**, *52*, 10753.

L.Wang, **B.Cao**, W.Kang, M.Hybertsen, K.Maeda, K.Domen, P.Khalifah, *Inorg. Chem.* **2013**, *52*, 9192.

Q.Mi, Y.Ping, Y. Li, **B.Cao**, B.Brunschwig, P.Khalifah, G.Galli, H.Gray, N.Lewis, *J. Am. Chem. Soc*. **2012**, *134*, 18318.

B.Cao, R. Adzic and P.Khalifah, *In Preparation*

B.Cao, D. Weinstain, B. Klobes, R. Hermann, K. Maeda, K. Domen and P. Khalifah, *In Preparation*

Chapter 1. Introductions

1.1 Fundamentals of Fuel Cells

Fossil fuels currently represent the major energy resource for worldwide consumption. However, fossil fuel is non-renewable and its supplies are not easily accessible. It is critical and important to reduce the use of oil and migrate alternative clean and sustainable energy sources. Fossil fuels have been extensively used to power automobiles. A transition from combustion engine powered automobiles to electric vehicles is an important step to sustain the current living standard.[1-3] A pure electric vehicle requires a good energy storage and conversion ability. Renewable technologies for energy storage and conversion, such as lithium batteries and fuel cells, have been developed rapidly in recent years.[3-5] Although lithium ion batteries have been intensively studied, the maximum specific energy density of current Li ion battery is limited to about 150 Wh/kg which severely limits the driving range of electric vehicles.[3] Hydrogen fuel cells have high theoretical energy density and are the most promising candidate to replace internal combustion engines in vehicles. Hydrogen fuel cells can be highly efficient since they involve electrochemical reactions rather than combustion. Hence, it is important to develop fuel cell powered automobiles for future applications.

Both batteries and fuel cells are devices that convert chemical energy to electrical energy via redox reactions. The major difference between battery and fuel cell is the compartment to store and convert energy. Typical lithium ion batteries have a closed structure, with the anode and cathode being active materials in the redox reaction. Energy storage and conversion occur in the same locations in the battery. In contrast, fuel cell has an open structure, with the anode and cathode only being the charge transfer media. The typical active materials of H_2 and O_2 are provided from the outside of the cell. The separation of energy storage and conversion aids the

high theoretical energy density of fuel cells. The high energy conversion efficiency and low environmental impact of fuel cells make them advantageous to replace combustion engines with fuel cells in the future.

1.1.1 Thermodynamics and Kinetics of Fuel Cells

All fuel cells have similar basic components and working principles. Fuel cells contain an anode, a cathode and an electrolyte which separates the two electrodes. Reactions at the anode usually take place at lower potentials than that at the cathode. The fuel (such as H_2 or methanol) is oxidized at the anode while the oxidant (O_2 or air) is reduced at the cathode. Electrons produced at the anode are transferred to the cathode through the external circuit. The redox reactions in fuel cells are spontaneous reactions. With the help of electrocatalysts, the chemical energy is converted into electrical energy in the form of an electric current. The electrochemical reactions follow the thermodynamic and kinetic rules of chemical reactions. The change in Gibbs free energy (ΔG) is equal to the negative of the electrochemical work (W_e) in a fuel cell.[6]

$$\Delta G = -W_e = -n_e FE \quad (1.1)$$

where n_e is the number of electrical charges transferred in the reaction (electron or proton), F is the charge carried by a mole of electrons (Faraday constant, 96485 A s/mol), E is the potential difference between the electrodes.

For a cell reaction occurring at constant temperature and pressure:

$$a\mathrm{A} + b\mathrm{B} \rightarrow m\mathrm{M} + n\mathrm{N} \quad (1.2)$$

The change in the Gibbs energy can be expressed as:

$$\Delta G = \Delta G^\circ + RT\ln\frac{[\mathrm{M}]^m[\mathrm{N}]^n}{[\mathrm{A}]^a[\mathrm{B}]^b} \quad (1.3)$$

where $\Delta G°$ is the standard Gibbs free energy, [A], [B], [M] and [N] is the concentration of species A, B, M and N. By substituting Equation (1.3) onto (1.1), the Nerst equation (1.4) is obtained:

$$E = E° - \frac{RT}{n_e F} \ln \frac{[M]^m [N]^n}{[A]^a [B]^b} \quad (1.4)$$

In a hydrogen fuel cell, the net reaction is

$$H_2 + ½\ O_2 \rightarrow H_2O \quad (1.5)$$

Two electrons are transferred in the reaction, so $n_e = 2$. Equation (1.4) can be written as

$$E = E° - \frac{RT}{2F} \ln \frac{P_{H2O}}{P_{H_2} P_{O_2}^{1/2}} \quad (1.6)$$

When the reaction reaches its equilibrium, the ideal potential $E°$ equals 1.23 V with liquid water product. From equation (1.6), diluting reactant gases will lower the fuel cell voltage. For example, if air is used as the reactant, the mole fraction of oxygen gives a smaller cell potential than 1.23 V.[7]

Thermodynamics describes the reaction at the equilibrium. The redox reaction in fuel cell occurs at the interface of the electrode and electrolyte. The electrical charge must overcome an activation energy barrier to move across the interface. The energy barrier determines the rate of the reaction. The kinetics of the electrochemical reaction can be understood based on the transition state theory.[7] For a redox reaction

$$Red \leftrightarrow Ox + ne^- \quad (1.7)$$

The rate of the charge-transfer-controlled reaction above can be described by the Butler-Volmer equation as

$$j = j_0 [\exp(\frac{n(1-\alpha)F\eta}{RT}) - \exp(\frac{-n\alpha F\eta}{RT})] \quad (1.8)$$

where j_0 is the exchange current density, $j_0 = k_0nFC$ (k_0 is the reaction rate constant, C is the concentration of reactants), n is the number of electrons involved in the reaction, η is the overpotential beyond the equilibrium potential ($\eta = E - E_{eq}$), and α is the transfer coefficient, which can be considered as the fraction of the change of overpotential that leads to a change in the rate constant for charge-transfer reaction.[4,7] When the overpotential is positive, the oxidation component is large and the reduction component is small. The net current density is positive meaning the oxidation reaction (forward reaction in Equation 1.7) is favorable. When the overpotential is negative, the reduction reaction takes place. The exchange current density is defined as the current that flows equally in both directions at equilibrium. When the reaction is on equilibrium, the net current density and overpotential are zero. The exchange current density is directly related to the kinetic terms. Therefore, it can be used to compare different catalysts. Generally, catalysts with a larger j_0 have a smaller activation energy which is the origin of the faster rate.

For large overpotentials ($|\eta| >> RT/nF$), the Tafel equation can be derived as follows

$$j = j_0[\exp(\frac{n(1-\alpha)F\eta}{RT})] \quad \text{anode (1.9)}$$

$$j = j_0[-\exp(\frac{-n\alpha F\eta}{RT})] \quad \text{cathode(1.10)}$$

In a Tafel plot, $\log|j|$ versus overpotential (η) has a linear relationship. The slope is $(1-\alpha)nF/RT$ for anodic reaction and $\alpha nF/RT$ for cathodic reactions. The exchange current density, j_0, can be calculated from the intercept of y-axis .

1.1.2 Performance of Fuel Cells

Besides the activation polarization, other factors influencing the performance of fuel cells include Ohmic polarization and concentration polarization (Figure 1.1). Ohmic polarization

arises from the resistance of electrode materials and electrolyte. According to the Ohm's Law, the relationship between current and overpotential is linear. The larger the resistance, the faster the drop of the voltage with increasing current density. As the redox reactions proceed, the active sites at the electrode-electrolyte interface are occupied by reactant species. The concentration difference between bulk electrolyte and electrode surface results in the concentration polarization. The voltage loss is due to active species not being able to reach the active site and to replace the reacted materials to sustain the reaction. At low currents, the performance of the fuel cell is dominated by kinetic losses of cathodic and anodic reactions. The buidup and decay of kinetic polarization is fast.[4] At intermediate currents, the ohmic losses are dominant. At high currents, limiting mass transport becomes important. The diffusion limitations are relatively slow.

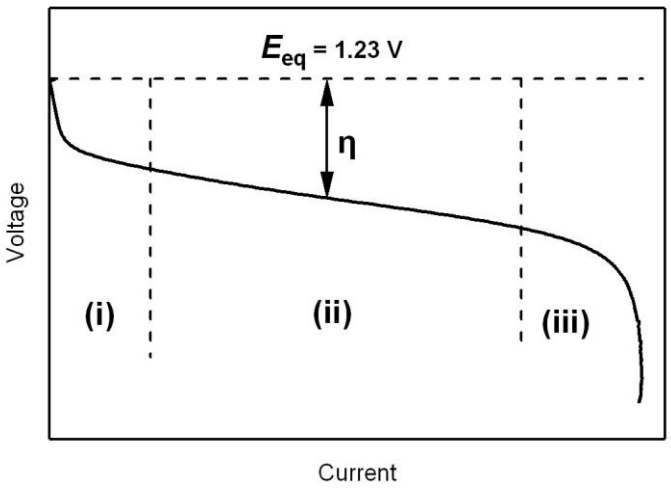

Figure 1.1 Typical polarization curve of a fuel cell, showing the influence of various types of polarization: (i) kinetic polarization; (ii) ohmic polarization; (iii) concentration polarization.

In order to improve the power efficiency, it is important to minimize the overall overpotential. One main factor controlling the activation overpotential is exchange current density j_0. Electrocatalyst with a large j_0 gives a higher onset cell potential and a lower

overpotential. The magnitude of j_0 can be increased by loading more electrocatalyst within the economic limitation. Ohmic losses can be minimized by enhancing the electric conductivity of the electrode materials, the ionic conductivity of electrolyte and the contact between catalyst layer and electrode surface. Porous electrodes are typically used in fuel cells to increase their surface area and enhance their efficiency.

1.1.3 Classification of Fuel Cells

Fuel cells are classified into six types according to their different types of electrolyte (Table1.1).[4,7,8] Alkaline fuel cells (AFC), proton exchange membrane fuel cells (PEMFC), direct methanol fuel cells (DMFC) and phosphoric acid fuel cells (PAFC) are operated at low temperatures. Molten carbonate fuel cells (MCFC) and solid oxide fuel cells (SOFC) are operated at relatively high temperatures.

Table 1.1 Classes of fuel cell systems.[4,7,8]

	AFC	PEMFC	DMFC	PAFC	MCFC	SOFC
Operating temp. (°C)	60-150	60-90	60-90	180-220	650-700	800-1000
Electrolyte	aqueous KOH	ion exchange membrane	ion exchange membrane	H_3PO_4	molten Li_2CO_3	yttria-stabilized zirconia
Charge carrier	OH^-	H^+	H^+	H^+	CO_3^{2-}	O^{2-}
Fuel	H_2	H_2	CH_3OH	H_2	H_2	gasoline
Cathode reaction	$O_2 + 2H_2O + 4e^- \rightarrow 4OH^-$	$O_2 + 4H^+ + 4e^- \rightarrow 2H_2O$	$O_2 + 4H^+ + 4e^- \rightarrow 2H_2O$	$O_2 + 4H^+ + 4e^- \rightarrow 2H_2O$	$O_2 + 2CO_2 + 4e^- \rightarrow 2CO_3^{2-}$	$O_2 + 4e^- \rightarrow 2O^{2-}$

One major advantage of high temperature fuel cell is that non-precious materials can be employed as electrode catalysts since the high operating temperature makes the reaction kinetics

faster. The overall efficiency for MCFC and SOFC can reach up to about 85%. In order to sustain the high operating temperature, the electrolytes of these fuel cells are immobilized liquids (molten Li_2CO_3 in $LiAlO_2$) or solid (yttria-stabilized or yttria-calcia-stabilized zirconia). These electrolytes have a high resistivity which inhibits the performance. The stability of electrode materials at high temperatures also remains a problem.

Compared to high temperature fuel cells, low temperature fuel cells are more suitable for practical applications. Small fuel cells in the range of 50 – 75 kW have been developed for use in automobile and bus propulsion.[4] The AFC is one of the oldest fuel cell types. Both noble metal and non-noble metal based catalysts are active in AFCs because hydrogen and oxygen kinetics are more facile in alkaline electrolyte which permits a higher cell voltage for AFC. However, AFC is susceptible to CO_2 inactivation since the electrolyte (KOH) reacts with CO_2 to form K_2CO_3. Only pure H_2 and O_2 can be used as the fuel feeds. AFC stacks have been developed to provide electric power for space shuttle applications.

Both PEMFC and DMFC are using unique ion exchange membranes as electrolytes which only allows proton to pass through the membrane. The solid electrolyte reduces the corrosion and water management problems. Moreover, the cell structures have good mechanical integrity under compression and expansion from temperature and pressure gradient during operation. The anode fuel for PEMFCs is H_2 while methanol is the fuel for DMFCs. One of the main advantages of DMFCs is that it is easy to store and transport the liquid methanol fuel. There is no need to convert the hydrocarbon fuel into hydrogen fuel. The anode catalyst (Pt-Ru) requires a high loading for methanol oxidation which involves a complicated $6e^-$ process compared to hydrogen oxidation ($2e^-$). DMFC has a low overall efficiency and it yields only ~ 0.5 V at 400 mA/cm^2 at 60°C.[4] In contrast, PEMFCs have a high power density and the cell

output is 0.7 V at ~1 A/cm^2.[4] This system has a minimal material problems though the costs for the catalyst and membrane are high. In addition, H_2S and CO impurities need to be eliminated to prevent catalyst poisoning for long-term operation.

The PAFC is another fuel cell employing acid media. This cell type is commercially available nowadays. The electrolyte is concentrated phosphoric acid in a silicon carbide matrix. The concentrated acidic solution is stable below 220°C and water management problems are reduced in this cell. When the temperature is below 150°C, the ionic conductivity of H_3PO_4 is poor. The operating temperature is therefore 150-200°C to maintain the cell efficiency.[4] The cell output for a existing PAFCs can reach 200 kW.[4]

1.2 Electrocatalysis in Fuel Cells

In hydrogen fuel cells, H_2 is oxidized at the anode and O_2 is reduced at the cathode. Compared to $2e^-$ hydrogen oxidation reaction (HOR), the oxygen reduction reaction (ORR) involves a more complicated $4e^-$ process. The exchange current density for ORR is ~10^{-10} A/cm^2 in acid and ~10^{-8} A/cm^2 in alkaline which are much lower than the value for the HOR (~10^{-3} A/cm^2).[9] Since ORR has a sluggish kinetics and higher overpotential, it is more important to investigate good cathode catalyst to facilitate the ORR reaction. The essential criteria for a good cathode catalyst include good catalytic activity, high electronic conductivity, chemical and structural stability, tolerant to contaminants and low cost.

1.2.1 Oxygen Reduction Reaction Pathways

Depending on the types of electrolyte and electrocatalyst, different mechanistic pathways for the ORR will occur. The ORR pathways include either a direct four-electron pathway and/or an indirect two-electron reduction followed by a further two-electron reduction. The indirect

pathway generates peroxide as a final byproduct or as an intermediate which will be further reduced into H_2O or OH^-.[10-13]

In acid electrolyte, the direct reaction is shown as reaction 1.11

$$O_2 + 2e^- + 2H^+ \rightarrow 2OH_{ads}$$

$$2OH_{ads} + 2e^- + 2H^+ \rightarrow 2H_2O$$

$$\text{Overall: } O_2 + 4e^- + 4H^+ \rightarrow 2H_2O,\ E° = 1.23 \text{ V vs. NHE} \qquad (1.11)$$

The indirect pathway follows reaction 1.12

$$O_2 + e^- + H^+ \rightarrow HO_{2,ads}$$

$$HO_{2,ads} + e^- + H^+ \rightarrow H_2O_2$$

$$\text{Overall: } O_2 + 2e^- + 2H^+ \rightarrow H_2O_2,\ E° = 0.682 \text{ V vs. NHE} \qquad (1.12)$$

H_2O_2 can be further reduced into H_2O

$$H_2O_2 + 2e^- + 2H^+ \rightarrow H_2O,\ E° = 1.77 \text{ V vs. NHE} \qquad (1.13)$$

In alkaline electrolyte, the direct pathway is

$$O_2 + 2e^- + 2H_2O \rightarrow 2OH_{ads} + 2OH^-$$

$$2OH_{ads} + 2e^- \rightarrow 2OH^-$$

$$\text{Overall: } O_2 + 4e^- + 2H_2O \rightarrow 4OH^-,\ E° = 0.401 \text{ V vs. NHE} \qquad (1.14)$$

The formation of H_2O_2 in alkaline is

$$O_2 + e^- + H_2O \rightarrow HO_{2,ads} + OH^-$$

$$HO_{2,ads} + e^- \rightarrow HO_2^-$$

$$\text{Overall: } O_2 + 2e^- + H_2O \rightarrow HO_2^- + OH^-,\ E° = -0.076 \text{ V vs. NHE} \qquad (1.15)$$

HO_2^- is reduced into OH^- as follows

$$HO_2^- + 2e^- + H_2O \rightarrow 3OH^-,\ E° = 0.88\ V\ vs.\ NHE \qquad (1.16)$$

The O-O bond in O_2 is stable with a high dissociation energy of 494 kJ/mol. It is necessary to use catalyst to rapidly break O-O bonds at or near room temperature. The ORR reaction occurs on the surface of the electrocatalyst. The O_2 adsorption sites and geometry on the electrode surface impact its ORR pathway. There are three possible configurations by which O_2 interacts with a metal. The Griffiths model involves a side-on interaction with single metal atom through two bonds.[14] The Pauling model involves an end-on interaction with single atom through a single bond.[15] In the Yeager model, the O_2 is adsorbed on two sites (bridge or trans interaction).[16] The Griffiths and Yeager configurations lead to a direct reduction with little or no peroxide formation while the Pauling configuration leads to the formation of peroxide.

Various authors have proposed different schemes for ORR pathways. Adzic *et al.*[13] have proposed a classification scheme to describe the complicated reaction pathways. It is defined as

(i) a direct four-electron reduction of O_2 without H_2O_2 detected on the ring electrode;

(ii) a two-electron reduction of O_2 into peroxide;

(iii) a series pathway with two- and four-electron reduction;

(iv) a parallel pathway which combines pathway (i), (ii) and (iii);

(v) an interactive pathway in which diffusion of species from a series pathway to a direct pathway is possible.

On most electrocatalysts, the ORR occurs via the initial formation of H_2O_2 followed by further reduction to H_2O. This is probably due to the lower dissociation energy of O_2 relative to H_2O_2 (146 kJ/mol).[17] In order to avoid corrosion caused by H_2O_2 of carbon supports or other fuel cell components, the four-electron direct pathway is desired. Therefore, it is important to design suitable catalysts that promote four-electron ORR reaction pathways.

1.2.2 Catalyst in Proton Exchange Membrane Fuel Cell (PEMFC)

The proton exchange membrane fuel cell (PEMFC), also called the polymer electrolyte membrane fuel cell, was first developed by General Electric in 1960's for use on space vehicles.[8] The polymer electrolyte works at low temperatures which allows a quick start-up for the PEMFCs. The use of a membrane means it is possible to make compact fuel cells. Other advantages include no corrosive fluids and flexible working configuration. These features enable the use of PEMFCs in transportation and portable device applications. PEMFCs are being actively developed for use in automobiles, portable electronics, and in combined heat and power systems. They are potential power sources with outputs ranging from a few watts to hundreds of kW.

In each PEMFC within a cell stack, there is an ion exchange membrane, the electrode/electrocatalyst, a conductive porous backing cloth and bipolar plates connecting cells in series. The cell stack contains multiple unit cells to achieve the desired voltage. For a wide range of applications, the preferred electrolyte, electrode structure, and the catalyst are similar.

The early versions of PEMFCs, as used in spacecraft, only had a lifetime of 500 hours.[8] A new polymer membrane called Nafion was developed by Dupont and became a new standard for PEMFCs. Nafion membranes consist of stable polytetrafluoroethylene (PTFE) backbones and sulfonic acid side chains (HSO_3) attached to the backbone (Fig. 1.2). The strong bonding between fluorine and carbon in PTFE makes it resistant to chemical attack. It is also hydrophobic which drives the product water out of the electrode and prevents flooding problems. The HSO_3 group is ionically bonded to the PTFE and the end of the side chain is an SO_3^{2-} ion. Since sulphonic acid is hydrophilic, the hydrated regions are generated around sulphonated side chain clusters. Within these hydrated regions, H^+ ions can move freely. Therefore, Nafion membrane

works as a proton conductor while also prevents the transport of anions. The membrane electrode assembly (MEA) is usually thinner than a few hundred micrometers, allowing cells to generate a voltage around 0.7 V and power density around 1 W/cm^2.

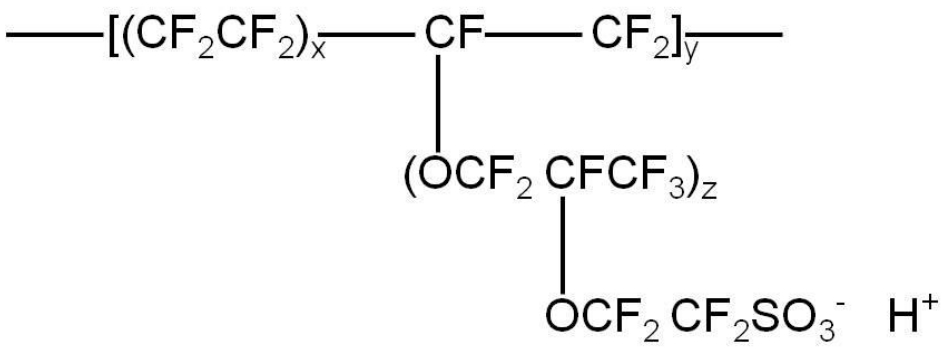

Figure 1.2 Structure of Nafion membrane.

Catalyst layers are present between the membrane and the backing cloth layer. The best catalyst is platinum. Ideally, small Pt particles are evenly dispersed onto the carbon supports, so that a high proportion of the surface area will be in contact with the reactants. Since Pt is a major factor responsible for the high cost of PEMFCs, two approaches have been taken to reduce the cost of cathode and enable a more widespread application of this technology. The first method is minimizing platinum amount in the catalyst layer. The second method is developing non-precious metal-based catalyst.

1.2.2.1 Noble Metal Based Catalyst

In the last two decades, the minimum required Pt loading has been reduced to 0.4 mg/cm^2.[18] The ORR activity is dependent on the particle size of Pt. Decreasing the particle size will increase the surface-area-to-volume ratio which is beneficial for catalysis. It is proposed that the point of zero charge on the Pt surface shifts 35 mV more negative by decreasing the particle size from 30 nm to 1 nm.[19] As a consequence, at the same potential, the surface coverage of

OH^- is higher for Pt with a smaller particle size. For ORR, the adsorbed OH^- ions act as blocking species and inhibit the reaction. Therefore, the Pt particle size can not be too small. The Pt nanoparticles with a size of 3 – 4 nm have the highest mass activity. [19]

Increasing Pt utilization can be achieved by alloying Pt with inexpensive transition metals (Co, Fe, Ni *etc*.) or by creating core-shell structured Pt nanoparticles. Alloying Pt results in two changes that may affect the activity of Pt alloys. First, alloying may change the electronic structure of platinum. Second, alloying may change the adsorption properties of platinum on the surface. The activity of binary Pt alloys was found to have a 2.4 – 3.6-fold increase in specific activity and a 2-3-fold increase in mass activity.[18,20] About 20 – 30 mV activity gains over Pt/C were obtained. According to the stability evaluation results, PtCr and PtTi did not show any apparent leaching while PtFe, PtMn and PtNi showed leaching of non-noble elements.[18] Alloying non-noble metals with other noble metals (Pd, Ru, Ir and Au) is another method to lower the cost. Pd based alloys show high ORR activity comparable to that of Pt/C. Pd-based alloys also have excellent methanol tolerance. However, the acidic stability of Pd alloys needs to be improved to meet industry needs.

Engineering Pt alloys to contain textured structures seems effective in improving the activity, stability and reducing the Pt amount.[21] Stamenkovic *et al*. prepared Pt_3M (M = Fe, Co and Ni) with three different surfaces.[22-24] Three surfaces are: (i) random surfaces containing randomly distributed Pt and *M* metals, (ii) Pt-skeleton surface containing 75 at.% Pt and 25 at.% *M*, (iii) Pt-skin surface containing 100 % Pt. It has been demonstrated that Pt alloys covered by a Pt-skin surface exhibit highest activity and durability. The noble-metal shell protects the core from contacting the acid electrolyte and prevents the core dissolution. The core substrate affects the catalytic properties of Pt shell by modifying its electronic structure and inducing surface

strain. Therefore, core-shell Pt nanostructure is a promising catalyst for ORR catalysis. The electrochemical properties of nanoparticles are dependent on the core composition and structure. Adzic *et al*. deposited Pt monolayers on various core structures to enhance and stabilize Pt and Pt-based alloys.[25] In order to synthesize the core-shell nanostructure, a Cu shell was first formed outside the core by under potential deposition. Pt monolayer was then deposited by galvanic displacement of Cu. Pt monolayers on 4 nm Pd and 4.6 nm Pd_3Co cores exhibited about 5- and 9-fold enhancement over 3 nm Pt nanoparticles. The enhancements can be attributed to the lattice contraction in (111) facets. These results demonstrate a way to tailor Pt core-shell structures by controlling the composition, size and shape of the core particles for improvements in ORR durability and activity.[26]

1.2.2.2 Non-noble Metal Based Catalyst

Numerous research efforts have focused on developing non-precious metal catalysts for PEM fuel cells. The most promising catalysts thus far are carbon supported macrocycles. Other non-noble metal electrocatalysts include transition metal chalcogenides, oxides, carbides and nitrides. Compared to Pt, increasing loading is not a significant cost issue for non-precious metal materials until the thickness of catalyst layer reaches 100 μm.[18] For a practical application of non-precious catalysts, DOE has set up the activity and stability goal for 2015. The ORR activity should reach a volumetric current density of 300 A/cm^3 at 0.8 V and the stability should reach 5000 hours.[27]

Carbon supported macrocycles (*M*-N_x/C) were synthesized by the pyrolysis of transition metal, nitrogen and carbon precursor materials. Factors influencing the ORR activity and durability are including transition metal type, carbon support, nitrogen content and heat treatment condition. Many series of macrocylces, phthalocyanines (Pc), tetramethoxyphenylporphyrin

(TMPP), tetraphenylporphyrin (TPP) and polyaniline(PANI) complexed with transition metals (Fe, Co, Ni and Cu) have been thoroughly investigated toward ORR.[28-30] Previous investigations have indicated that the complexes with Co and Cu appear to be the most stable, while the complexes with Fe and Co appear to be the most active. The ORR activity can be further improved for complexes containing two or more different metal-ion centers. It is observed that pyrolyzed Fe/Co-N_x catalysts not only enhance the ORR activity but also improve the stability.[31-35] Carbon supported PANI-Fe_3Co had a high ORR performance (open cell potential is 0.93 V) with less than 10 % degradation was observed after 700 h at 0.4 V in a fuel cell setup (Fig. 1.3).[34] It has been recognized that the pyrolysis process is responsible for active site formation, giving a high ORR performance relative to non-pyrolyzed macrocycles. Normally, *M*-N_x/C complexes with high activity can be obtained at heating temperatures between 500 and 800 °C in an inert atmosphere. In this temperature range, a thermal rearrangement of the carbon, nitrogen and metal groups creates active sites for the ORR. Above 800 °C, the formation of metallic particles or metal oxides/carbides occurs with a decrease in nitrogen content, leading to a reduced activity.[36-38]

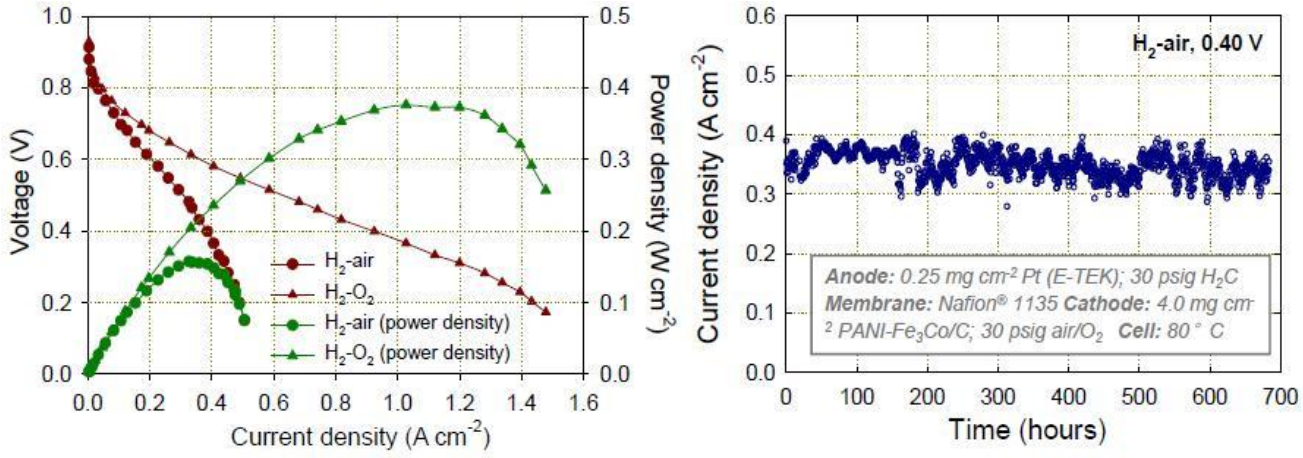

Figure 1.3 Left: polarization curves of PANI-Fe_3Co-C catalyst in a fuel cell setup. Right: durability test of PANI-Fe_3Co-C catalyst holding at 0.4 V.[34]

The nature of catalytically active sites in these macrocycles still remains uncertain. A debate is focused on whether the transition metal ions represent the active species or not. Dodelet's group proposed that the configuration of Fe coordinated by four nitrogen atoms (Fe-N_4) is responsible for ORR activity.[39] An alternative hypothesis is that the transition metal is not the active site. The ORR activity is attributed to the formation of graphitic nitrogen and pyridinic nitrogen groups. The function of transition metals is to catalyze the formation of N-C active sites. This statement is supported by the observed ORR activity of metal free N/C catalysts.[40,41] Although the exact nature of metal ions is ambiguous, the presence of metal ion center during pyrolysis has a significant impact on ORR activity.

In PEMFCs, the acid stability requirement rules out most oxides since few electronically conductive oxides are stable in an acidic environment. It was reported that when ruthenium-pyrochlore electrodes were attached to a proton-exchange membrane, the electrode was stable in acidic solutions.[42] In this aspect, pyrochlores have potential applications for PEM fuel cells. The face centered pyrochlore structure can be described by the general formula: $A_2B_2O_6O'$. The cubic B_2O_6 framework of corner-shared octahedra is interconnected by an A_2O' array. The *B*-O-*B* bond angle ranges from 180° to 135°. The strong *B*-O-*B* interactions within the B_2O_6 framework are responsible for the metallic conductivity of pyrochlore oxides. There are two types of oxygen: the O oxygen is bonded to both *A* and *B* cations whereas the O' oxygen is only bonded to *A* cations. The O' oxygens can be partially or totally absent and are often the source of non-stoichiometry in pyrochlores. The conductivities of heavily non-stoichiometric oxides are only marginally lower than that of metals. For instance, $Pb_2Ru_2O_{6.5}$ and $Bi_2Ru_2O_{7-\delta}$ have high conductivities of $\sigma = 10^2$-10^3 S/cm at room temperature.[43] $A_2B_2O_7$ compounds exhibit a wide variety of interesting electric properties. This is because *B* cations can be transition metal

elements with variable oxidation states and *A* cations can be rare earths (*Ln*), alkaline earths or other large elements. Thus, the electrical nature of pyrochlores vary from highly insulating to semiconducting to metallic behavior. Since pyrochlores have many possibilities for good metallic conductors and can accommodate many metals useful in catalysis, they belong to a good structural family for designing electrodes for electrocatalysis. Previous studies investigated the activity and stability of ruthenium pyrochlore oxides. Study showed that ruthenium pyrochlores could catalyze the ORR in acid environment by attaching to a Nafion or Dow developmental fuel cell membrane.[42] Stabilized $Pb_2Ru_{1.95}Pb_{0.05}O_{7-\delta}$ showed a higher activity than commercial Pt catalyst under acidic conditions.[44] Further modifications on metal oxides are required to overcome the stability challenges.

Recently, nitrides, oxynitrides, carbides and carbonitrides modified by transition metals have been explored as ORR catalyst candidates. Nitrides are relatively stable and have high electrochemical potentials. Many studies have been focused on molybdenum nitrides and tungsten nitrides. Although the ORR activity of carbon supported W_2N is low, this material remains stable after 100 hours operation in a fuel cell setup.[45] Molybdenum nitrides have higher ORR current density and onset potential than tungsten nitrides. Mo_2N/C exhibited an open circuit potential of 0.6 – 0.8 V and no deterioration was observed after 60 hour cell testing.[46] The kinetics of the ORR on Mo_2N/C was studied and the electron transfer number was 3.8, suggesting that the reaction mechanism followed a 4-electron pathway. Heat treatment of carbon supported transition metals in NH_3 was utilized for the synthesis. The ORR activity of carbon supported nitride is ascribed to metal nitride and pyrrolic nitrogen species present in the carbon support.[27] Oxynitrides are formed by doping nitrogen into metal oxides. The doping of nitrogen can reduce the band gap of oxides and decrease its electrical resistivity.[47] TaO_xN_y was reported

to have an ORR onset potential as high as 0.8 V.[48] Powder ZrO_xN_y showed an onset potential of 0.7 V while thin film ZrO_xN_y had an onset potential of 0.8 V.[49,50] Both Ta and Zr oxynitrides exhibited excellent stability in acid.

Tungsten carbide (WC) was reported to have a similar electronic structure with platinum,[51] which inspired investigations on carbides for ORR catalysis. However, applications of pure carbides are unfeasible due to the limited acid stability. Incorporation of Ta into WC improves the stability. The improvement is attributed to the formation of Ta-W alloy phase. Ni-Ta-C compound is found to be stable in acid electrolyte since a thin TaO on the surface protects the bulk material.[52,53] Carbonitrides such as CrCN,CoCN,NiCN and FeCN could display ORR activity.[54,55] It was also found that partial oxidation of carbonitrides have a positive effect on the ORR activity.[56-59] For example, the onset potential of partially oxidized ZrCN compound increased to 0.97 V and it was stable at an electrode potential of 0.6 V for 100 hours.[57]

As discussed above, non-precious transition metal based catalysts haven shown promising ORR activity and stability. It is pivotal to optimize the catalyst composition, structure and morphology to increase the ORR activity to meet the DOE activity targets. In the long term, understanding the active sites in these different structures is important to further improve the catalytic properties in a rational manner.

1.2.3 Catalyst in Alkaline Fuel Cell (AFC)

One major advantage of AFC is that the ORR kinetics are inherently faster in alkaline electrolyte. However, carbonation issues remain a serious problem for AFCs if air is used as the feed. The formation of K_2CO_3 precipitations will change the electrolyte pH and block the gas-diffusion electrode which causes the failure of the entire cell. To solve the problem, a solid polymer electrolyte, analogous to proton exchange membrane, has been developed. The modified

AFC is similar to PEMFC. The membrane only transfers OH^- ions produced at the cathode to the anode side to react with H_2.[60] Although development of AFCs with anion exchange membrane is still underway, noble-metal-free AFCs hold promise in the future.

1.2.3.1 Noble Metal Based Catalyst

Pt and Pt-based alloys are most active catalysts in alkaline electrolytes.[61-67] Pt/C with a loading of 60 wt% Pt reduces oxygen through four electron process.[66] Pt-based alloys exhibit higher activity and/or stability.[65] Silver has been studied as replacement of Pt due to its high performance in alkaline media and relatively low cost. The size of Ag particles and oxidation state of Ag on the surface affect the performance. Ag nanoparticles (5-10 nm) on carbon with a loading between 20 wt% and 30 wt% proceed through a four electron pathway.[68] The effect of hydroxide concentration is positive for Ag but negative for Pt. Ag-based materials becomes competitive to Pt in alkaline media with a high concentration.[68]

1.2.3.2 Non-noble Metal Based Catalyst

Numerous non-noble metal catalysts in AFCs have been developed and screened in terms of their ORR activity. Although carbonaceous materials show poor activity in acid, these materials are able to catalyze ORR in alkaline through a two electron process. Functional carbonaceous materials with a high surface area have increased activity. Non-noble metal oxides have also been studied. In these studies, binary manganese oxides, spinel oxides and perovskite oxides are attractive alternatives to noble metals due to their ORR performance and low cost.

Manganese oxides possess prominent advantages such as good activity toward ORR, abundance, low cost and environmental friendliness. Binary MnO_x with different stoichiometry and crystal structures have different activities. Previous studies demonstrate that the activity

follows the sequence of $Mn_5O_8 < Mn_3O_4 < Mn_2O_3 <$ MnOOH and MnO_2.[69,70] The high activity of MnO_2 is attributed to the reduction of Mn^{4+} to Mn^{3+} and the following electron transfer from Mn^{3+} to oxygen molecules. There are multiple structural polytypes for MnO_2, including 1D tunnel structures (α-,β- and γ-MnO_2), a 2D layered structure (δ-MnO_2) and a 3D spinel structure (λ-MnO_2). α-MnO_2, which has a characteristic 2 × 2 tunnel structure, exhibits the highest activity among these phases. By depositing Ni nanoparticles onto α-MnO_2 nanowires, the onset potential increases 20 mV compared to α-MnO_2 nanowires and the overall ORR is a quasi 4-electron transfer.[71]

Spinel oxides and perovskite oxides have also shown high ORR activity. Their catalytic properties can be modified by incorporating transition metals into these tunable structures. Spinel oxides have the composition of AB_2O_4. *A* and *B* can be monovalent, divalent, trivalent, or even tetravalent cations, including Mg^{2+}, Zn^{2+}, Fe^{3+}, Mn^{3+}, Al^{3+}, Ti^{4+} and Si^{4+}. In the ideal spinel structure, oxide anions form a cubic close-packed arrangement, in which *A* cations occupy tetrahedral holes and *B* cations occupy octahedral holes. The spinel structure is very flexible due to the wide range of cations it can incorporate. In addition, *A* and *B* can be the same type of cations with different oxidation state as in Fe_3O_4. Depending on the oxidation state, vacancies can be present in the structure. The vacancies in the structure result in better ion mobility. Spinels such as Co_3O_4, $NiCo_2O_4$, $CoFe_2O_4$, and $MnCo_2O_4$ have been investigated for their ORR activity. The activity of $NiCo_2O_4$ reached 250 mA/cm^2 at 0.65 V in 5N KOH at 25°C. However, the activity decreased to less than 2 mA/cm^2 within 2-3h.[72] A mixture of $NiCo_2O_4$ and FeO_x enhances the electrocatalytic activity because FeO_x reduces the overpotential of ORR.[73] In order to improve its stability, Yeung and Tseung[74] bound $NiCo_2O_4$ with Teflon and its performance remained at 25 mA/cm^2 at 750 mV over a period of 130 hours in 5N KOH. In $Mn_xCo_{3-x}O_4$ ($0 < x$

< 1), the influence of cation distribution toward ORR has been investigated .[75] The ORR current density is affected by the bulk Co/Mo ratio. However, the ORR on $Mn_xCo_{3-x}O_4$ proceeds through multiple steps involving HO_2^- as an intermediate. Catalyst supports also play a crucial role for ORR performance. Although Co_3O_4 nanoparticles only show little ORR activity, Co_3O_4 grown on reduced graphene oxide is reported as a high-performance cathode catalyst for oxygen reduction.[76] In 6 M KOH, the hybrid exhibits comparable activity but superior stability to commercial Pt (Figure 1.4). Chronoamerometry measurements demonstrates that the activity of the hybrid remains stable over 10000 s while the activity of Pt exhibits a ~ 40% decrease at the same operation condition.

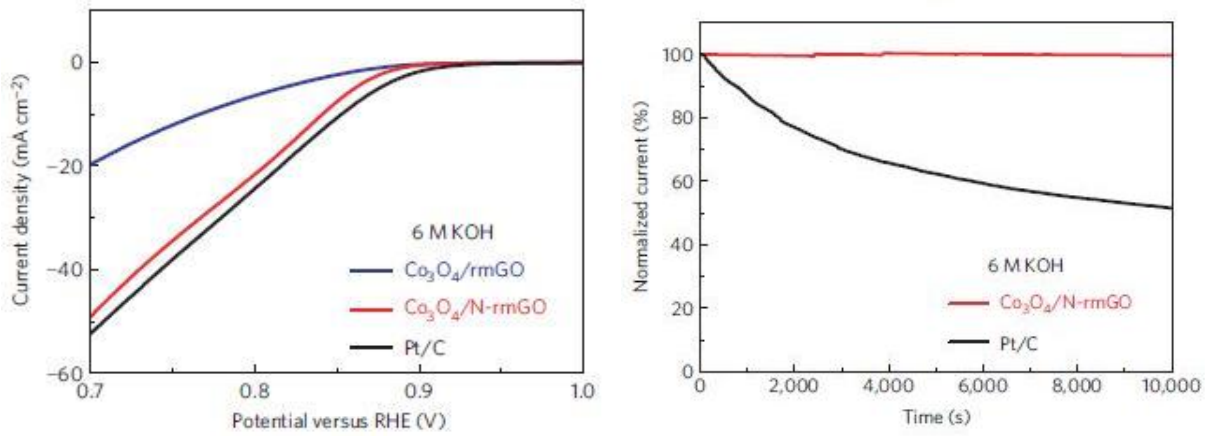

Figure 1.4 Left: oxygen reduction polarization curves of Co_3O_4/rmGO, Co_3O_4/N-rmGO and commercial Pt/C catalyst (catalyst loading ~0.24mg/cm^2) in O_2-saturated 6 M KOH. Right: Chronoamperometric responses of Co_3O_4/N-rmGO and commercial Pt/C kept at 0.70 V in O_2-saturated 6 M KOH.[76]

ABO_3 compounds with the perovskite structure can be described as having a three-dimensional framework made up of *B*O_6 octahedra. The centers of the frameworks are 12-fold coordinated *A* cations in ideal perovskites. The electronic conductivities of perovskites are generally higher than spinels due to the edge sharing octahedral chains of spinels. Perovskite-type rare earth cobaltites, ferrites and manganites have been found to give good electrode

performance. Among these oxides, *Ln*MnO_3 (*Ln*=lanthanides) are active and stable in alkaline solutions. Furthermore, $LaMnO_{3+\delta}$ allows the partial substitution of La and Mn for Sr and Fe respectively, which gives a significant improvement in activity. Yuasa tested the performance of $La_{0.6}Sr_{0.4}Mn_{0.8}Fe_{0.2}O_{3+\delta}$ in 9M NaOH at 85°C.[77] The loading of 17 mass% $La_{0.6}Sr_{0.4}Mn_{0.8}Fe_{0.2}O_{3+\delta}$ on the carbon support have shown excellent activity.

The intrinsic catalytic activity of La-based perovskites was studied through a thin-film rotating ring-disk electrode technique.[78] For La*M*O_3 (*M* = Ni, Co, Fe, Mn and Cr), $LaCoO_3$ shows the largest ORR current and highest onset potential. For $LaNi_{0.5}M_{0.5}O_3$, substituting half of the nickel with other transition metals (Fe, Co, Mn or Cr) enhances the ORR reaction and provides a promising route to optimize the catalyst. Koutecky – Levich analysis indicates that the ORR on these compounds is close to a 4-electron reaction, a result which is also supported by the small amount of hydrogen peroxide production (< 2%). Factors linked to catalytic activity have been investigated among La-based perovskites synthesized via co-precipitation method.[79] La perovskite oxides with *A*-site ($La_{1-x}Ca_xBO_3$ and $La_{1+x}BO_3$) and *B*-site ($LaB_{1-x}B'O_3$) substitution were studied for ORR catalysis. A volcano relationship is obtained between the e_g electron of *B*-site atoms and ORR activity. Based on the volcano plot, too few e_g electrons result in a overly strong *B*-O_2 bonding, whereas too many e_g electrons produce too weak *B*-O_2 bonding. A maximum ORR activity can be approached in transition metal perovskites with an e_g electron filling near 1. This work provides design principles for perovskite type catalysts enhanced ORR activity that might replace platinum.

1.3 Catalyst Evaluation Techniques

The most frequently used techniques for ORR catalysis studies include steady-state polarization, cyclic voltammetry (CV), rotating disk electrode (RDE) and rotating ring-disk

electrode (RRDE) measurements. All of these experiments are conducted in a conventional three-electrode electrochemical cell (Figure 1.5). In the cell, the working electrode, counter electrode and reference electrode are immersed in an Ar or O_2 saturated electrolyte. In this setup, the potential is measured between the working electrode and reference electrode and the current passes through the working electrode and counter electrode.

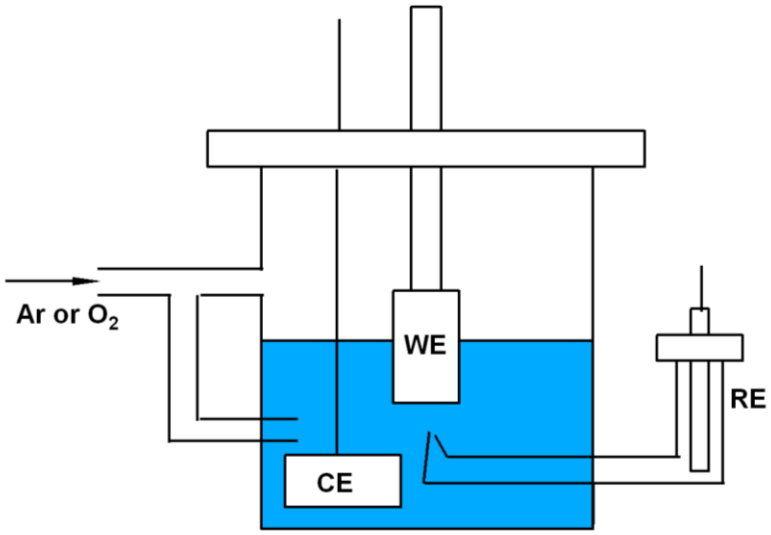

Figure 1.5 Basic scheme of three-electrode electrochemical cell.

Steady-state polarization curves are recorded by sweeping the electrode potential and recording the current response (Figure 1.1). For a good ORR catalyst, high current density at lower overpotential is expected. To compare ORR catalysts, current density at a specific potential or the overpotential at a specific current are evaluated. Cyclic voltammetry measures the electrochemical response and the catalytic activity of catalysts. For catalysts containing transition metals, specific redox pairs may be observed. The onset potential toward ORR is obtained by subtracting the CV measured in Ar from the CV measured in O_2. Good ORR catalysts have a high onset potential as close as possible to the theoretical potential (1.23 V).

1.3.1 Rotating Disk Electrode (RDE)

The RDE is a hydrodynamic working electrode. The electrode rotates to induce a flux of reactant to the electrode surface and the products are swept away from the electrode. The steady-state current is controlled by the solution flow generated by RDE rather than by the diffusion of the reactants and products, in contrast to static experiments like CV. RDE responses follow the Koutecky-Levich equation[80]:

$$\frac{1}{j} = \frac{1}{j_k} + \frac{1}{j_d} \quad (1.17)$$

where j is the measured disk current density, j_k is the kinetic current density without any mass transfer effect, and j_d is the diffusion-limiting current density (Levich current density). The term j_k can be expressed as

$$j_k = nFk_{O2}C_{O2}\Gamma_{\text{catalyst}} \quad (1.18)$$

where n is the overall electron transfer number, k_{O2} is the reaction rate constant which is related to the potential, C_{O2} is the concentration of dissolved O_2 in electrolyte, and Γ_{catalyst} is the catalyst loading on the electrode surface. The term j_d can be expressed according to the Levich equation

$$j_d = 0.201nFC_{O2}D_{O2}^{2/3}\nu^{-1/6}\omega^{1/2} \quad (1.19)$$

where D_{O2} is the diffusion coefficient of O_2, v is the kinematic viscosity of the electrolyte, and ω is the rotation rate in rpm. The diffusion limiting current is thus expected to be proportional to the square root of the rotation speed of the RDE.

For RDE analysis, C_{O2}, D_{O2} and v are constant parameters which depend on temperature and the electrolyte. If $1/j$ is plotted against $\omega^{-1/2}$, a linear plot can be obtained. The slope of the plot can be used to estimate the number of electrons transferred during the ORR. Also j_k can be obtained from the intercept of the plot.

1.3.2 Rotating Ring-disk Electrode (RRDE)

RRDE experiments are used to probe the ORR mechanism. In RRDE, experimental intermediates like H_2O_2 which are generated during the ORR can be detected on the ring electrode. On the disk electrode, 2- or 4-electron reactions occur. On the ring electrode, products from $2e^-$ reactions (H_2O_2) are oxidized into H_2O, which can be measured at a higher potential. The $2e^-$ current (I_{2e}) is given by

$$I_{2e} = I_R / N \quad (1.20)$$

where I_R is the ring current, N is collecting coefficient number of RRDE. Since the disk current (I_D) is the sum of both the $2e^-$ and $4e^-$ currents, the average transfer electron number (n) for ORR is calculated by

$$n = \frac{4I_D}{I_D + I_R/N} \quad (1.21)$$

1.4 Water Electrolysis

As mentioned in previous session, hydrogen and oxygen are used in hydrogen fuel cells to provide energy. Hydrogen and oxygen are clean fuels since the only byproduct of the fuel cell is water, which is environmentally benign. Oxygen can be obtained from air easily, but hydrogen does not exist as molecular form in nature. Today, hydrogen is mainly produced by steam reforming from natural gas.[81] However, this method consumes non-renewable fossil fuels. Another alternative method to produce hydrogen is water electrolysis which converts electrical energy to chemical energy in an electrolyzer. The electrolysis method supplies 4%-5% of the world's hydrogen.[81] The electrical power needed to drive the chemical reaction can be provided by renewable wind, solar energy or other renewable soure. Hydrogen generated in this manner can be stored and used in fuel cells later to provide electricity on demand. One advantage of a

water electrolysis cycle is that hydrogen can be stored and used on the station directly without the need for transportation.

There are two types of electrolyzers commercially available: alkaline and proton exchange membrane (PEM). Alkaline electrolysis is a mature and commercial technology for hydrogen production. However, the membrane of alkaline electrolyzer can not prevent cross-diffusion of product gas completely, which reduces its efficiency. The high Ohmic loss across the alkaline electrolyte also lowers the achievable current density.[81] PEM electrolyzers have been developed to overcome these drawbacks. A thin layer of polymer electrolyte membrane (Nafion) is used in PEM electrolyzers (Figure 1.6). The advantages of PEM electrolysis include high current density, good voltage efficiency and high output gas purity since the Nafion membrane possesses the advantageous properties of high proton conductivity and low gas crossover.[81] Problems related to high cost of components and possibly low durability in corrosive acidic environment are still present and these problems prevent the wide commercialization of PEM electrolysis. In order to develop this technology and contribute to a future hydrogen based economy, the development of suitable electrocatalysts with high efficiency, low cost and long-term stability is pursued.

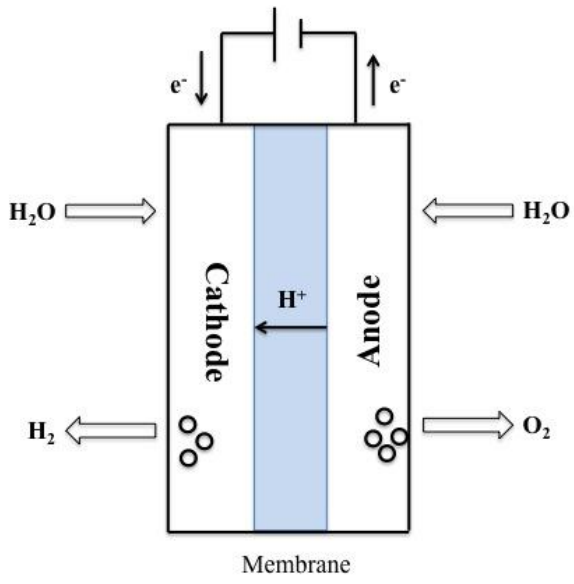

Figure 1.6 Basic scheme of PEM electrolyzer: only protons are allowed to pass through the proton exchange membrane. H_2 molecules are produced at the cathode while O_2 molecules are produced at the anode.

1.4.1 Mechanism for Hydrogen Evolution Reaction

Cathode catalysts for water electrolyzer need to provide sufficient cathode current to reduce protons to H_2 molecules. In contrast to the slow oxygen evolution reaction (OER) kinetics, the kinetics of HER is much faster due to its two electron process. The HER proceeds through a combination of three primary steps to convert H^+ into H_2. These elementary steps include the discharge of proton to adsorption hydrogen (H_{ads}) (Volmer reaction, Eq.1.22), the simultaneous electron transfer between proton and adsorped hydrogen (Heyrovsky reaction, Eq.1.23) and the dissociation of H_2 without electron transfer (Tafel reaction, Eq.1.24).[82,83] The combination of Volmer-Heyrovsky or Volmer-Tafel reactions leads to the production of H_2. Tafel slopes indicate how fast the electrode responds to an applied potential to produce current, and can be applied to evaluate the electrode performance. The Tafel slopes of these three reactions differ from each other. The Volmer reaction has a Tafel slope of 120 mV/dec, while the

Heyrovsky and Tafel reactions have slopes of 40 and 30 mV/dec, respectively.[82-84] Experimentally measured Tafel slopes can potentially be used to identify the HER mechanism.

$$\text{Volmer: } H^+ + e^- \rightarrow H_{ads} \qquad (1.22)$$

$$\text{Heyrovsky: } H_{ads} + H^+ + e^- \rightarrow H_2 \qquad (1.23)$$

$$\text{Tafel: } H_{ads} + H_{ads} \rightarrow H_2 \qquad (1.24)$$

Although Tafel slopes can be used as guide to the mechanism, it should be noted that these values are based on measurements for noble metals and may vary under different experimental conditions. Density functional theory (DFT) calculations can be employed to model electrochemical reactions and explore reaction at the interface on a molecular scale.[85-90] The kinetics of Tafel reaction on different metals with different facets were studied using DFT calculations. The calculated rates and exchange current densities are in good agreement with experimental data.[86,88,90]

1.4.2 Catalysts for Hydrogen Evolution Reaction

There are two basic requirements for a good cathode catalyst. First, the catalyst should be highly active toward HER. The high activity means a low overpotential, a high current density and a large exchange current density. Second, the catalyst should possess long-term durability in electrolyte.

A comprehensive study of pure metals for HER was performed by Miles and Thomason. It was found that the activity for HER in 0.1 M H_2SO_4 at 80 °C had a following order: Pd > Pt > Rh > Ir > Re > Os > Ru > Ni.[81] Later on, Nørskov *et al*. used DFT to calculate hydrogen adsorption energies on noble and transition metals with a close packed structure.[86,88] Plotting catalytic activity (exchange current density) versus free energy of hydrogen adsorption (ΔG_H)

gives rise to a volcano relation (Fig. 1.7). From the peak to the left side, the activity decreases with a decreasing ΔG_H value since the bonding strength of left side elements is too strong to form metal hydrogen bond at the surface. From the peak to the right side, the activity decreases with a increasing ΔG_H value because proton transfer becomes more difficult and hydrogen becomes more unstable.[86,88] Therefore, materials with intermediate metal-hydrogen bond strength are the most suitable HER catalyst. In this diagram, Pt is close to the optimal value which is consistent with the fact that Pt is the most efficient electrocatalyst known for HER. Although the loading of Pt on the cathode is relatively low compared to the anode, the cathode still represents a considerable cost. In order to lower the Pt loading, further development of more homogeneous catalyst with smaller particle size is underway.

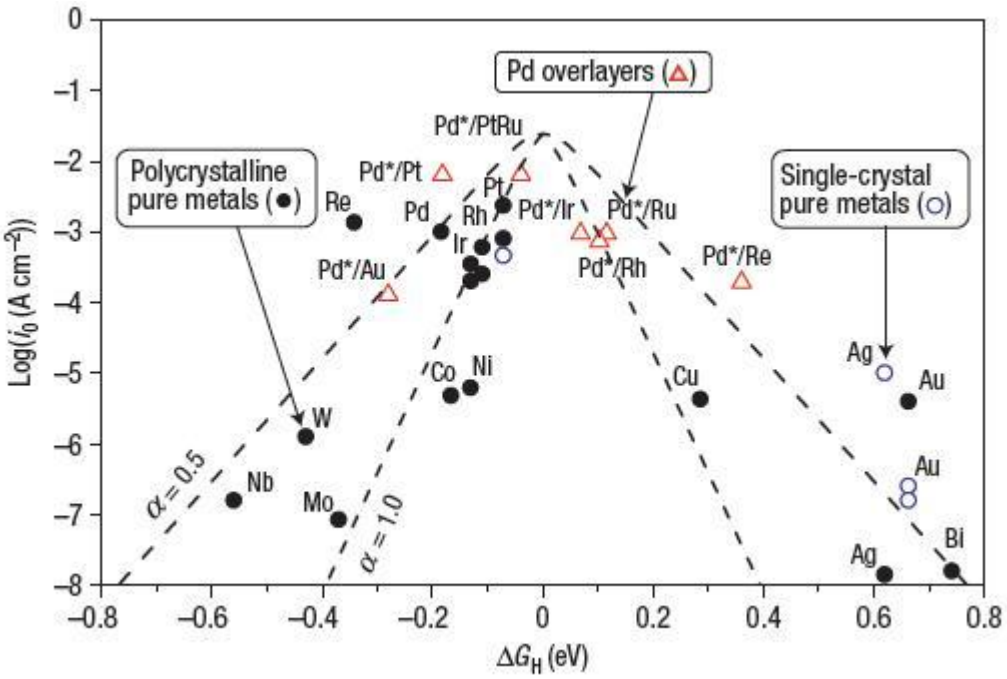

Figure 1.7 Measured exchange current density of different metals plotted as a function of free energy for hydrogen adsorption ΔG_H. ΔG_H values are calculated at 1 bar of H_2 (298 K). The two dashed lines correspond to the activity predictions assuming transfer coefficients of 0.5 and 1.0, respectively. [86]

Alloys are considered to be good alternatives to pure noble metals. Alloys can be used to lower the loading amount of noble metals as well as to enhance their activity and stability. DFT calculations suggest that surface alloys, including BiPt, PtRu, AsPt, SbPt, BiRh, RhRe, PtRe, AsRu, IrRu, RhRu, IrRe and PtRh, are both active and stable toward HER in acidic environments.[86] It should be noted that Pt is highly active for HER while Bi is not active for HER. The surface alloy combining these two elements is predicted to be active. The BiPt surface alloy prepared by a three-step deposition method is confirmed to exhibit high catalytic activity, which is comparable to or even better than pure Pt films.[86] Hence, exploring alloys is desirable to provide more possible catalyst candidates.

Depositing monolayer Pt on low-cost substrates is another method to minimize Pt amounts while retaining activity. Monolayer (ML) Pt was deposited onto WC thin films by thermal evaporation. It is found that the Tafel plot of 1 ML Pt on WC thin film was almost identical to that of bulk Pt.[91] By varying the substrates, catalytic properties may be further improved. Designed materials with core-shell structures are able to decrease Pt loadings while remaining activity. Core-shell catalysts consist of monolayers of active materials (Pt or Pt alloys) supported on a metallic core. Noble metal catalyst with a core-shell morphology can reduce the amount of noble metal and exhibit enhanced activity and/or stability for ORR reaction in fuel cells.[92] Core-shell structures are promising alternatives for HER catalysis.

These limitations of using expensive noble metals even at low loadings have motivated extensive efforts to design and develop non-noble metal HER electrocatalysts which are stable in acidic environments. Ni-based materials are generally used as electrode catalysts in alkaline electrolyzer.[93] Although some of these catalysts have shown high activity in acidic electrolytes,

their poor stability remains a problem. Mo based materials, especially MoS_2, have been widely investigated as cathode catalysts for HER in acidic electrolytes.[83,87,94-99]

MoS_2 is a well-known classic catalyst in hydrodesulfurization (HDS) which also involves H_2.[100] It was also reported that molybdenum-sulfide dimers were able to produce hydrogen at low overpotentials in organic solvents.[101] Initially, MoS_2 was not considered as a promising catalyst for HER since bulk MoS_2 showed poor activity. In contrast, nanoparticles of MoS_2 were reported to be active HER catalysts.[94] Since then, the investigation and development of MoS_2 have intensified. Carbon-supported nanoparticulate MoS_2 has been studied in sulfuric acid. It was found that the overpotential of carbon-supported MoS_2 is comparable to the hydrogen binding energy on the edge of the nanoparticles.[95] Therefore, the active sites of MoS_2 for HER are edge sites rather than basal planes. A scanning tunneling microscopy (STM) study of MoS_2 nanoparticles supported on Au (111) surface also provided direct evidence that the active sites are indeed edge sites.[87] Heterogeneous MoS_2 contains two types of edges, the Mo-edge and the S-edge. Generally, Mo-edge sites are more active toward HER since Mo-edge has a ΔG_H of 0.08 eV which is the major edge exposed.[95] The structure and morphology of MoS_2 are tunable by using different starting reagents and synthesis methods. Factors like composition, structure and morphology have great impacts on the catalytic properties. Studies have presented excellent HER activity on various forms of MoS_2 and its analogues. Core-shell MoO_3-MoS_2 nanowires have been developed to drive HER efficiently with stable activity over thousands of potential cycles.[83] The morphology of vertically aligned core-shell nanowires provides a high surface area for catalysis. The MoO_3 core is partially reduced and served as a highly conductive substrate. The ultrathin MoS_2 shell served as a cathode catalyst and a protective layer to prevent the dissolution of MoO_3 core.[83] MoS_2 grown on reduced graphene oxide (RGO) also demonstrates

high activity with low overpotential (~0.1 V) and small Tafel slope (41 mV/decade).[96] Unlike aggregated MoS_2 grown freely in solution without GO, the growth of MoS_2 nanoparticles are selective due to the strong chemical coupling between MoS_2 and graphene oxide sheets.[96] The highly dispersed MoS_2 nanoparticles afford abundant exposed edge sites which serve as active sites. The synergistic coupling of the hybrid combines the sulfide strongly with the RGO substrate which facilitates a fast electron transport. This MoS_2/RGO hybrid exhibits superior activity relative to other MoS_2 catalysts. Two-dimensional MoS_2 contains single S-Mo-S layers in hexagonally packed structures which can exist in various polymorphs. 2H-MoS_2 phase is thermodynamically favored in nature, and contains MoS_6 in a trigonal prismatic geometry. 2H-MoS_2 is a semiconductor whose poor conduction limits the overall catalytic efficiency. In contrast, 1T-MoS_2 containing edge-sharing MoS_6 octahedra is reported to be metallic.[97] 1T-MoS_2 nanosheets can be achieved by lithium intercalation into 2H-MoS_2. This chemical exfoliated metallic 1T-MoS_2 exhibits superior and stable HER activity owning to its proliferated active sites and facile electron transport.[97] Besides crystalline MoS_2, amorphous MoS_2 synthesized through a wet chemistry synthesis is a highly active catalyst with an overpotential of 200 mV that achieves 10 mA/cm^2 hydrogen evolution current densities, which is a useful metric to compare catalysts for solar hydrogen production.[98] This material shows the highest activity among reported MoS_2 synthesized using a room temperature wet chemistry method (Fig. 1.8). Thin film samples have the advantage of homogeneity compared to powder samples. MoS_2 and $MoSe_2$ thin films have been tested for HER catalysis. The configuration of edge-terminated thin film contains vertically aligned layers with the purpose of exposing edge sites maximally.[99] Because current density of these thin films is smaller than that of powder samples, further improvements are underway. Other chalcogenides like cubane-type $[Mo_3S_4]^{4+}$ have also been

found to show high per-molecule catalytic efficiency though the durability remains a problem in acidic electrolyte.[102] In conclusion, future optimization of MoS_2 will focus on improving its conductivity and maximizing the density of active edge sites by controlling the nanostructure growth.

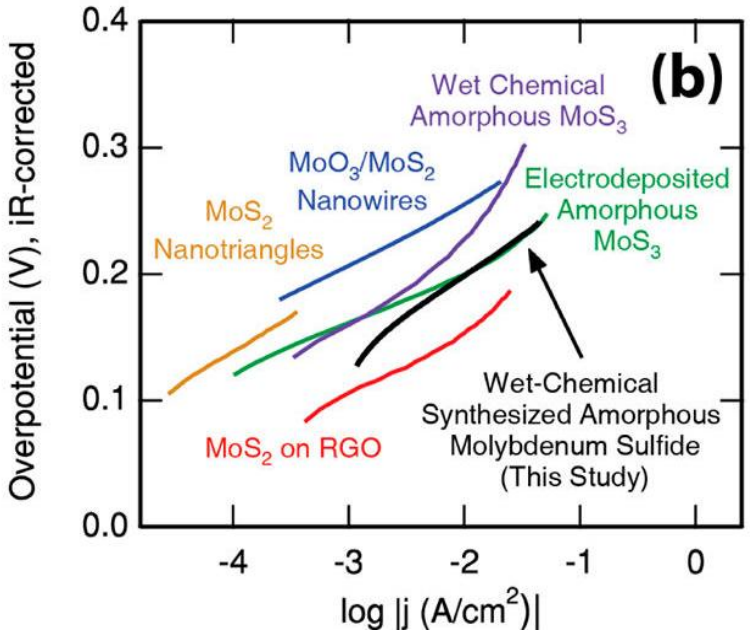

Figure 1.8 Tafel plots of molybdenum sulfide catalysts for HER, including MoO_3/MoS_2 core-shell nanowires in 0.5 M H_2SO_4 (blue line), MoS_2 nanotriangles in H_2SO_4 (pH = 0.24, orange line), amorphous MoS_3 in 1 M H_2SO_4 (purple line), electrodeposited amorphous MoS_3 (pH = 0, green line), wet-chemical synthesized amorphous MoS_2 in 0.5 M H_2SO_4 (black line) and MoS_2/RGO in 0.5 M H_2SO_4 (red line). [98]

In addition to molybdenum sulfides, other molybdenum-based materials have also been investigated. Nitrides and carbides have shown excellent catalytic activities toward various reactions.[103-105] The function of such material as a catalyst resembles that of noble metal for certain reactions. MoN, MoB and Mo_2C have been evaluated to be good catalysts for hydrogen evolution.[103-105] Although the particle sizes of MoB and Mo_2C are large and irregular, their activities are high in both acid and alkaline conditions.[103] The Faradaic yields of these catalysts are quantitative in both media. Better performance could be achieved by making more defined

nanoparticles. For instance, nanostructured β-Mo_2C supported on carbon nanotube gave a higher HER current density compared to bulk Mo_2C.[104] Similar to Mo_2C, hexagonal MoN is able to catalyze hydrogen production reaction.[105] Incorporation of nickel in the molybdenum nitride structure further enhances its activity.[105] Unlike nickel-molybdenum which is stable in alkaline but not acidic environments, $NiMoN_x$ nanosheets only show a slight degradation over 2000 cycles. The high activity and stability may be attributed to the exfoliated nanosheet structure and modified d-band electronic structure, though more experiments need to be conducted to elucidate the intrinsic reason. Recently, hexagonal Ni_2P, a well-known HDS catalyst, was found to exhibit high activity comparable to Pt.[106] Hollow Ni_2P has a high density of exposed (001) surface sites which are predicted to be active sites for HER based on theory.[106] To date, the majority of non-noble metal based HER electrocatalyst are binary compounds. It is intriguing to develop ternary or even more complicated compounds. Hence, chemical substitution and nanostructure modification will be promising strategies to further improve the catalytic activity and stability for HER.

1.5 Objectives of Research Work

As discussed in the previous section, the utilization of sustainable and clean energy sources such as hydrogen fuel in the future is required due to energy crisis and environmental problems caused by fuel combustion. Hydrogen fuel cells are potential solutions to replace internal combustion engines since the theoretical energy density of H_2 is higher than gasoline and it is environmentally benign. Compared to hydrogen oxidation catalysis, oxygen reduction reaction is more challenging due to the sluggish four electron process. Pt is the best known cathode catalyst for ORR. However, the cost and scarcity of Pt currently prevent the commercialization of hydrogen fuel cells. Therefore, it is desirable to investigate non-noble

metal based cathode materials as alternative to Pt. Mo-based oxynitrides and nitrides have been explored as ORR catalysts in this study since the modified oxynitride or nitride surface makes it easier to donate electrons to oxygen molecules and facilitates the ORR reaction.

The hydrogen evolution reaction is an important reaction in the renewable production of H_2 from water electrolysis. Utilization of H_2 as a future energy source requires efficient catalysts for HER. Unfortunately, the best current HER catalysts incorporate noble metals such as Pt, whose terrestrial scarcity and high cost limit the viability of renewable H_2 production. These limitations have motivated extensive efforts to design and develop non-noble metal HER electrocatalysts which are stable under acidic environments. Notable recent progress has been made in the last decade in developing acid-stable HER catalysts, resulting in the discovery of excellent HER activity for MoS_2, Mo_2C, MoB, Ni-Mo, Ni-Mo-N, and Ni_2P, all of which contain Mo and/or Ni. We are therefore motivated to investigate the electrocatalytic activity of more complex ternary molybdenum nitrides in which the valence and electronic states of Mo can be more readily tuned than in binary molybdenum nitrides.

In this thesis, we studied binary molybdenum nitrides (Mo-N), cobalt molybdenum oxynitrides (Co-Mo-O-N)[107], ternary cobalt molybdenum nitride (Co-Mo-N)[108] and ternary iron tungsten nitride (Fe-W-N) as electrocatalyst candidates for oxygen reduction reaction and hydrogen evolution reaction. These nitrides and oxynitrides were prepared by ammonolysis method. Synthesis conditions were modified by altering the precursor, annealing temperature and flow rate. Their crystal structures were studied by X-ray diffraction, neutron diffraction and neutron pair distribution function analysis. Their morphologies were characterized by scanning electron microscope and transmission electron microscope. The valence states and compositions were analyzed using X-ray absorption spectroscopy, X-ray photoelectron spectroscopy and

thermogravimetric analysis. A set of electrochemical techniques including cyclic voltammetry and chronoamperometry were employed to investigate the catalytic activity and stability of these catalysts.

Carbon supported Co-Mo-O-N with different compositions were investigated to establish the correlation of compostion and activity. The structure-reactivity correlation was explored by investigation of Mo-N with different crystal structures. Further improvement of hexagonal Mo-N was approached by doping Co into binary molybdenum nitride. Our studies indicate new possibilities for utilization of Mo-containing (oxy)nitrides as promising catalysts for oxygen reduction reaction and/or hydrogen evolution reaction.

Chapter 2. Carbon-Supported Cobalt Molybdenum Oxynitride as Electrocatalyst for Oxygen Reduction Reaction

2.1 Introduction

Due to energy demands, tremendous research efforts have been focused on developing efficient catalysts for proton exchange membrane fuel cells (PEMFCs) and anion exchange membrane fuel cells (AMFCs). Compared to hydrogen oxidation catalysis, it is much more challenging to develop suitable catalysts for the oxygen reduction reaction (ORR) since the ORR is a complex four electron process which typically has sluggish kinetics that require high overpotentials to overcome.[109] Platinum supported on carbon is the best known cathode catalyst for ORR with a moderate overpotential (about 300 mV). However, Pt is expensive and sensitive to contaminants like halides, methanol and carbon monoxide.[110] It is highly desirable to investigate non-noble metal based materials as alternative cathode catalysts. Various non-noble metal catalysts (NNMCs), such as transition metal chalcogenides,[111] macrocycles,[112-114] transition metal oxides,[79] transition metal carbides/nitrides[46,115,116] and transition metal oxynitrides,[117-120] have been widely studied. Among these NNMCs, catalysts containing cobalt or iron have shown the most promising catalytic activities for ORR.[113,114] These highly active catalysts can be obtained by choosing the right combination of metal-nitrogen-carbon precursors and heating conditions. For example, PANI-FeCo-C was recently reported to exhibit high ORR activity with an onset potential of 0.93 V and retention of activity for 30000 cycles in a PEMFC.[114]

Transition metal nitrides and oxynitrides are well suited for catalysis applications as they have good electrical conductivities and corrosion resistance. Their activities in hydrodenitrogenation and hydrodesulfurization resemble those of noble metals.[115] The

formation of nitrides favourably modifies the catalyst electronic structure such that the contraction of *d*-bands in Group 4-6 nitrides results in a greater electron density near Fermi level. This facilitates the donation of electrons to adsorbates such as oxygen.[115] Therefore, the formation of nitride on the surface may make it easier for the catalytically active metal to reduce oxygen. Previously, ORR activities of monometallic nitrides/oxynitrides of Group 4-6 have been studied in acidic solution for fuel cell applications. [46,115-118] ZrO_xN_y and TaO_xN_y were found to show moderate ORR activities and excellent chemical stabilities in sulfuric acid.[117,118] Studies on MoN and Mo_2N demonstrated that they had comparatively good ORR activities and that the oxygen reduction reaction proceeds through a nearly four electron process.[46,116] Compared to monometallic oxynitrides, bimetallic oxynitrides are potentially better ORR catalyst candidates since their catalytic properties can be enhanced by the combination of multiple active species or by the tuning of electronic states. Indeed, bimetallic Co-W-O-N catalysts supported on carbon were found to have an onset potential of 0.749 V in 0.5 M H_2SO_4, an activity substantially higher than monometallic W and Co oxynitrides.[119] Oyama *et al*. have synthesized bimetallic oxynitrides Co-Mo-O-N with high surface areas which showed excellent hydrodenitrogenation activities.[121] Similar to Co-W-O-N, we hypothesized that Co-Mo-O-N may possess good ORR activities as well. Here, we report the synthesis and characterization of $Co_xMo_{1-x}O_yN_z$ compounds supported on carbon black as effective catalysts for ORR in acidic media and as exceptional ORR catalysts in basic environments.

2.2 Experiment Section

2.2.1 Sample Preparation

The synthesis of fine powders of Co-Mo-O-N catalysts with a composition that is generically represented as $Co_xMo_{1-x}O_yN_z$ was accomplished by the low temperature firing of an

aqueous solution of soluble precursors. For Co/Mo mixed samples (x = 0.25, 0.50, 0.75), stoichiometric amounts of $Co(NO_3)_2 \cdot 6H_2O$ (Alfa Aesar, 97.7%) and $(NH_4)_6Mo_7O_{24} \cdot 4H_2O$ (Alfa Aesar, 99%) were first dissolved completely in deionized water. This clear solution was stirred and dried overnight in air at 393 K. The dried powders were then placed on a semicircular fused quartz boat that was open on both sides to facilitate gas flow over the sample. The boat was placed inside a fused quartz tube (ID=22 mm), and centered inside a tube furnace (SC 11R, 8 in length, 1.25 in diameter/MELLEN Company Inc.). Before heating, the tube was first purged with NH_3, whose flow rate was then stabilized at 20mL/min for the reaction using a calibrated flowmeter (Cole-Parmer 150 mm flowmeter). Samples were quickly heated to 573 K (5 K/min), and then more slowly (1 K/min) raised to their final reaction temperature (773 to 923 K for x = 0.50, 823 K for x = 0.25 and 0.75), where they were kept for 3 hours. Afterwards, samples were cooled to room temperature (5 K/min). Interestingly, Mo did appear to inhibit the formation of Co metal for mixed samples (x = 0.25, 0.50, and 0.75) synthesized at 823K, a temperature at which CoO will completely reduce to Co metal under flowing ammonia. As recommended,[119] reaction products were passivated overnight in N_2 gas at room temperature to prevent rapid and highly exothermic oxidation of the reaction product containing Co metal on air exposure. The phase "Mo_2N" (x = 0.0) was synthesized according to the literature method[46] using the same soluble Mo precursor, but a slightly different thermal treatment (5 K/min to 623 K, 0.5 K/min to 723 K, 2.5 K/min to 973 K, 3 hour hold at 973 K, same cooling procedure as mixed Co/Mo samples). CoO and CoN (x = 1.0) could not be synthesized under similar conditions due to the ease with which Co^{2+} is reduced, and commercially available powder CoO (Alfa Aesar, 95%) was used for activity comparisons. Carbon-supported samples ($Co_xMo_{1-x}O_yN_z$/C) were prepared in an analogous manner with the only change being that carbon black (Vulcan XC72R) was

added into the initial aqueous solution allowing the catalyst to impregnate overnight during the drying process.

2.2.2 Sample Characterization

The crystal structures of reaction products were analyzed with an X-ray diffractometer (D8 Advance, Bruker AXS) set to a diffraction radius of 300 mm in a Bragg-Brentano (θ-θ) geometry, using Cu K_α radiation (K_β line removed with Ni foil), and with a 192 channel LynxEye position sensitive strip detector whose energy level settings were changed to a lower level of 0.19 V and a window of 0.06 V to filter out Co fluorescence within the limited energy resolution of this detector (~25%). Scans were collected using a fixed divergence slit of 0.6º, with a step size of 0.02º over the 2θ range of 7 to 120º and a count time of 9 hours. Routine pattern indexing and phase identification was done using the JADE software package.

Scanning electron microscopy (SEM) analysis was carried out on a JEOL 7600F microscope coupled with energy-dispersive X-ray spectroscopy (EDX). Transmission electron microscope (TEM) imaging studies were performed using an FEI Titan 80-300, equipped with a post-specimen aberration corrector (CEOS) operated at 300 kV. Scanning transmission electron microscopy (STEM) was performed with a cold-field emission Hitachi HD2700C, equipped with an aberration-corrector for the electron probe, operated at 200kV. This instrument is equipped with a Bruker EDS spectrometer and a high-resolution Gatan Enfina electron energy loss spectrometer (EELS).

A PHI 3056 X-ray Photoelectron Spectroscopy (XPS) spectrometer with an Al source in a $2x10^{-10}$ Torr vacuum chamber was used to characterize the surfaces of the catalyst particles. The instrument was calibrated before use with gold and silver foils. Samples were pressed into indium foil (Alfa Aesar) and the foil was attached to the sample holder using carbon tape. High

resolution scans were taken with a 5.85 eV pass energy, 0.05 eV energy step, and 100 repeats to reduce instrument noise. Charging effects were compensated by shifting binding energies based on adventitious carbon 1s peak (284.8 eV). MoO_2 (Alfa Aesar, 99.95%) and MoO_3 (Alfa Aesar - Puratronic) powders were used to determine the Mo $3d_{5/2}$ / Mo $3d_{3/2}$ ratio for the instrument (65%/35%). Peak fits and atomic surface concentration analysis was performed using PHI Multipack software.

X-ray absorption near-edge structure (XANES) spectroscopy measurements on the Co K-edge and Mo $L_{2,3}$-edge were collected at beamline X19A of the National Synchrotron Light Source (NSLS) at Brookhaven National Laboratory (NSLS). As-synthesized sample powders were mounted on Kapton tape and spectra were measured in fluorescence mode using a Lytle detector. The beam intensity was detuned to 60% for the Co K edge and 50% for the Mo L edge to eliminate harmonic contamination. For the Co K-edge edge (7709 eV) only, extended X-ray absorption fine structure (EXAFS) spectra were collected from 150 eV below to 1000 eV above the edge. Metallic Co foil was used as the reference for energy calibration. XANES and EXAFS data fitting was processed using Athena and Artemis.[122] The EXAFS signals χ(k) were isolated from fluorescence data using AUTOBK polynomial background removal. Fourier transforms were calculated using k^2 weighting with a Hanning window function.

2.2.3 Electrochemical Measurements

Catalyst inks for electrochemical testing were prepared by adding 10mg $Co_xMo_{1-x}O_yN_z$/C powders to a mixture of 500 μL Milli-Q water, 500 μL isopropyl alcohol (70% v/v, Aldrich), and 50 μL Nafion (5 wt%, Aldrich), and then sonicating for 30 min to disperse the catalysts in the ink. Afterwards, 15μL of fresh catalyst ink were cast onto a glassy carbon (GC) disk electrode (0.196 cm^2 geometrical areas, Pine Research Instrument) and dried at room temperature. The

typical catalyst loading was about 0.7 mg/cm^2. A conventional three-electrode glass cell was used for all electrochemical measurements at room temperature, with an electrolyte solution of either 0.1 M $HClO_4$ or 0.1 M KOH. In acid solutions, an Ag/AgCl reference electrode was used while a saturated calomel electrode was used in basic solutions, and a Pt foil was used as the counter electrode for all solutions. Cylic voltammetry (CV), rotating disc electrode (RDE), and rotating ring disc electrode (RRDE) measurements were carried out to evaluate ORR activities. CVs were recorded without rotation in solutions saturated with either Ar or O_2 gas. All CV and RDE measurements were carried out from 0.05 to 1.0 V vs. RHE at a scan rate of 10 mV/s. Chronoamperometric testing of $Co_{0.50}Mo_{0.50}O_yN_z$/C was conducted in O_2-saturated 0.1 M $HClO_4$ (0.4 V vs. RHE) and 0.1 M KOH (0.6 V vs. RHE) at room temperature.

All RDE measurements were collected in O_2-saturated solutions with a rotation speed of 100-2500 rpm. The Koutecky-Levich equation was used to determine the number of transferred electrons during oxygen reduction reaction. This equation is expressed as $1/j=1/j_k+1/(B\omega^{1/2})$, where $B=0.62nFC_{O2}D^{2/3}\upsilon^{-1/6}$, j is the measured disk current density, j_k is the kinetic current density, ω is the rotation speed, n is the electron transfer number, F is the faraday constant, C_{O2} is the concentration of dissolved oxygen in electrolyte, D is the diffusion coefficient of dissolved oxygen, and υ is the kinematic viscosity of the electrolyte. C_{O2} is 1.38×10^{-6} mol/cm^3 in 0.1 M $HClO_4$ and 1.20×10^{-6} mol/cm^3 in 0.1 M KOH. D equals 1.67×10^{-5}cm^2/s in 0.1 M $HClO_4$ and 1.90×10^{-5}cm^2/s in 0.1 M KOH. υ is around 0.010 cm^2/s in both electrolytes.

For RRDE measurements, a rotating ring disk electrode with a glassy carbon disk and a Pt ring was used (Pine Instruments). The disk electrode was scanned from 0.05 to 1.0 V vs. RHE at 10 mV/s while holding the ring electrode at 1.2 V vs. RHE in O_2 saturated 0.1 M $HClO_4$ or 0.1 M KOH. The electron transfer number (n) was determined as $n = 4I_d/(I_d+I_r/N)$, and the H_2O_2

peroxide fraction as (4-n)/2, where I_d is disk electrode current, I_r is the ring electrode current, and N is collection efficiency.

2.3 Results and Discussion

2.3.1 Crystal Structure

Catalyst powders with nominal compositions of $Co_xMo_{1-x}O_yN_z$ were synthesized (x = 0.0, 0.25, 0.50, and 0.75) or purchased (x = 1.0) to investigate their potential for ORR electrocatalysis. The soluble cation precursors $Co(NO_3)_2{\cdot}6H_2O$ and $(NH_4)_6Mo_7O_{24}{\cdot}4H_2O$ were reacted under flowing ammonia at relatively low temperatures (773 – 973 K) with the goal of producing rock salt products. Temperatures and reaction times were optimized to minimize the amount of reaction side products (typically Co metal or Co_3Mo_3N). The impurity Co_3Mo_3N was thermodynamically favored at temperatures of 873 K and higher (Figure 2.1a). The less ionic (more metallic) character of Co_3Mo_3N is consistent with the lower chemical potential of nitrogen (μ_N) expected at higher temperatures where the formation of N_2 is entropically favored. Interestingly, Mo did appear to inhibit the formation of Co metal for mixed samples (x = 0.25, 0.50, and 0.75) synthesized at 823K, a temperature at which CoO will completely reduce to Co metal under flowing ammonia. X-ray diffraction patterns of reaction products (Figure 2.1b) showed that the rock salt phase $Co_xMo_{1-x}O_yN_z$ was present for all mixed compositions studied. A closer inspection of the X-ray patterns shows that a substantial amount of Co metal is present in the x = 0.75 sample while a small amount of Co metal can be seen in the x = 0.50 phase, and no Co metal can be resolved in the x = 0.25 pattern. The values of the cubic lattice parameter and the primary particle size obtained from whole-pattern (Le Bail) fitting (Table 2.1) indicate that the cubic lattice parameter decreases with decreasing Co content, though Mo_2N is an outlier from this trend. The primary particle size was found to be about 10 nm for Mo_2N and 4 – 5 nm for the

bimetallic samples, substantially lower than the 30 nm of the purchased CoO. The peak widths of the rock-salt phase were much broader than that of the Co_3Mo_3N structure (77 nm crystallite size) that formed at higher temperatures.

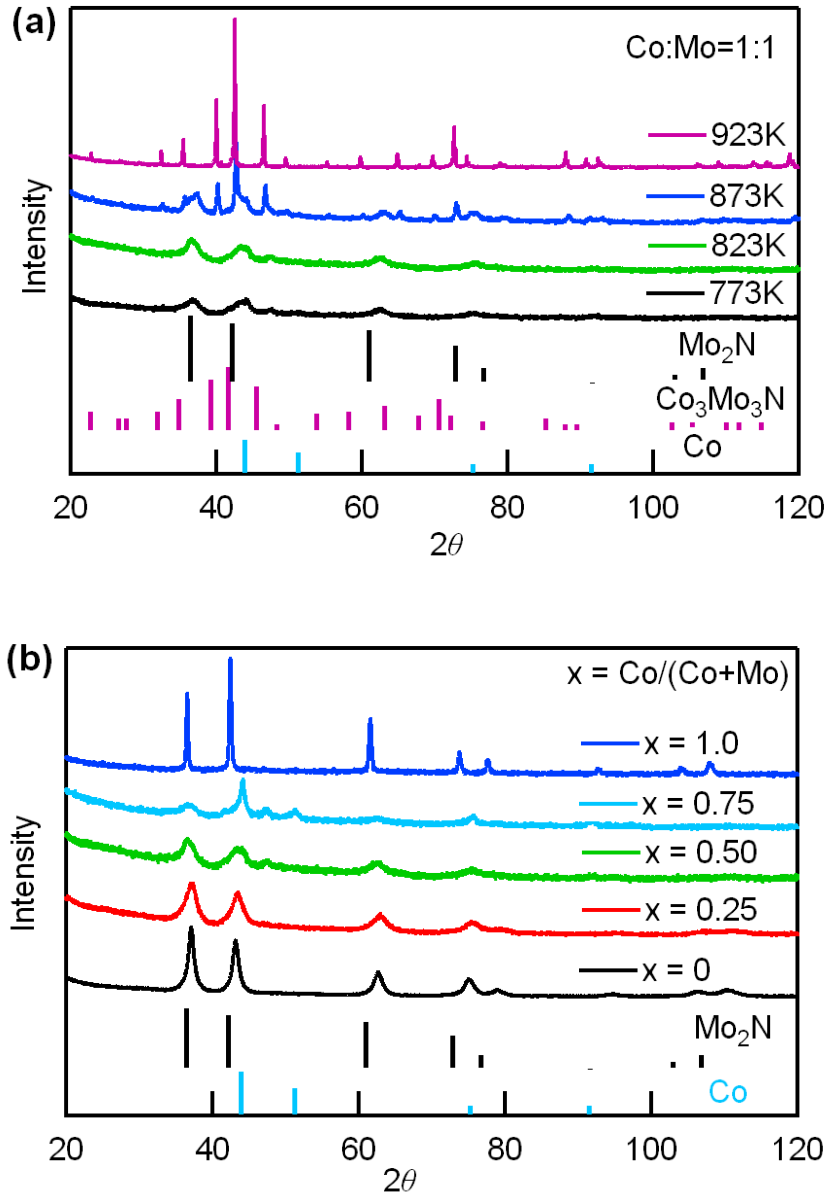

Figure 2.1 (a) XRD patterns of $Co_{0.50}Mo_{0.50}O_yN_z$/C treated from 773 K to 923 K. (b) XRD patterns of $Co_xMo_{1-x}O_yN_z$/C synthesized at 823K with different Co/Mo ratios.

Table 2.1 Lattice parameters and estimated crystallite size of $Co_xMo_{1-x}O_yN_z$/C obtained from Le Bail refinements.

	$x = 0.0$[a]	$x = 0.25$	$x = 0.50$	$x = 0.75$	$x = 1.0$[b]	Co_3Mo_3N
T (K)	973	823	823	823	N/A	923
a (Å)	4.1948(2)	4.149(1)	4.172(3)	4.255(2)	4.2604(1)	11.0386(3)
Crystal Size (nm)	10.1(2)	4.06(7)	4.29(5)	4.6(4)	30.1(1)	77
Strain e_0	0.30(1)	0.4(8)	0.8(4)	N/A	0.05(1)	0.05(2)

[a] Mo_2N. [b] CoO.

2.3.2 Electrochemical Performance

2.3.2.1 ORR Activity in Acid Electrolyte

The ORR activity of carbon-supported $Co_xMo_{1-x}O_yN_z$ compounds was assessed by cyclic voltammetry measurements and rotating disk electrode (RDE) measurements. First, the acidic ORR activities of $Co_{0.50}Mo_{0.50}O_yN_z$ that had been treated at different temperatures were compared (Figure 2.2). The best activity was obtained for the sample treated at 823 K, which had an onset potential of 0.645 V vs. RHE and reached a current density of 4.1 mA/cm^2 at 0.20 V vs. RHE in RDE measurements (Table 2.2), which is close to the diffusion-limited current density expected for a four electron pathway.[111] The ORR activities rapidly drop for samples treated at 873 K and above. The 923 K sample was phase-pure Co_3Mo_3N, which can clearly be seen to be inactive for ORR electrocatalysis. Composition also impacts ORR performance (Figure 2.3 and Table 2.3). The bimetallic oxynitride $Co_{0.50}Mo_{0.50}O_yN_z$ had substantially better activities than binary Mo_2N and CoO which suggests that Co substitution into Mo_2N enhanced its activity for oxygen reduction by about 0.2 V. However, it was discovered that only a portion of the Co was incorporated into the oxynitrides and that the true compositions are Mo-rich relative to the nominal composition, as will be discussed in more details later. The balance of cobalt was

present as metallic Co which has no ORR activity. The compounds $Co_{0.75}Mo_{0.25}O_yN_z$/C and $Co_{0.25}Mo_{0.75}O_yN_z$/C both exhibited ORR activity, though at a rate only slightly higher than that of Mo_2N. The activity of $Co_{0.50}Mo_{0.50}O_yN_z$ is substantially better than reported ZrO_xN_y[117] and TaO_xN_y, [118] whose current densities were only about 50 μA/cm^2 at 0.4 V, far lower than the 3 mA/cm^2 measured for $Co_{0.5}Mo_{0.5}O_yN_z$ at the same voltage.

The $Co_{0.50}Mo_{0.50}O_yN_z$/C catalyst has a moderate activity better than that of binary Mo_2N but lower than that of the well-known standard noble-metal catalysts, as seen in its Tafel slope (Figure 2.4a) of -160 mV/dec, a value significantly larger than that of Pt/C (-87 mV/dec). RDE measurements of $Co_{0.50}Mo_{0.50}O_yN_z$/C (823K) in $HClO_4$ were carried out at rotation speeds of 100-2500 rpm to study its ORR kinetics (Figure 2.4b and c). At low overpotentials, both two and four electron reductions take place. When the potential is lower than 0.35 V vs. RHE, the calculated number *n* of transferred electrons from Koutecky-Levich plot is 3.6. A rotating ring disk electrode (RRDE) measurement was also performed to better understand the ORR mechanism. The peroxide yield between 0.1 to 0.3 V vs. RHE is over 30% and the corresponding *n* is around 3.2, which is lower than the result from the Koutecky-Levich analysis (Figure 2.4d).

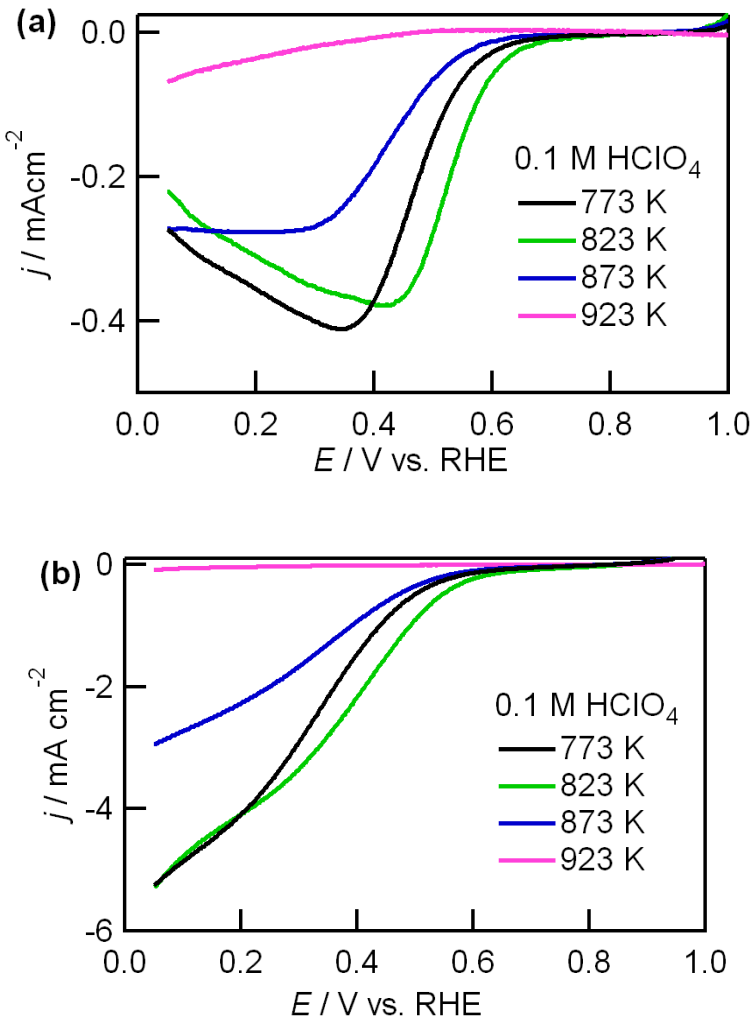

Figure 2.2 ORR data collected in 0.1 M $HClO_4$: (a) linear sweep voltammetry curves (j_{O2}-j_{Ar}) and (b) RDE (1600 rpm) curves of $Co_{0.50}Mo_{0.50}O_yN_z$/C treated between 773K and 923K.

Table 2.2 ORR activities of $Co_{0.50}Mo_{0.50}O_yN_z$/C treated between 773K and 923K in 0.1 M $HClO_4$.

T (K)	773	823	873	923
E_{onset} (V vs. RHE)[a]	0.605	0.645	0.561	0.259
E_{half} (V vs. RHE)[b]	0.376	0.413	0.330	0.185
$j_{0.6V}$ (mA/cm^2)[c]	0.137	0.233	0.100	0.005

[a] E_{onset}, the potential at which the ORR current density | j_{O2}-j_{Ar} | exceeds 25 μA/cm^2. [b] E_{half}, the potential at which the ORR current is 50% of its maximum. [c] $j_{0.6V}$,the ORR current density at E = 0.60 V vs. RHE.

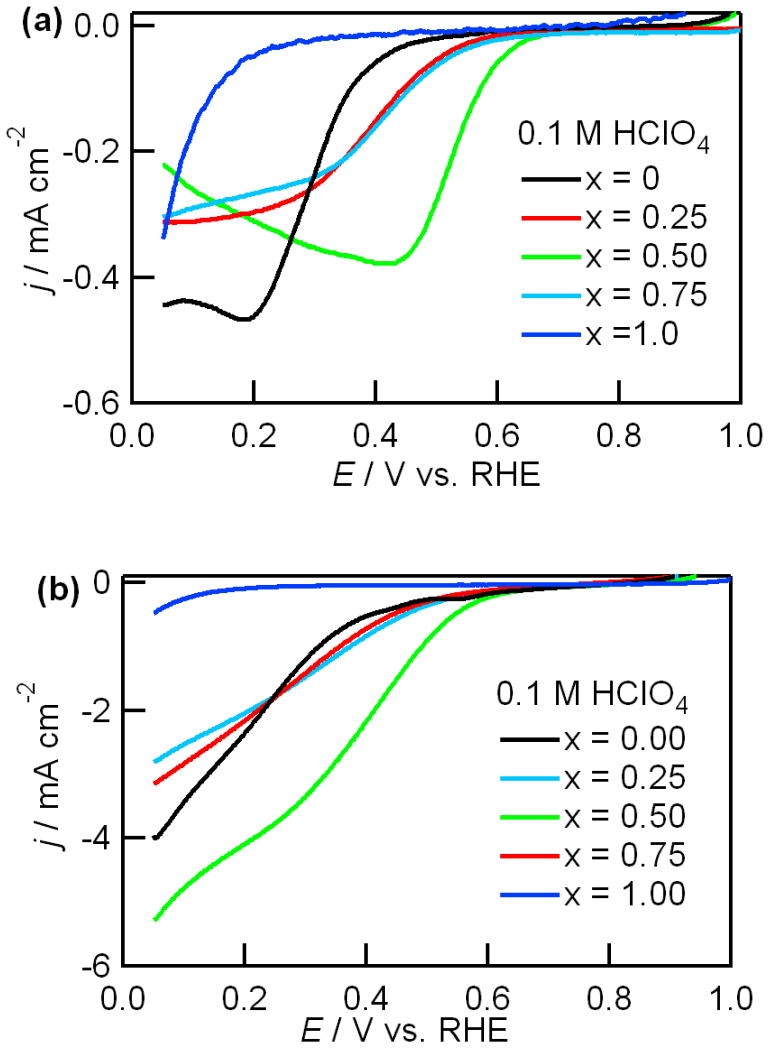

Figure 2.3 ORR data collected in 0.1 M $HClO_4$: (a) linear sweep voltammetry curves (j_{O2}-j_{Ar}) and (b) RDE (1600 rpm) curves of $Co_xMo_{1-x}O_yN_z$/C with different Co/Mo ratios synthesized at 823 K.

Table 2.3 ORR activities of $Co_xMo_{1-x}O_yN_z$/C with different Co/Mo ratios in 0.1 M $HClO_4$.

T (K)	x = 0.0	x = 0.25	x = 0.50	x = 0.75	x = 1.0
E_{onset} (V vs. RHE)	0.472	0.561	0.645	0.587	0.294
E_{half} (V vs. RHE)	0.231	0.295	0.413	0.288	0.111
$j_{0.6V}$ (mA/cm^2)	0.174	0.142	0.233	0.121	0.033

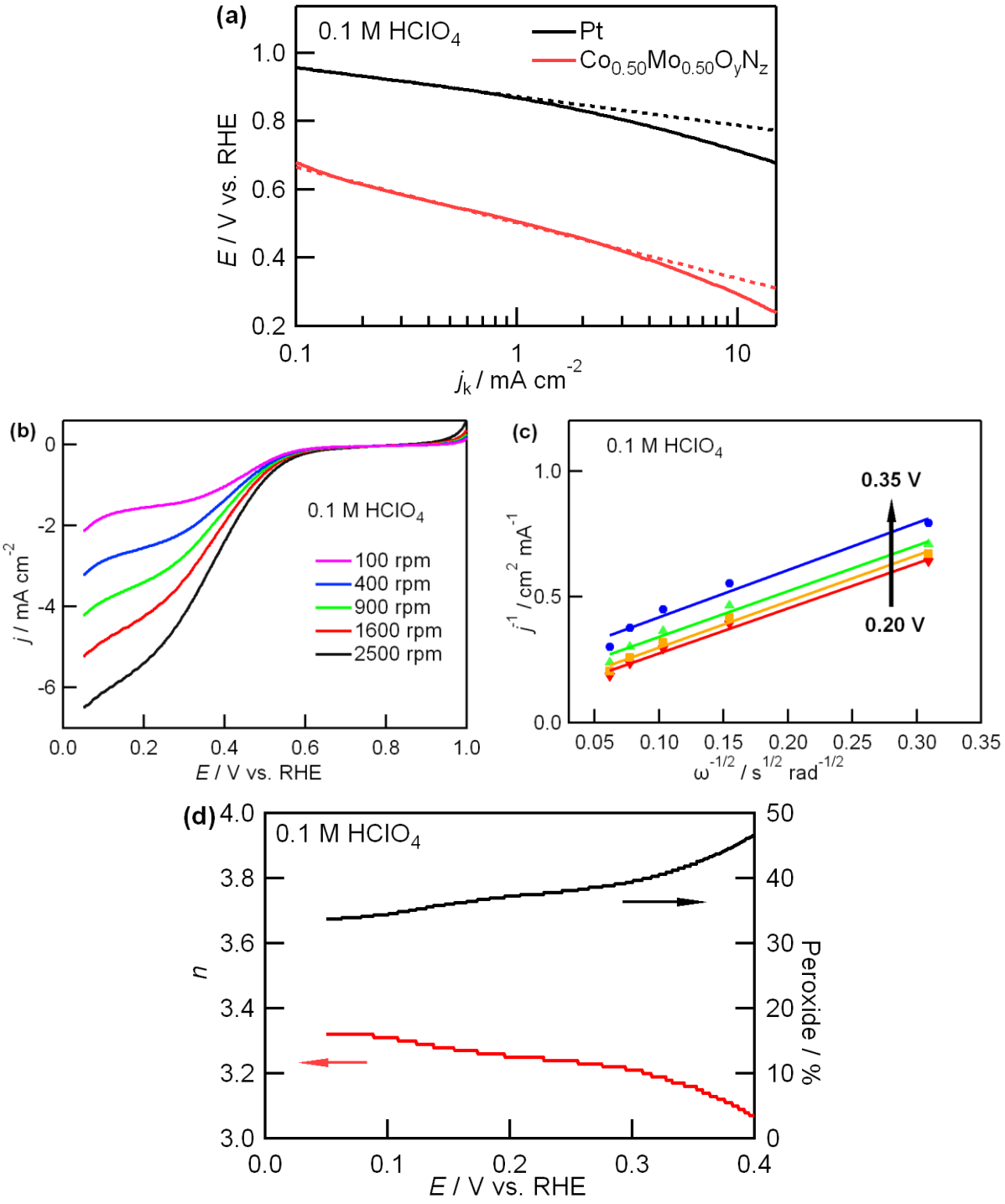

Figure 2.4 In O_2 saturated 0.1 M $HClO_4$: (a) Tafel plots of $Co_{0.50}Mo_{0.50}O_yN_z$/C (823K) and Pt/C. (b) RDE curves of $Co_{0.50}Mo_{0.50}O_yN_z$/C (823 K) with a rotation speed of 100-2500 rpm. (c) Corresponding Koutechy-Levich plots at a potential range of 0.20 to 0.35 V vs. RHE from bottom to top. (d) Percentage of peroxide and the electron transfer number of $Co_{0.50}Mo_{0.50}O_yN_z$/C (823K) based on the RRDE data.

2.3.2.2 ORR Activity in Alkaline Electrolyte

Although $Co_xMo_{1-x}O_yN_z$/C samples have moderate activity in acid, they are exceptionally active in alkaline conditions (pH = 13). Both synthesis temperature and composition impact activity (Fig. 2.5, Tables 2.4 and 2.5). The highest activity is achieved by $Co_{0.50}Mo_{0.50}O_yN_z$/C (823K) with an onset potential as high as 0.918 V vs. RHE and an E_{half} of 0.758 V. This is only about 0.1 V lower than commercial Pt/C samples (Etek) measured under the same conditions here and elsewhere.[111] Among the various non-noble metal systems studied under basic conditions, only perovskite $LaNiO_3$ is clearly better than $Co_{0.50}Mo_{0.50}O_yN_z$/C based on a comparison of onset potentials and currents at fixed potential (Table 2.6). The diffusion-limited current density of $Co_{0.50}Mo_{0.50}O_yN_z$/C is about 4.8 mA/cm^2 which is very close to that of Pt (5.0 mA/cm^2). Above 0.8 V vs. RHE, the Tafel slope is -71 mV/decade (Fig. 2.6a), which is smaller than of Pt/C (-87 mV/dec).

Analysis of Koutecky-Levich plots at potentials of 0.4 – 0.7 V vs. RHE (Fig. 2.6b and 2.6c) gave n = 3.85, indicating a four-electron pathway is the dominant mechanism. RRDE data demonstrated that only 2-4% peroxide was produced, giving n = 3.9 (Fig. 2.6d). Durability testing of $Co_{0.50}Mo_{0.50}O_yN_z$/C (823K) indicates that the sample retains activity after extended operation in both alkaline (24 h at a potential of 0.6 V) and acidic (40 h at a potential of 0.4 V) environments (Fig. 2.7). In order to determine the catalytically active phase, $Co_{0.50}Mo_{0.50}O_yN_z$/C loaded onto carbon paper was analyzed after electrochemical measurements. It is found that the Co-Mo oxynitride phase is retained and identified by XRD after ORR tests in acid or alkaline solution, which indicates the oxynitride is the active phase to catalyze oxygen reduction.

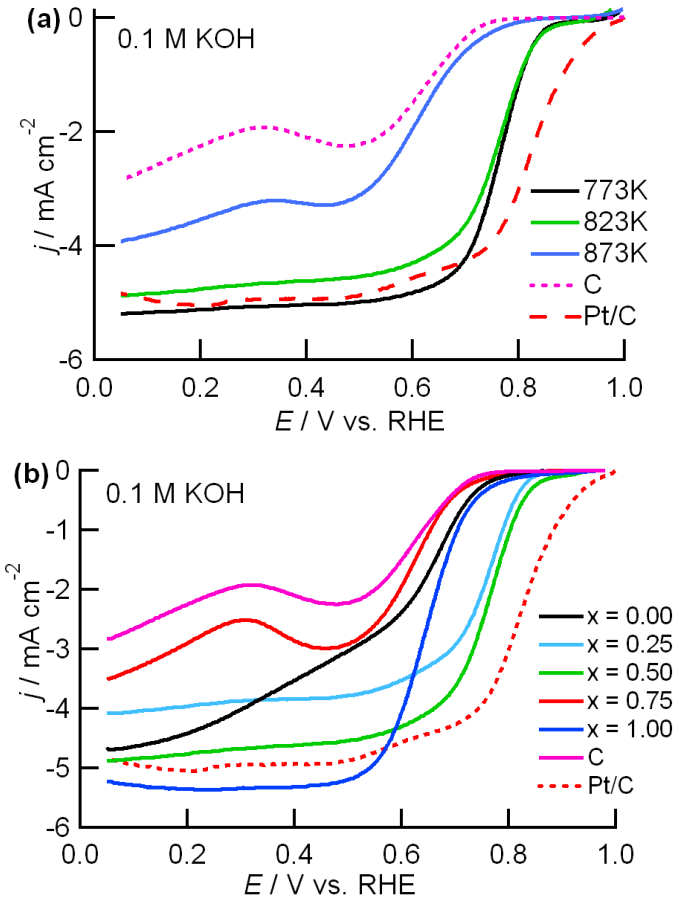

Figure 2.5 In O_2 saturated 0.1 M KOH: (a) RDE curves of $Co_{0.50}Mo_{0.50}O_yN_z$/C treated between 773K and 923K. (b) RDE curves of $Co_xMo_{1-x}O_yN_z$/C with different Co/Mo ratios.

Table 2.4 ORR activities of $Co_{0.50}Mo_{0.50}O_yN_z$/C treated between 773K and 923K in 0.1 M KOH.

T (K)	773	823	873
E_{onset} (V vs. RHE)	0.852	0.918	0.794
E_{half} (V vs. RHE)	0.774	0.758	0.605
$j_{0.6V}$ (mA/cm^2)	4.83	4.30	1.97

Table 2.5 ORR activities of $Co_xMo_{1-x}O_yN_z$/C with different Co/Mo ratios in 0.1 M KOH.

T (K)	x = 0.0	x = 0.25	x = 0.50	x = 0.75	x = 1.0
E_{onset} (V vs. RHE)	0.804	0.857	0.918	0.742	0.866
E_{half} (V vs. RHE)	0.610	0.753	0.758	0.624	0.646
$j_{0.6V}$ (mA/cm^2)	2.39	3.53	4.30	1.96	4.09

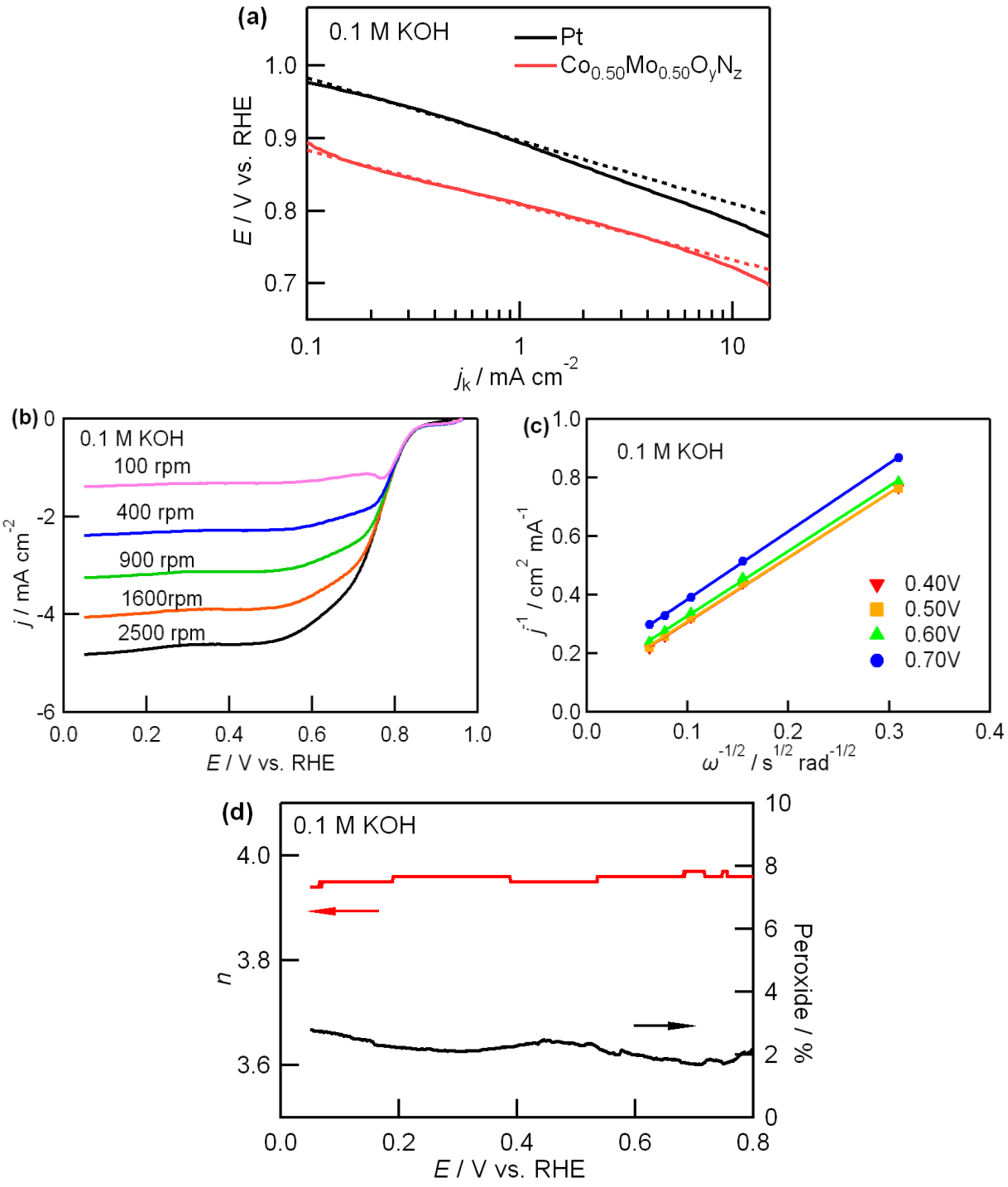

Figure 2.6 In O_2 saturated 0.1 M KOH: (a) Tafel plots of $Co_{0.50}Mo_{0.50}O_yN_z$/C (823K) and Pt/C derived from RDE data. (b) RDE curves of $Co_{0.50}Mo_{0.50}O_yN_z$/C (823 K) with a rotation speed of 100-2500 rpm. (c) Corresponding Koutechy-Levich plots at a potential range of 0.40 to 0.70 V vs. RHE. (d) Percentage of peroxide and the electron transfer number of $Co_{0.50}Mo_{0.50}O_yN_z$/C (823K) based on the RRDE data.

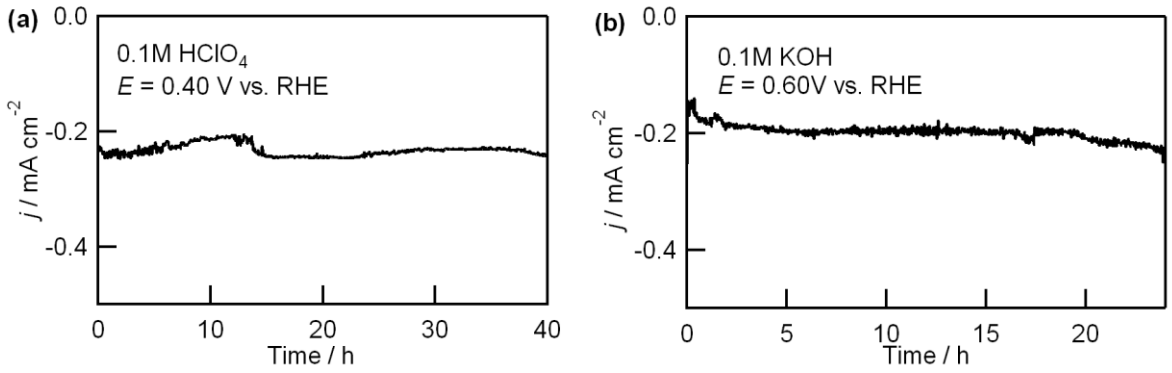

Figure 2.7 (a) Chronoamperometry of $Co_{0.50}Mo_{0.50}O_yN_z$/C (823 K) in O_2 saturated 0.1 M $HClO_4$ (*E* is held at 0.40 V for 40 h). (b) Chronoamperometry of $Co_{0.50}Mo_{0.50}O_yN_z$/C (823 K) in O_2 saturated 0.1 M KOH (*E* is held at 0.60 V for 24 h).

Table 2.6 Summary of ORR activities in 0.1 M KOH for Pt and important non-noble alternatives.

Source	Materials	*E* at j = -1 mA/cm^2 (V vs. RHE)	$j_{0.6V}$ (mA/cm^2)
This work	Pt	0.90	4.60
	$Co_{0.50}Mo_{0.50}O_yN_z$	0.80	4.30
	$Co_{0.25}Mo_{0.75}O_yN_z$	0.78	3.53
Ref. [123]	$LaNiO_3$	~0.87	not provided
	$LaCu_{0.5}Mn_{0.5}O_3$	~0.70	~4.20
	$La_{0.75}Ca_{0.25}FeO_3$	~0.62	~1.30
Ref. [71]	α-MnO_2	~0.80	~1.75
	β-MnO_2	~0.73	~1.30
	γ-MnO_2	~0.66	~1.10
Ref. [111]	CoS-graphene hybrid	~0.80	~4.50

2.3.3 Physical Properties

Based on these ORR results, the composition of $Co_xMo_{1-x}O_yN_z$ can be seen to strongly influence catalytic activity. X-ray diffraction patterns (Figure 2.1) revealed that mixed metal samples contained metallic Co and the true stoichiometry of these materials was likely Mo-rich relative to the nominal stoichiometry. Scanning electron microscopy (SEM), transmission electron microscopy (TEM), X-ray absorption near-edge structure (XANES) and X-ray photoelectron spectroscopy (XPS) measurements were carried out to better understand the properties of nominal $Co_{0.50}Mo_{0.50}O_yN_z$ at the bulk and local scale, and to investigate the actual composition of the rock salt phase present in this material.

2.3.3.1 Morphology

Scanning electron microscopy (SEM, Fig. 2.8a) showed that $Co_{0.50}Mo_{0.50}O_yN_z$ is composed of 0.3 – 1.0 μm particles with surface nanoparticles (20–30 nm) of Co metal, an acid-soluble species which can be removed by washing with perchloric acid (Fig. 2.8b). Energy-dispersive X-ray spectroscopy (EDX) studies find abundant oxygen and nitrogen in the rock salt phase, confirming that it is indeed an oxynitride.

Given the large particle size of the rock-salt phase in SEM experiments, it is surprising that the X-ray coherence length observed for $Co_{0.50}Mo_{0.50}O_yN_z$ (823K) was only about 5 nm. More local TEM studies find that sample heterogeneity exists for even the smallest rock-salt particles (~25 nm). When the thin edge regions of particles were observed, it could be clearly seen that they presented a heterogeneous morphology on a length scale of about 5 nm (Fig. 2.9) which is attributed to sample porosity arising from the reductive elimination (via evaporation) of cobalt metal during processing under reducing conditions (NH_3 flow). Combined STEM-EDX studies were used to probe the Co and Mo distributions over local scale. It is clear that Mo is

distributed evenly through out the whole particle region. In contrast, Co clusters are only observed in the particle interior, suggesting the volatilization of Co readily occurs at the sample surface. Co loss from the exterior of particles is also seen in electron energy loss spectroscopy (EELS) line scan analyses (Fig. 2.10e and f). These scans find Co even outside of the Co-rich clusters proving that the rock salt phase is a true bimetallic compound.

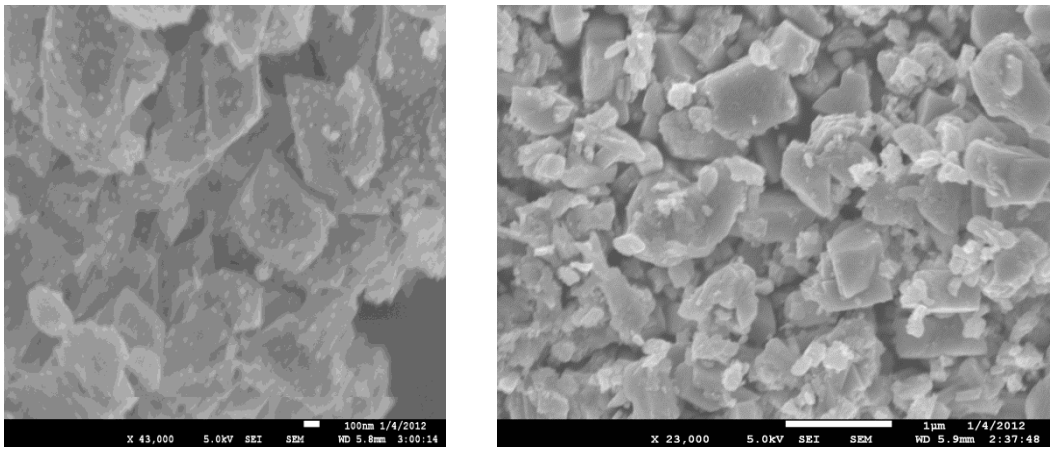

Figure 2.8 (a) SEM image of $Co_{0.50}Mo_{0.50}O_yN_z$ (823K) with smaller surface Co nanoparticles. (b) SEM image of $Co_{0.50}Mo_{0.50}O_yN_z$/C (823 K) after acid leaching.

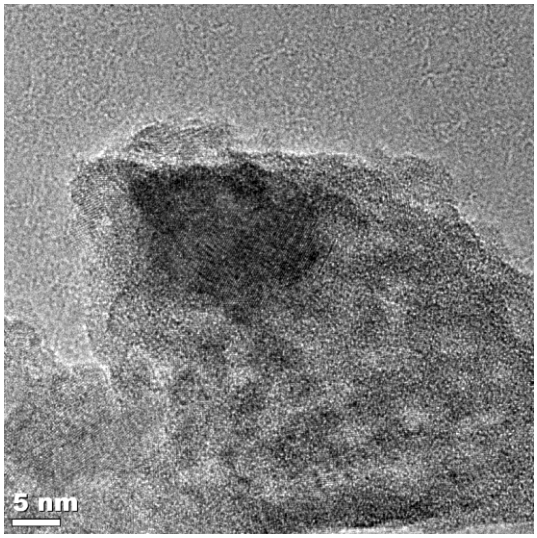

Figure 2.9 TEM image of $Co_{0.50}Mo_{0.50}O_yN_z$ (823K).

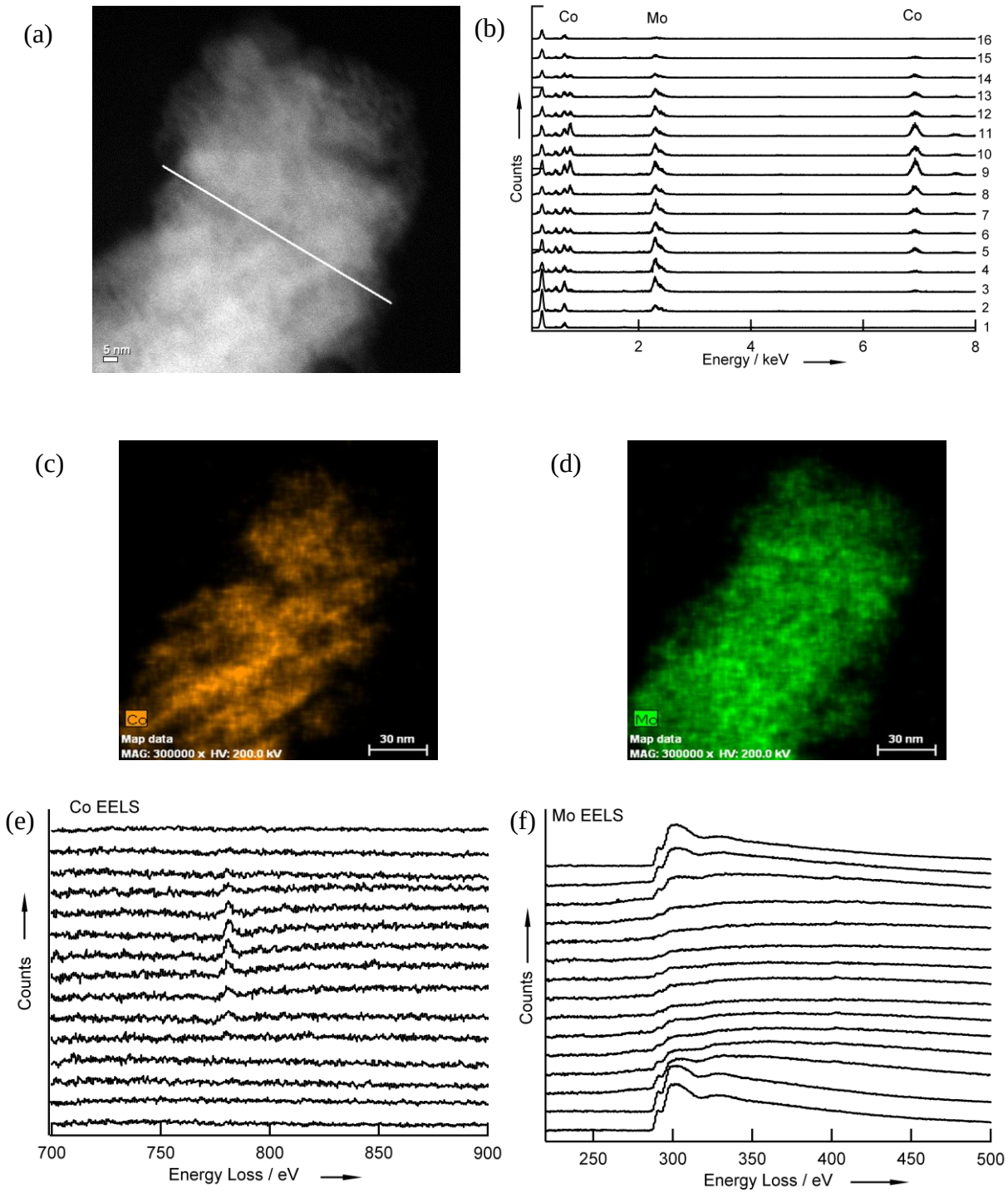

Figure 2.10 (a) STEM image of $Co_{0.50}Mo_{0.50}O_yN_z/C$ (823 K).(b) EDX spectra evenly distributed along a line scan (from left to right) through both Co-poor regions (edge) and Co-rich regions (center) identified through EDX mapping. (c) STEM EDX map of Co distribution. (d) STEM EDX map of Mo distribution. (e) EELS spectra of Co L-edge spectra at points along line scan. Co concentrations are higher in the center relative to the edge. (f) Mo M-edge EELS spectra from line scan. Mo is present at all positions across the line.

2.3.3.2 Bulk Valence State

The valence states of Co and Mo in bulk $Co_xMo_{1-x}O_yN_z$ were analyzed using X-ray absorption near edge spectroscopy (XANES). As seen in Fig. 2.11a, three characteristic features are present in the Co K-edge spectra – a pre-edge peak (~7709 eV), an edge jump (~7717 eV) and a white line (~7725 eV).[124] There is a striking similarity between the patterns of $Co_{0.50}Mo_{0.50}O_yN_z$ and $Co_{0.25}Mo_{0.75}O_yN_z$, suggesting that the Co environments in these samples are very similar. XANES data for $Co_{0.50}Mo_{0.50}O_yN_z$ and $Co_{0.25}Mo_{0.75}O_yN_z$ do not exhibit the isosbestic points that would be expected from a simple mixture of Co metal and CoO, indicating that the catalytically active phase is indeed a distinct bimetallic rock salt compound. In the Mo $L_{2,3}$ edge spectra, $Co_{0.50}Mo_{0.50}O_yN_z$ and $Co_{0.25}Mo_{0.75}O_yN_z$ have a similar Mo environment (Figure 2.11). The oxidation state of Mo in these two compounds is clearly higher than that in the reference compounds Co_3Mo_3N and Mo_2N, and is highest for the $Co_{0.50}Mo_{0.50}O_yN_z$ sample with the highest activity. The splitting of the white line around 2525 eV indicates that Mo may have an octahedral environment in these oxynitrides,[125] as would be expected for the rock salt structure.

An extended X-ray absorption fine structure (EXAFS) study of the Co K-edge can clearly distinguish between coordination environments of Co metal and ionic Co. Fitting was carried out for the first coordination shell (Fig. 2.12), which was modelled using Co-Co and Co-O paths. The calculated bond lengths between cobalt and anion for both samples (Table 2.7) are consistent with those deduced from the lattice parameters obtained from Le Bail fits of X-ray diffraction data. The EXAFS data for both $Co_{0.50}Mo_{0.50}O_yN_z$ and $Co_{0.25}Mo_{0.75}O_yN_z$ show a strong peak at about 2.48 Å indicative of the Co-Co bonding in Co metal. There is a shoulder at lower distances that can be well fit by assuming a component with octahedral coordination of Co that refines to

55% and 66% of the Co species in the x = 0.50 and 0.25 samples, respectively. The true compositions are thus $Co_{0.18}Mo_{0.82}O_yN_z$ for x = 0.25 and $Co_{0.35}Mo_{0.65}O_yN_z$ for x = 0.50. It is therefore concluded that the incorporation of CoO into the rock-salt structure of Mo_2N occurs and is necessary for the enhanced ORR activity.

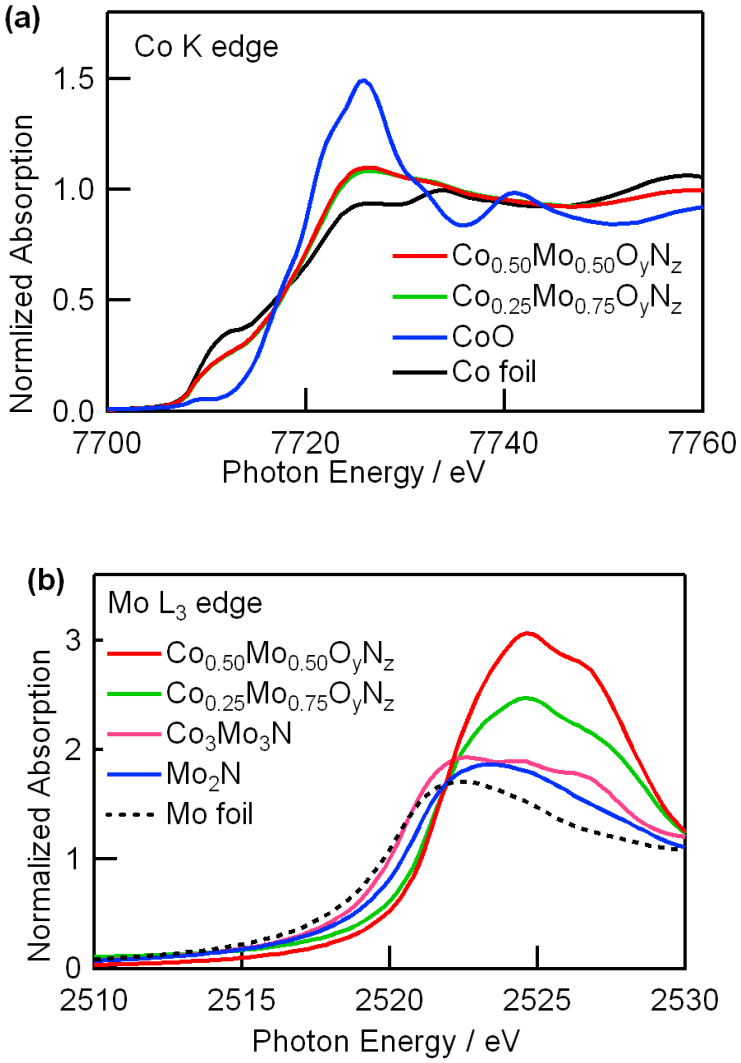

Figure 2.11 XAFS studies of most active $Co_{0.50}Mo_{0.50}O_yN_z$/C sample. (a) XANES spectra near the Co K-edge indicating mix of metallic and divalent Co. (b) XANES spectra near the Mo L_3-edge, demonstrating that Mo valence is slightly higher than in Mo_2N.

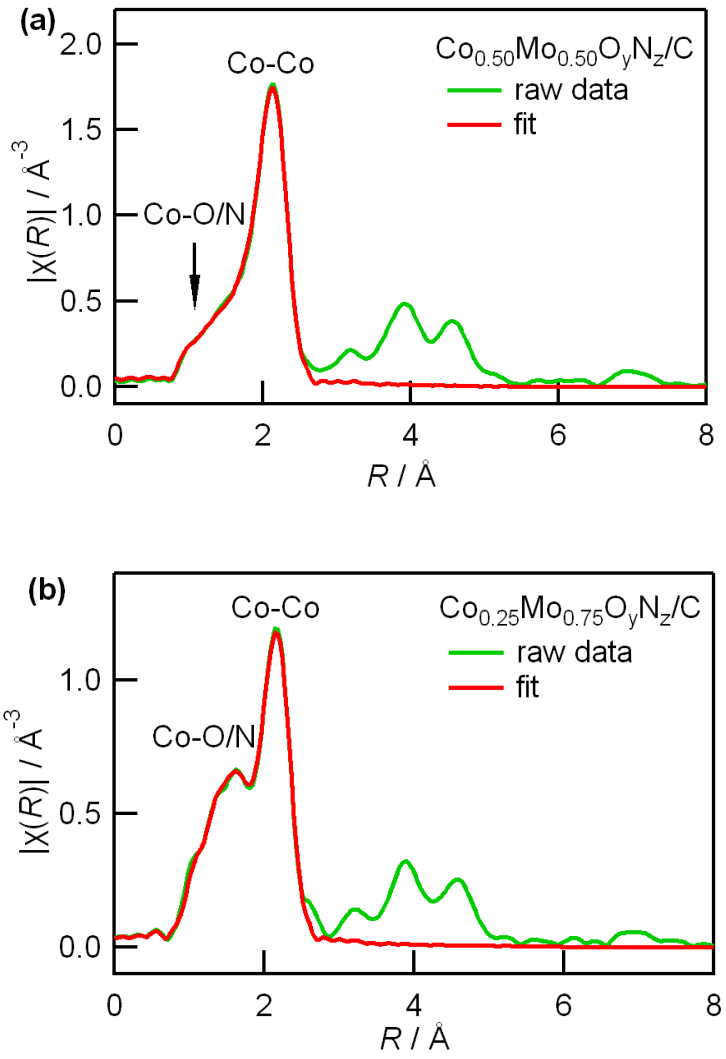

Figure 2.12 Co K-edge EXAFS spectra of (a) $Co_{0.50}Mo_{0.50}O_yN_z/C$ and (b) $Co_{0.25}Mo_{0.75}O_yN_z/C$ in *R* space.

Table 2.7 EXAFS analysis of $Co_xMo_{1-x}O_yN_z/C$ (x = 0.50 and 0.25).

	x = 0.25	x = 0.50
Fraction of Co-O/N	0.66 (±0.03)	0.55 (±0.02)
R (Å)	2.06 (±0.04)	2.02 (±0.04)
Composition	$Co_{0.18}Mo_{0.82}O_yN_z$	$Co_{0.35}Mo_{0.65}O_yN_z$

2.3.3.3 Surface Valence State

XPS measurements were performed to further explore the properties on the surface. The Co $2p_{3/2}$ data collected for $Co_{0.50}Mo_{0.50}O_yN_z/C$ (823K) and $Co_{0.25}Mo_{0.75}O_yN_z/C$ (823K) samples exhibited a dominant peak at 781.6 eV due to Co-O or Co-N species (Fig. 2.13a), consistent with bulk EXAFS results. An additional peak due to Co-OH species that form when Co metal is exposed to air was also commonly observed. The complete absence of metallic Co^0 in the XPS signal of the catalytically active rock salt phases can be attributed to two factors – either the facile evaporative loss of this species at the outer few nanometers of catalyst particles, or its complete oxidation to CoO upon air exposure. This is in clear contrast to the catalytically inactive phase Co_3Mo_3N, whose Co 2p XPS data exhibits a third low energy Co species (778.4 eV) which is due to covalent Co^0 rather than ionic Co^{n+}, as expected from the stoichiometry of this compound.The C 1s data for carbon black treated under NH_3 (Fig. 2.13b) showed no oxygen and nitrogen on the carbon surface. The observed oxygen and nitrogen species must instead be on the catalyst, proving that the catalytically active surface (and not just the bulk) is an oxynitride.

The Mo 3d XPS data is consistent with XPS data reported for other molybdenum nitrides.[126] Deconvoluting the concentration of each Mo species is complicated by the presence of dual Mo peaks for each individual species due to excitation of both Mo $3d_{5/2}$ and Mo $3d_{3/2}$ electrons. The separation and relative intensities of the Mo $3d_{5/2}$ and Mo $3d_{3/2}$ peaks, were estimated using a pure MoO_3 reference sample, which gave two peaks with a 3.1eV apart and with an intensity ratio of 65%/35%. This separation of ~3.1eV indicates that the measured low energy Mo $3d_{5/2}$ species, located at 229 and 230 eV, have a corresponding Mo $3d_{3/2}$ peak at 232.1 and 233.1 eV. These higher energy Mo $3d_{3/2}$ peaks directly overlap with the Mo $3d_{5/2}$ peak

located at 232.8 eV for Mo^{6+}. The known ratio of Mo $3d_{5/2}$ / $3d_{3/2}$ was therefore used to deconvolute the contribution of overlapping peaks at these energies. XPS indicated that the top few nanometers of $Co_{0.50}Mo_{0.50}O_yN_z$/C and $Co_{0.25}Mo_{0.75}O_yN_z$/C samples contained about 17 at% $Mo^{2/3+}$, 30 at% $Mo^{3/4+}$, and 53 at% Mo^{6+}. This ratio remained essentially unchanged after air exposure indicating that the reduced Mo species are quite stable (Fig. 2.13c), indicating that the synthesis temperature (and presumably the overall sample stoichiometry) was the major factor determining the Mo valence. Interestingly, $Co_{0.50}Mo_{0.50}O_yN_z$/C (773K) did not contain the lowest oxidation state $Mo^{2/3+}$ species. This Mo data, along with the Co data, indicates reactions at higher temperatures clearly lead to a preferential reduction in the Mo valence on the surface; Co seems unaffected. The 823K sample with $Mo^{2/3+}$ performs better activity than the 773K sample without $Mo^{2/3+}$. This suggests that the Mo oxidation state is closely correlated with the electrochemical activity of the rock salt phase, and it is hypothesized that there are viable substitutional strategies which will give an optimal Mo valence and provide new routes to increase the activity.

The N 1s data demonstrates that there are significant concentrations of nitrogen species near the surface (Fig. 2.13d). Significant peak overlaps are observed for the Mo $3p_{3/2}$ and N 1s species (~394-399 eV). Using the MoO_3 data to correct the Mo 3p signals, it is possible to identify two unique N 1s species, Co/Mo-N (~397.6 eV) and N-H (~399.3 eV). This data confirms the formation of metal-nitride bonds as well as the presence of residual NH bonds which are due to either the incomplete reaction of NH_3 or a reaction with atmospheric water. By extracting the Mo signal from the N 1s peak, it was possible to estimate the surface composition (Table 2.8 and 2.9). The net Co:Mo ratio for $Co_{0.50}Mo_{0.50}O_yN_z$/C and $Co_{0.25}Mo_{0.75}O_yN_z$/C were approximately 1:1 and 1:3, consistent with the nominal stoichiometries. Analysis of the O to N ratios revealed that the $Co_{0.50}Mo_{0.50}O_yN_z$/C was richer in oxygen (33.5:45.1 at%) than the

$Co_{0.25}Mo_{0.75}O_yN_z/C$ (27.9:54.2 at%). This confirms that Mo is more reactive towards N than Co, as expected based on the compositions of the binary end members.

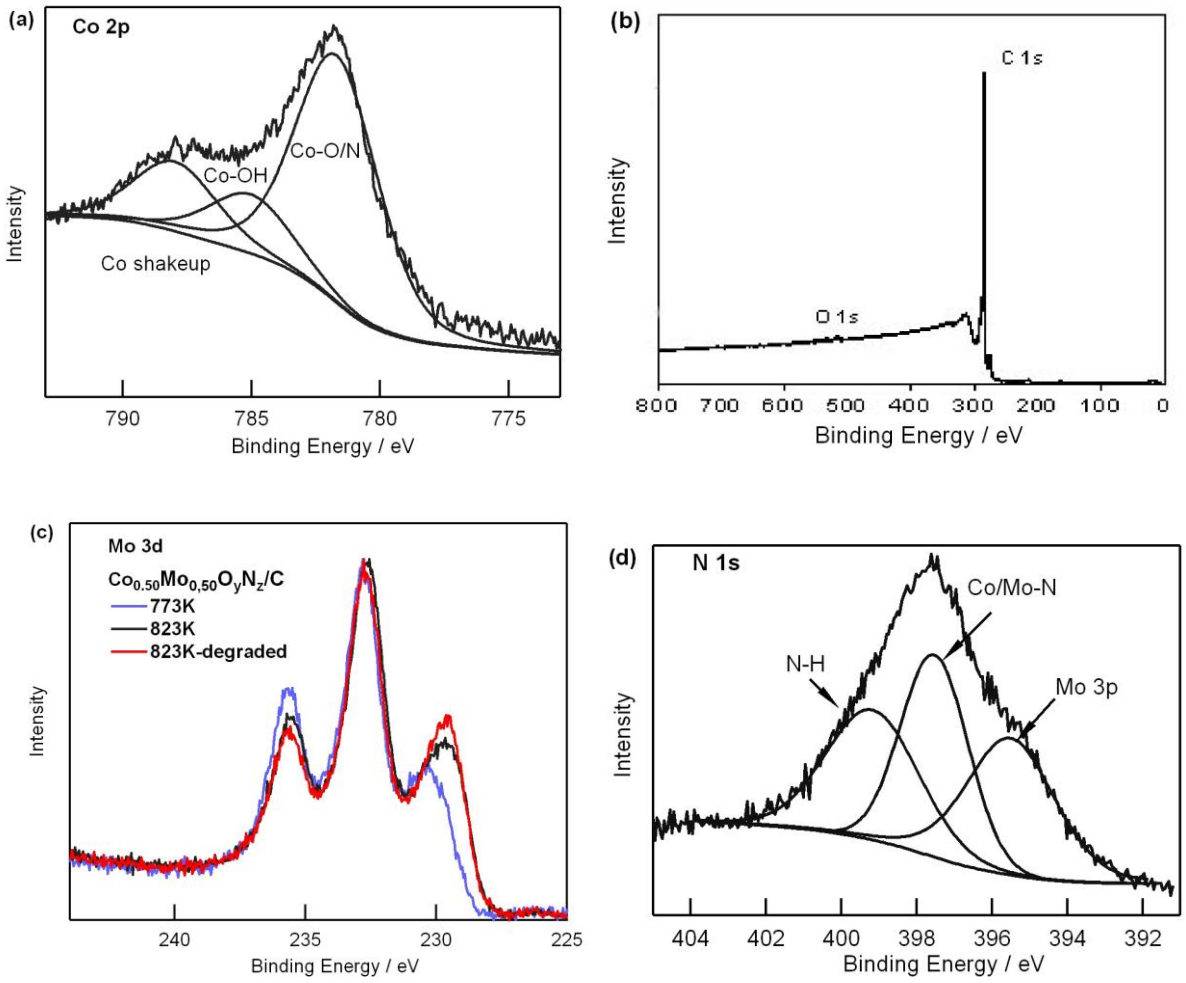

Figure 2.13 (a) Co 2p XPS data collected for $Co_{0.50}Mo_{0.50}O_yN_z/C$ (823 K). (b) C 1s XPS data collected for carbon black treated in NH_3. (c) Comparison of Mo 3d XPS data collected for $Co_{0.50}Mo_{0.50}O_yN_z/C$ (823 K) as synthesized and after air exposure for one month, and for $Co_{0.50}Mo_{0.50}O_yN_z/C$ (773 K). (d) N 1s XPS data collected for $Co_{0.50}Mo_{0.50}O_yN_z/C$ (823 K).

Table 2.8 XPS analysis of $Co_xMo_{1-x}O_yN_z/C$ (x=0.50 and 0.25), MoO_3, Co_3Mo_3N, and carbon black treated under NH_3 at 823K. All samples were studied as synthesized, except for those marked as "degraded" (extended air exposure of ~ 1 month) or as "after ORR".

Sample	Mo $3d_{5/2}$ Mo^0	Mo $3d_{5/2}$ $Mo^{2+/3+}$	Mo $3d_{5/2}$ $Mo^{3+/4+}$	Mo $3d_{5/2}$ / $3d_{3/2}$ Mo^{6+}	Co $2p_{3/2}$ Co^0	Co $2p_{3/2}$ Co-O/N	Co $2p_{3/2}$ Co^{3+}-O/N	Co $2p_{3/2}$ Co-OH
x=0.50 w/CB 773K			230.29	232.83		781.67		785.33
% [a]			35.4	64.6		76.3		23.7
x = 0.50 w/CB 823K		229.24	230.1	232.82		781.78		785.36
% [a]		22.8	23.0	57.6		81.6		18.4
x = 0.50 w/out CB 823K		229.11	230.12	232.41		781.26		784.76
% [a]		19.2	29.7	51.1		78.7		21.3
x = 0.50 823K after ORR test in KOH		229.76	230.70	232.45		781.29		784.27
% [a]		18.1	14.0	67.9		74.2		25.8
x= 0.50 w/ CB 823K - degraded		229.48	230.55	232.83		781.68		785.02
% [a]		26.7	25.2	48.0		80.7		19.3
x = 0.25 w/ CB 823K		229.26	230.32	232.87		781.79		785.51
% [a]		16.9	31.7	51.4		82.1		17.9
x=0.25 w/ CB 823K - degraded		229.23	230.34	232.86		781.90		784.90
% [a]		17.4	28.3	54.3		75.8		24.2
Co_3Mo_3N	227.77	228.86	231.09	232.25	778.39	781.16	783.54	
% [a]	26.7	28.6	39.9	4.8	24.0	51.7	24.3	
MoO_3				233.13				
% [a]				100				

Sample	Mo $3p_{3/2}$	Mo $3p_{3/2}$	N 1s Co/Mo-N	N 1s NH	O 1s Co/Mo-O	O 1s Co/Mo-OH or C-O
x = 0.50 w/ CB 773K		395.38	397.55	398.56	530.64	532.09
% [b]			67.1	22.9	74.1	25.9
x = 0.50 w/ CB 823K		395.41	397.52	399.37	530.69	531.98
% [b]			64.6	35.4	74.1	25.9
x = 0.50 w/out CB 823K		395.52	397.54	399.19	530.84	532.37
% [b]			53.0	47.0	77.1	22.9
x = 0.50 823K after ORR test in KOH		395.593	398.08	400.07	[c]	
% [b]			71.3	28.7		
x = 0.50 w/ CB 823K - degraded	394.87		396.91	398.85	530.29	531.98
% [b]			66.6	33.4	78.9	21.1
x = 0.25 w/ CB 823K		395.38	397.59	399.54	530.72	531.98
% [b]			64.0	36.0	70.4	29.6
x = 0.25 w/ CB 823K - degraded		395.28	397.54	399.42	530.94	532.71
% [b]			54.4	45.6	80.6	19.4
Co_3Mo_3N	393.81	395.64	397.73	399.79	530.46	533.10
% [b]			83.7	16.3	90.0	10.0

[a] Due to the overlap of the Mo $3d_{3/2}$ signals from the $Mo^{2/3+}$ and $Mo^{3/4+}$ species with the Mo$3d_{5/2}$ signal of Mo^{6+}, the concentrations of $Mo^{2/3+}$, $Mo^{3/4+}$ and Mo^{6+} species were estimated by measuring the Mo $3d_{5/2}$ and Mo $3d_{3/2}$ signals, using a least squares fit for MoO_3, and calculating the relative intensity of these two signals (Mo $3d_{5/2}$:Mo $3d_{3/2}$ = 1.8). This factor was used to estimate the Mo $3d_{3/2}$ intensity from the $Mo^{2/3+}$ and $Mo^{3/4+}$ species, which overlap with the Mo $3d_{5/2}$ signal for Mo^{6+} (~233 eV). The percent of each Mo^{6+} surface species was then estimated by subtracting the calculated Mo $3d_{3/2}$ signal from the $Mo^{2/3+}$ and $Mo^{3/4+}$ species, then normalizing the percent species to this calculated value.

[b] N concentrations calculated removing Mo 3p component.

[c] O 1s signal for sample after ORR test is affected by Nafion component mixed in the sample. The actual O percentage in the sample can not be accurately determined.

Table 2.9 Atom fractions calculated from XPS analysis of $Co_xMo_{1-x}O_yN_z/C$ (x =0.50 and 0.25), MoO_3, Co_3Mo_3N, and carbon black treated under NH_3 at 823K.

Sample	C:Co:Mo:O:N	Co:Mo:O:N
x = 0.50 w/ CB 773K	59.7 – 4.5 – 4.0 – 15.2 – 16.7	11.5 – 9.7 – 38.7 – 40.1
x = 0.50 w/ CB 823K	52.1 – 5.2 – 5.7 – 16.4 – 20.6	9.9 – 11.4 – 33.5 – 45.1
x = 0.50 w/out CB 823K	12.3 – 8.8 – 10.7 – 30.5 – 37.8	10.0 – 12.1 – 34.8 – 43.1
x = 0.50 w/CB 823K - degraded	53.3 – 4.8 – 5.6 – 15.7 – 20.8	10.3 – 12.1 – 33.7 – 43.9
x = 0.25 w/ CB 823K	66.1 – 1.9 – 6.0 – 12.3 – 13.8	4.9 – 13.0 – 27.9 – 54.2
x = 0.25 w/ CB 823K - degraded	62.9 – 2.1 – 5.1 – 11.9 – 18.1	5.5 – 13.6 – 32.0 – 48.8
Co_3Mo_3N	15.8 – 15.1 – 13.7 – 35.0 – 20.3	18.0 – 16.3 – 41.6 – 24.2
Carbon black in NH_3	100.0 – 0 – 0 - 0 – 0	

2.4 Conclusions

In conclusion, non-noble $Co_xMo_{1-x}O_yN_z/C$ catalysts exhibit moderate ORR activity in acidic conditions and superb activity in alkaline conditions which is only 0.1 V away from the performance of Pt/C. The oxynitrides were synthesized by a solution impregnation method followed by ammonolysis at medium temperatures. Samples of nominal composition $Co_{0.50}Mo_{0.50}O_yN_z/C$ treated at 823K demonstrated the best activity (E_{onset} = 0.918 V vs. RHE in base and E_{onset} = 0.645 V vs. RHE in acid). Koutechy-Levich and RRDE analysis indicated that a four-electron or nearly four-electron pathway for ORR occurred in acid at low potential range and in alkaline at relatively high potential range. Chonoamperometry measurements indicated that the oxynitride remained active and stable after long-term operation. EDX and EELS studies in STEM mode clearly showed that Mo was distributed throughout the particle while Co clusters were distributed in the interior region, suggesting the formation of Mo-rich oxynitride which is in consistent with XRD and EXAFS analysis. Although some cobalt metal is invariably formed during syntheses, ionic cobalt is demonstrated to be integrally substituted into the rock-salt structure in the bulk and on the surface to form a bimetallic cobalt molybdenum oxynitride with nanoscale (~5 nm) texture that is catalytically active for oxygen reduction. It is suggested that strategies for tuning the metal oxidation states within the oxynitride phase are likely to lead to further enhancements in ORR activity with the potential of matching or exceeding the activity of Pt.

Chapter 3. Binary Molybdenum Nitride Electrocatalyst for Oxygen Reduction Reaction

3.1 Introduction

Investigating efficient and effective electrocatalysts using renewable energy as a conversion resource to satisfy the incremental worldwide energy demand has become increasingly important. Hydrogen fuel cells such as polymer electrolyte membrane fuel cells (PEMFCs) have been attracted intensive research attentions due to its high specific energy density and low operating temperature. In PEMFCs, it is more difficult to catalyze oxygen reduction reaction (ORR) on the cathode due to the sluggish kinetics of 4-electron reaction compared to the 2-electron anode reaction. Platinum and platinum related alloys have been considered and used as efficient cathode catalysts for ORR in PEMFCs.[18] However, the high cost of and tremendous scarcity of platinum remain to be obstacles for the commercialization of PEMFCs. The development of alternative non-noble metal based catalysts is highly desirable. Transition metal macrocycles, oxides, carbides and nitrides have been widely investigated for ORR catalysis.[27,127-129] Transition metal catalysts in Group 4-5 such as zirconium oxide, titanium nitride and tantalum oxynitride showed slight ORR activities but excellent stabilities in acidic electrolyte.[27,130] Transition metal macrocycles containing Co, Fe or Cu have shown a good ORR activity and long-term durability which is comparable to Pt.[128]

Another group as promising alternatives to Pt for catalysis applications is transition metal nitrides, as they can have both low electrical resistance and good corrosion resistance.[27] Compared to oxide, the surface of the nitride is modified by the formation of metal-nitrogen bonding. It is easier to donate electrons to oxygen molecule on the nitride surface, which facilitates the process of ORR. Previously, both MoN and Mo_2N have been demonstrated to exhibit ORR activities and to proceed oxygen reduction by a nearly four electron process in

PEMFCs.[46,116,131] Preliminary durability tests suggested that no decay in performance was observed for Mo_2N (60 h) and MoN (10 h) in 0.5 M H_2SO_4.[97,98] Therefore, further modifications of these molybdenum nitrides may enhance its activity and/or stability.

In acidic condition, the ORR activity of MoN is higher than that of Mo_2N. Density functional theory studies indicate that the hexagonal crystal structure and suitable geometric site of MoN facilitate oxygen adsorption and lead to the enhanced ORR activity relative to Mo_2N.[131] It is worthwhile to study the correlation between crystal structure and ORR activity of molybdenum nitride. Monometallic molybdenum nitrides are reported to typically have stable structures which are based on simple close-packed geometries. One such compound is cubic Mo_2N which has a face centered (fcc) rock salt structure with an ABC repeat sequence of layers. The coordination environment of Mo within the rock salt structure would consist of only MoN_6 octahedra if nitrogen site was fully occupied. However, the nitrogen site is only half-occupied when the Mo : N stoichiometric ratio is 2 : 1, so it is expected that Mo cations have a reduced coordination number, an ususualy geometry which is perhaps stabilized by the low average Mo valence of +1.5. Another compound with only octahedral local environments is δ_3-MoN with the NiAs structure type that has the simple two-layered hexagonal close packed (hcp) stacking of octahedral layers in an AB sequence. δ_1-MoN has an X-ray diffraction pattern that is nearly indistinguishable from that of δ_3-MoN, however, it has been reported to have a structure based on the WC prototype (only A layers) in which Mo is found exclusively in a trigonal prismatic MoN_6 environment. By modifying synthesis condition or doping additional transition metal element, mixture of trigonal prisms and octahedra can be achieved in Mo_5N_6 and $(Fe_{0.8}Mo_{0.2})MoN_2$.[132-134] Comparing ORR activities of molybdenum nitrides with various MoN_6 coordination environments will help to understand the structural impact on catalytic activity.

In this study, molybdenum nitrides with different prototypes were selected as cathode catalysts toward ORR in acidic electrolyte. The relationship among crystal structure, morphology, electronic structure and ORR activity have been studied.

3.2 Experiment Section

3.2.1 Sample Preparation

A series of bulk molybdenum nitride samples were prepared by ammonolysis of different molybdenum precursors at elevated temperatures as reported earlier (Table 3.1).[132] Various precursors such as MoO_3 (99.95%, Alfa Aesar) and $(NH_4)_6Mo_7O_{24}\bullet 4H_2O$ (99.997%, Alfa Aesar) can be used to prepare Mo_2N. The oxide precursor was heated under NH_3 at 5°C/min to 250°C, 0.5°C/min to 350°C, 2.5°C/min to 700°C and held at 700°C for 3 hours. δ-MoN was synthesized by treating $MoCl_5$ under NH_3 at 5°C/min to 600°C. The precursor was held at 600°C for 3 hours and then quenched to room temperature. It should be noted that $MoCl_5$ will react with moisture and will be partially oxidized immediately when it is exposed to air. Precursor with partial oxidation leads to a mixture of δ-MoN and Mo_2N as the final product. Mo_5N_6 was synthesized by heating MoS_2 under NH_3 at 5°C/min to 750°C for 20 hours.

Table 3.1 Synthesis conditions for molybdenum nitrides.

Sample	Precursor	Reaction Temperature (°C)	Reaction Time (h)	Gas flow rate (cm^3/min)
Mo_2N	MoO_3	700	3	50
δ-MoN	$MoCl_5$	600	3	50
Mo_5N_6	MoS_2	750	20	100

3.2.2 Characterization

X-ray powder diffraction patterns (XRD) were obtained from a D8 Advance X-ray diffractometer (Bruker, AXS, λ = 1.54 Å) with a LynxEye detector set to a diffraction radius of 300 mm. Scans were collected using a fixed divergence slit width of 0.6 º, a 2θ range of 7 to 120 º and a collection time of 1.5 s per step. Time-of-flight neutron diffraction measurements were performed by use of the nanoscale-ordered materials diffractometer (NOMAD) at the Spallation Neutron Source (SNS), Oak Ridge National Laboratory. Approximately 100 mg of powder samples were loaded into a capillary (Φ = 2mm), with a data acquisition time of 100 mins for a total proton charge of 5.4×10^{12}. Both neutron diffraction and neutron pair distribution function (NPDF) data were generated using the IDL software package developed for NOMAD instrument. High resolution synchrotron data were obtained at beamline 11-BM (λ = 0.413832 Å) at the Advanced Photon Source (APS) of Argonne National Laboratory as samples were loaded into a 0.8 mm diameter Kapton capillary. TOPAS software package (Version 4.2, Bruker AXS) was used for Le Bail and Rietveld refinements of X-ray and neutron diffraction data.

Scanning electron microscopy (SEM) analysis was carried out on a JEOL 7600F high resolution microscope with an energy-dispersive X-ray spectroscopy (EDX). Transmission electron microscopy (TEM) was performed on a JEOL 1400 microscope operated at an accelerating voltage of 120 kV. Thermogravimetric analysis (TGA) was performed using a Q5000 (TA instruments) to determine sample anion contents. TGA experiment was ran under flowing O_2 (25 mL/min) with a ramp rate of 5 °C/min from room temperature to 150 °C, held for 1 hour; then from 150 °C to 500 °C and held for 2 hours. Alternating current (ac) susceptibility measurements were carried out using the Quantum Design Magnetic Property measurement system. Powder samples were placed in standard gelatin capsules and then cooled to 2K at zero

magnetic field. The temperature dependence of ac susceptibility was measured at a static magnetic field of 2 Oe.

3.2.3 Electrochemical Measurements

Catalyst inks for electrochemical testing were prepared by adding a mixture of 2 mg nitride sample and 2 mg carbon black (Vulcan XC72) to a solution of 500 μL Milli-Q water, 500 μL isopropyl alcohol (70% v/v, Aldrich), and 50 μL Nafion-117 (5 wt%, Aldrich), and then sonicating for 30 min to disperse the catalysts in the ink. Afterwards, 25μL of fresh catalyst ink was dropped onto a glassy carbon (GC) disk electrode (0.196 cm^2 geometrical area, Pine Research Instrument) and dried at room temperature. All electrochemical measurements were conducted in a three electrode conventional glass cell with an electrolyte solution of 0.1 M $HClO_4$. Ag/AgCl was used as reference electrode and Pt foil was used as auxiliary electrode. Both cyclic voltammetry (CV) and rotating disc electrode (RDE) measurements were performed by sweeping from 0.05 to 1.0 V vs. RHE at a scan rate of 10 mV/s. CVs were recorded in acid solution saturated with either Ar or O_2 gas. RDE measurements were collected in O_2-saturated solution with a rotation speed of 1600 rpm.

3.3 Results and Discussion

3.3.1 ORR activities of molybdenum nitrides

ORR activity of molybdenum nitride is strongly dependent on its crystal structure. There are two stable classes of molybdenum nitride structures those based on face centered cubic Mo_2N or on hexagonal nitrides including different polytypes of δ-MoN and Mo_5N_6. Previous studies demonstrate that the preferred geometry of hexagonal structure is more suitable for oxygen adsorption which contributes to a higher ORR activity of MoN than Mo_2N based on density functional theory calculations.[131]

Linear sweep voltammograms of these nitrides are shown in Figure 3.1. In both Ar and O_2 atmosphere, reduction peaks around 0.45 V and 0.56 V are observed, especially for Mo_2N and Mo_5N_6. These reduction peaks reflect the reduction of Mo ions upon cathodic polarization, which are not related to oxygen reduction. Cyclic voltammogram of Mo_5N_6 tested in Ar (Fig. 3.1d) clearly shows oxidation and reduction of Mo species. Because the valence states of Mo in the nitrides do not reach the highest state (6+), the surface Mo ions will change dependent on the electrode potential and pH. According to potential-pH equilibrium diagram for molybdenum-water system,[135] Mo ions tend to be oxidized to Mo^{6+} upon anodic sweep and then tend to be reduced to Mo^{3+} upon cathodic sweep in acidic condition. There is no obvious oxidation-reduction peak for δ-MoN, indicating Mo on δ-MoN surface may possess a higher oxidation state.

In acid electrolyte, cubic Mo_2N exhibits the lowest onset potential and current density which indicates that Mo_2N with a rock-salt structure is not an active catalyst for ORR catalysis (Fig. 3.1e and Fig. 3.2a). The maximum current density of Mo_2N is only 4 mA/cm^2 that indicates ORR catalyzed by Mo_2N is not a complete $4e^-$ process. In addition, the ORR current of Mo_2N does not reach the diffusion limit, suggesting the kinetic control appears to be a dominant portion for the reaction. In contrast, nitrides with hexagonal structure exhibit enhanced activity. The diffusion current density for δ-MoN and Mo_5N_6 reaches 6 mA/cm^2 respectively, which corresponds to a nearly $4e^-$ oxygen reduction process. The reaction on these two nitrides seems to be under a combined kinetic-diffusion control of charge transfer and mass transport. Mo_5N_6 and δ-MoN exhibit similar onset potential, though δ-MoN shows a faster kinetic at small overpotential range. This difference is probably related to crystallinity, morphology and surface oxidation state of Mo. Besides onset potential, Tafel slope can be used to evaluate the catalyst.

As can be seen in Fig. 3.2b, Mo_2N has a large Tafel slope while Mo_5N_6 and δ-MoN have relatively smaller Tafel slopes, suggesting oxygen molecules can be reduced more easily on hexagonal molybdenum nitrides. However, the large values of Tafel slopes indicate further modifications on molybdenum nitrides are required to improve the ORR activity.

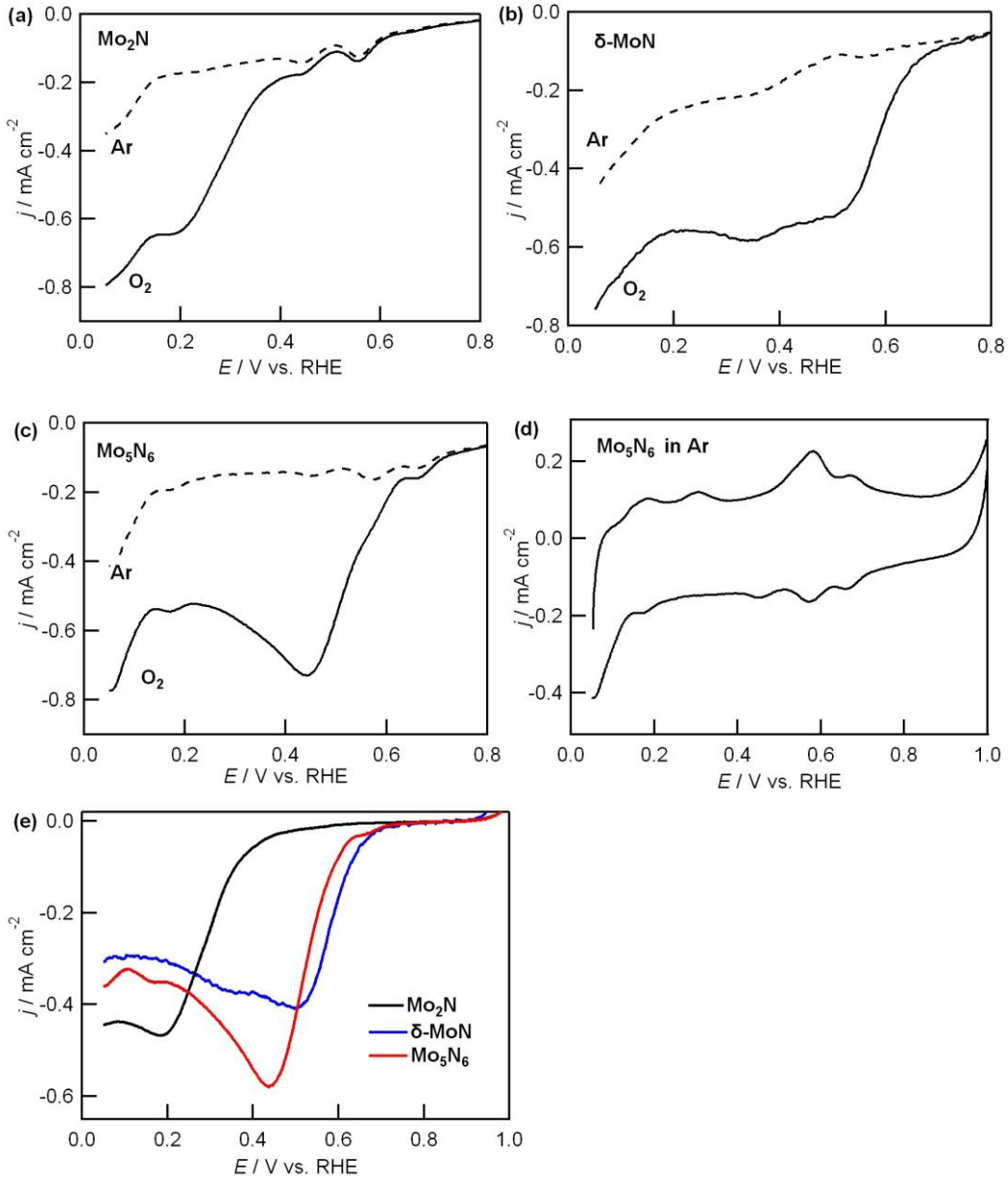

Figure 3.1 Linear sweep voltammograms in Ar (dashed line) and O_2 (solid line) saturated 0.1 M $HClO_4$ for (a) Mo_2N, (b) δ-MoN and (c) Mo_5N_6. (d) CV curve of Mo_5N_6 in Ar atmosphere. (e) Corresponding ORR polarization curves (j_{O2}- j_{Ar}, no rotation) for Mo_2N, δ-MoN and Mo_5N_6.

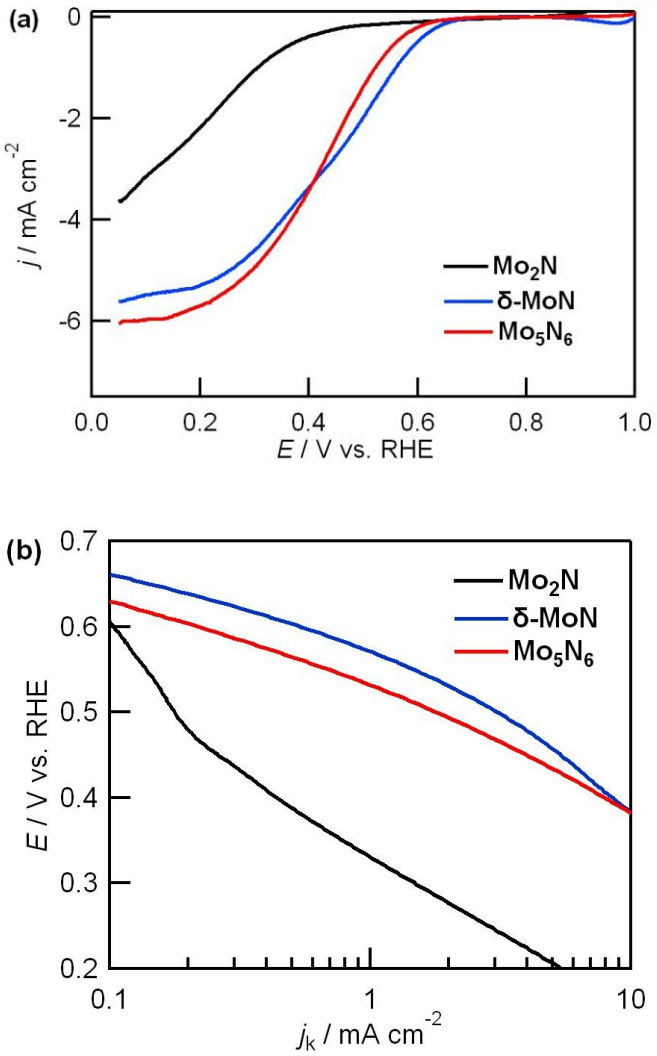

Figure 3.2 (a) RDE curves (1600 rpm) of Mo_2N, δ-MoN and Mo_5N_6 in O_2-saturated 0.1 M $HClO_4$. (b) Corresponding Tafel plots of Mo_2N, δ-MoN and Mo_5N_6.

Table 3.2 ORR activities and Tafel slopes of Mo_2N, δ-MoN and Mo_5N_6 in 0.1 M $HClO_4$.

	Mo_2N	δ-MoN	Mo_5N_6
E_{onset} (V vs. RHE)[a]	0.472	0.680	0.675
$j_{0.6V}$ (mA/cm^2)[b]	0.101	0.500	0.215
Tafel Slope (mV/dec)	190	100	105

[a] E_{onset}, the potential at which the ORR current density | j_{O2}-j_{Ar} | exceeds 25 μA/cm^2. [b] $j_{0.6V}$,the ORR current density at E = 0.60 V vs. RHE.

3.3.2 Crystal Structures

Structure studies are needed to resolve the bulk coordination environment and oxidation state of the cations in the monometallic nitrides, as these two parameters can strongly impact catalytic activity. Two stable types of molybdenum nitrides those based on face centered cubic Mo_2N or on hexagonal nitrides including different polytypes of δ-MoN and Mo_5N_6 can be obtained by ammonolysis of different precursors. Oxide precursors (MoO_3 or $(NH_4)_6Mo_7O_{24}{\cdot}4H_2O$) have been used to prepare Mo_2N.[136] $MoCl_5$ has been used to synthesize nearly pure δ-MoN, while MoS_2 has been used to produce Mo_5N_6.[132] Two primary coordination environments of Mo atoms are found in these crystal structures. In cubic Mo_2N, Mo has an octahedral coordination, though certain site is actually not occupied by nitrogen atoms. Hexagonal molybdenum nitrides contain various Mo coordination environments. δ_1-MoN has a MoN_6 trigonal prismatic unit while δ_3-MoN has an octahedral coordination of Mo atoms. Both octahedral and trigonal polyhedral layers are present in hexagonal Mo_5N_6. Additionally, anion vacancies are present in nominal "Mo_2N" and cation vacancies are present in Mo_5N_6.[132,137]

The ammonolysis of Mo-containing precursors only produces nitrides. No evidence of metallic molybdenum, molybdenum carbides and molybdenum oxides is found in X-ray diffraction patterns. A comparison of their laboratory XRD patterns is provided in Figure 3.3, though a more detailed structural analysis was carried out for each phase using synchrotron and neutron diffraction data. It is distinguishable that Mo_2N belongs to a different structure class compared to δ-MoN and Mo_5N_6. Mo_2N is unique in having a cubic lattice. The remainders of the compounds have atom positons that are related to the simplest hexagonal lattice subcell, as seen in the strong diffraction peaks at the positions predicted by the subcell. In both X-ray and neutron diffraction data, significant peak broadening is present for all three molybdenum nitrides. Peak

broadening is attributed to both size and strain broadening induced from low temperature ammonolysis. In addition, anisotropic peak broadening for hexagonal nitrides are observed which can be ascribed to composition difference among each crystallite.[143] The calculated crystallite size for Mo_2N and δ-MoN was 28 nm and 34 nm respectively based on Le Bail refinement results. Mo_5N_6 exhibits a narrower peak width and a higher order of crystallinity due to relatively higher synthesis temperature and longer annealing time. The calculated crystallite size of Mo_5N_6 is around 68 nm.

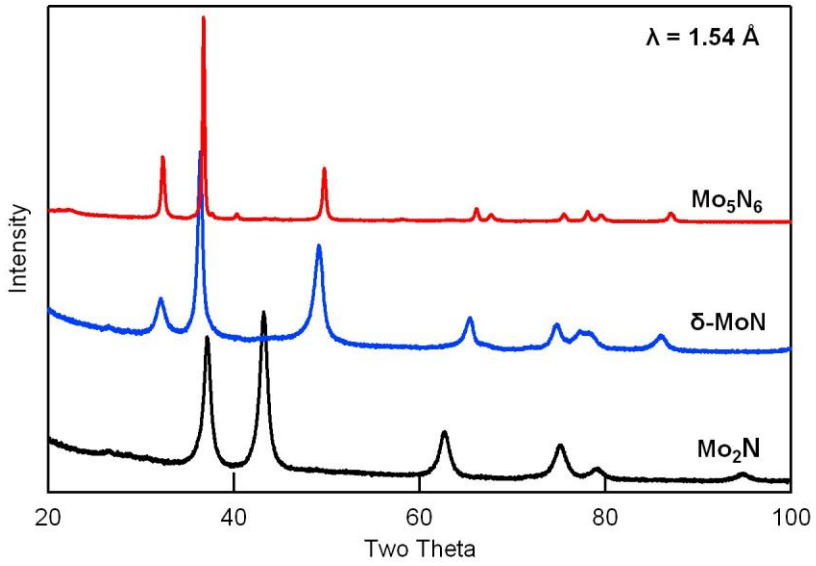

Figure 3.3 Laboratory X-ray diffraction data for Mo_2N, δ-MoN and Mo_5N_6, showing that Mo_2N belongs to a different crystal structure system compared to δ-MoN and Mo_5N_6.

Table 3.3 Lattice parameters for Mo_2N, δ-MoN and Mo_5N_6 based on Le Bail refinements of synchrotron X-ray data (11-BM, λ = 0.4138 Å) .

	Mo_2N	δ-MoN	Mo_5N_6	
Space group	*Fm*-3*m*(225)	*P*6$_3$/*mmc*(194)	*P*6$_3$/*m*(176)	*P*6$_3$/*mmc*(194)
a (Å)	4.19841 (6)	2.8471(7)	4.89669(5)	2.82716(2)
c (Å)		11.147(3)	11.0742(2)	11.0749(1)
V (Å^3)	74.003(4)	78.25(4)	229.957(6)	76.661(2)

Among these compounds, rock salt type Mo_2N has the simplest lattice, and it can be indexed with a small fcc cubic unit cell with a = 4.19841 Å (Table 3.3). The small cell parameters result in only a handful of diffraction peaks being observed in laboratory XRD data. In order to have a sufficient number of peaks to allow the accurate determination of crystallographic parameters from Rietveld refinement, the structural analysis was carried out either using TOF neutron diffraction data or high energy synchrotron data (Fig. 3.4 and Table 3.4). When the Mo occupancy was freely refined using the neutron diffraction data, a stoichiometry of $MoN_{0.534}$ was obtained. This is very close to the ideal stoichiometry of Mo_2N that has been previously proposed.

Despite the consistency of the refined and expected stoichiometry, there are other indications that ideal stoichiometry of Mo_2N may be an imperfect description for this compound. Although X-ray diffraction is less sensitive to the nitrogen content, the refinements of both 11-BM data ($MoN_{0.793}$) and X7B data ($MoN_{0.67}$) suggest that the anion content is deviated away from the ideal stoichiometry. All three powder diffraction refinements were carried out on data collected from different sample preparations, so it is possible that the stoichiometry of this phase is sensitive to the details of the preparation conditions. The difference in the refined stoichiometries could potentially be attributed to the anion site containing a mixture of oxygen and nitrogen, which could result in the neutron refinement underestimating the anion site occupancy when the site is refined as only containing nitrogen. Previous studies demonstrated that ammonolysis of MoO_3 produced molybdenum oxynitride (MoO_xN_y).[138] The oxygen content in the bulk structure was detected via elemental chemical analysis. Our initial efforts to use electron microscopy techniques were inconclusive in identifying the incorporation of oxygen into the crystal structure.

Additionally, the background of the neutron diffraction data exhibits a shape characteristic for incoherent scattering, which is interpreted as originating from hydrogen in this sample. Ammonolysis reactions can incorporate hydrogen in a ceramic lattice in the form of either NH_4^+ cations or as complex anions (OH^-, NH^{2-}, *etc*.). NH_4^+ typically occupies sites suitable for large cations such as Na^+ or K^+, and there are no large sites of this type in rock salt type Mo_2N. An examination of the Fourier diffrenece map of the neutron diffraction data showed no discrete peaks in the difference map that might be linked to hydrogen. While the present preliminary studies clearly idenfity the potential crystallographic complexities associated with Mo_2N, more thorough studies are required to achieve a comprehensive understanding of this phase.

Table 3.4 Refined atomic positions for Mo_2N based on neutron Rietveld refinement.

	Wycoff	*x*, *y*, z	Occupancy	B_{eq} (Å^2)
Mo	4*a*	0, 0, 0	1.0	0.93(4)
N	4*b*	½, ½, ½	0.534(4)	1.34(6)

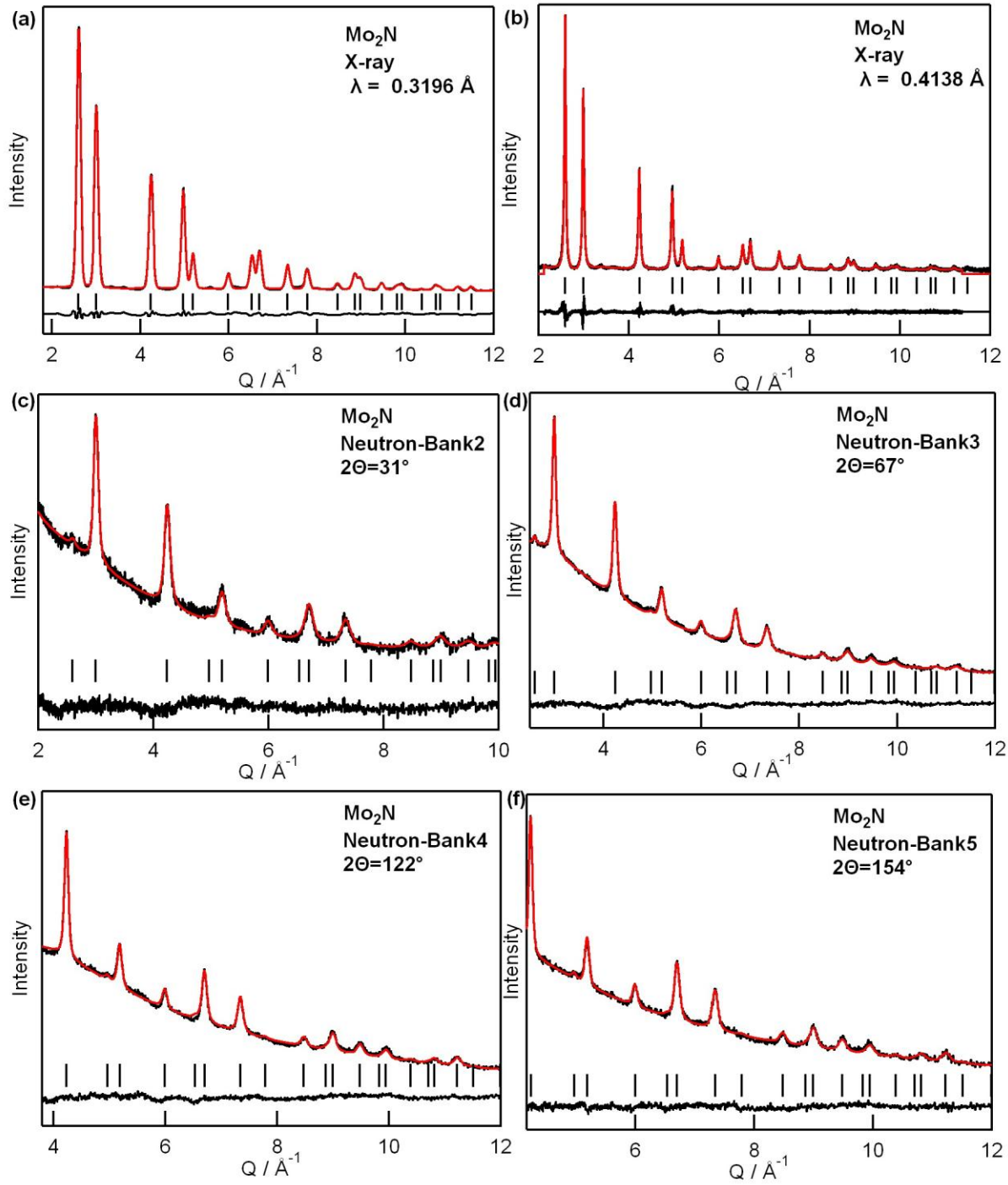

Figure 3.4 Rietveld refinement profiles for Mo_2N using X-ray and time of flight neutron data. Synchrotron X-ray data: (a) λ = 0.3196 Å; (b) λ = 0.4138 Å. Neutron data are ordered by increasing scattering angles: (c) bank 2-2θ=31°; (d) bank 3-2θ=67°; (e) bank 4-2θ=122°; (f) bank 5-2θ=154°. The black line indicates the observed data, the red line indicates the calculated data and the lower black line indicates the difference curve.

Two other nitrides belong to hexagonal structure class. Previous paper reported that diverse polytypes of δ-MoN can be generated and present due to various synthesis conditions.[132] These polytypes can be indexed with either WC-type (δ_1-MoN) or NiAs-type (δ_3-MoN) structure. The two structure types only differ in the arrangement of nitrogen atoms (or Mo coordination environment). The difference in the stacking sequence of nitrogen only results in weak intensities of superstructure peaks in X-ray diffraction which can not be easily resolved since X-ray is insensitive to light atoms. Hence, neutron technique has been applied to determine the position of nitrogen atoms because nitrogen has a strong coherent scattering length of 9.36 fm and it is distinct from Mo atom which has a scattering length of 6.715 fm.

Previous investigations claimed that δ_1-MoN synthesized by $MoCl_5$ was described by WC-type structure (space group *P*-6*m*2, a = 2.851 Å, c = 2.782 Å and Z = 1).[139] δ_3-MoN prepared by high-pressure and high-temperature annealing of δ_1-MoN was proposed to form a 2×2×1 supercell of the NiAs structure type (space group $P6_3mc$, a = 5.737 Å, c = 5.613 Å and Z = 8).[140,141] Disorder of nitrogen atoms in δ_1-MoN along *c*-axis was observed which made its crystal structure complicated.[132] Although X-ray diffraction data for δ-MoN can be fitted with one layered structure model, the neutron diffraction pattern clearly demonstrates that δ-MoN does not have a simple WC-type structure in this study due to the presence of superstructure peaks at d = 1.64 Å and d = 2.06 Å (Fig. 3.5). The plausible model of δ phase can be described as a layer structure with a complex sequence of nitrogen layers containing both WC- and NiAs-type building blocks. Some pairs of adjacent layers have the same stacking sequence (*ie* AA) while other pairs have opposite stacking sequence (*ie* AB). Ganin *et al.* have proposed that a random stacking of nitrogen atoms is present in δ_1-MoN which can not be easily modeled.[132] In this study, the neutron diffraction data could be most effectively modeled using the space group

$P6_3/mmc$. δ-MoN is indexed with a unit cell of a = 2.8471 Å and c = 11.147 Å which can be expressed as a 1×1×4 supercell compared to WC-type unit cell (Fig.3.6). This supercell is generated by an alternative stacking sequence of MoN_6 trigonal prism and octahedra. Although most peaks of δ-MoN can be well fitted by the four layered structure model, peak at d = 2.26 Å can not be fitted indicating that δ-MoN may contain other nitride phase with a different space group and unit cell. The broadened peak width makes it difficult to index the minor phase. The minor phase probably has similar formation energy with major phase under ambient synthesis condition. Other synthesis route such as high pressure synthesis or thin film deposition will be applied to approach single-phase sample.

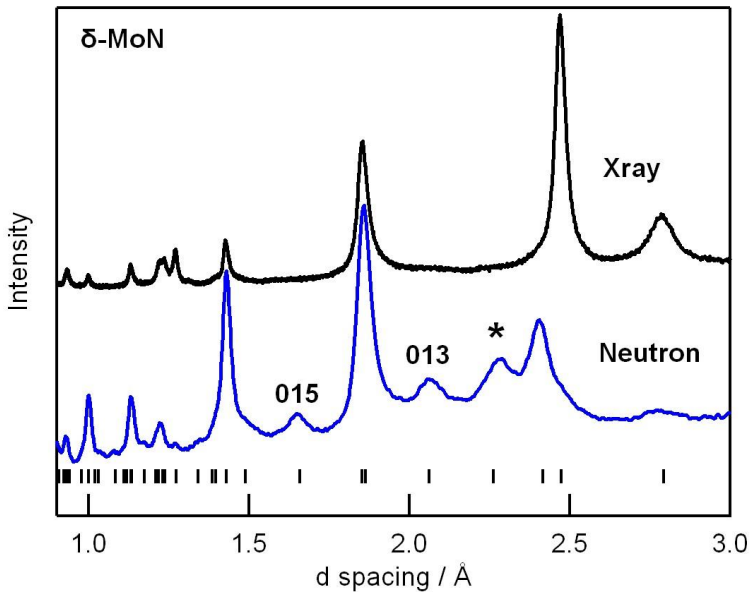

Figure 3.5 Comparison of X-ray and neutron powder diffraction patterns of δ-MoN in the same d spacing range of 1 to 3 Å. Super structure peaks such as 013 and 015 reflections are more intense in neutron diffraction data.

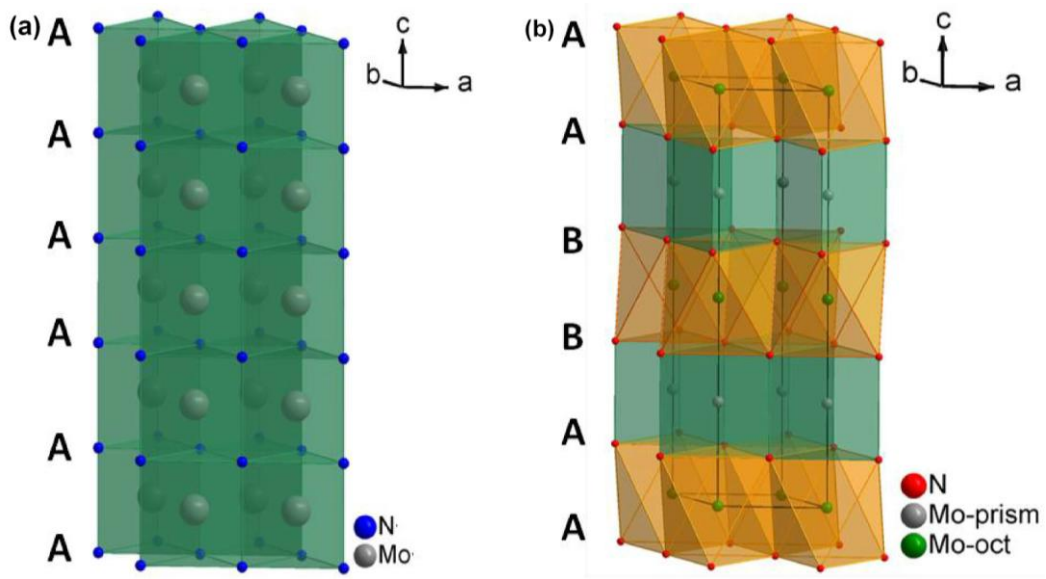

Figure 3.6 (a) Single layered crystal structure of δ-MoN only containing trigonal prisms (space group No. 187). (b) Four layered crystal structure of δ-MoN containing alternative trigonal prisms and octahedra (space group No. 194).

Hexagonal Mo_5N_6 was first prepared by a reaction of thin Mo films with ammonia and indexed with space group $P6_3/mmc$ (a = 2.86 Å, c = 11.20 Å and Z = 4).[142] Later, this nitride is characterized with a larger unit cell ($\sqrt{3}\times\sqrt{3}\times4$, space group $P6_3/m$, a = 4.893 Å and c = 11.20 Å). [132,133] Mo_5N_6 can be viewed as an intergrowth of WC- and NiAs-type structure which presents a featuring AABBAA stacking arrangement. The intergrowth of different polytypes was observed in high resolution TEM images.[132] The literature structure was refined with five independent Mo sites in the proposed space group of $P6_3/m$ (No. 176), which hints that a non-optimal space group may have been chosen in the analysis of the laboratory data used in this initial structure determination. Our laboratory X-ray data shows clear evidence of the c-axis superstructure (including a strong and sharp 002 peak at d = 5.53 Å). However, there are only two or three broad peaks associated with the in-plane $\sqrt{3}\times\sqrt{3}$ superstructure suggesting that the in-plane coherence of the superstructure may be limited. The sensitivity of XRD methods to the

supercell suggests that Mo cations are involved in the superstructure formation, as may also be inferred by the composition of this phase.

The crystal structure is initially refined using 1×1×4 superstructural model based on synchrotron and neutron diffraction data, ignoring the weak in-plane supercell reflections (Fig. 3.7). The Rietveld refinement of neutron diffraction data using this structural model was quite successful in modeling the observed diffraction peak intensities, and the resulting structural model had both reasonable bond distances and displacement parameters (Table 3.5). The occupancies of the trigonal prismatic (1.0) and octahedral (0.70) Mo sites could be clearly seen to be different though the Mo vacancy was found on the octahedral site and not the prismatic site, in contrast to the previously proposed structure. Since knowledge of the nitrogen positions is required to differencitate between prismatic and octahedral site, the octahedral location of the Mo vacancy determined from the neutron data should be considered to be definitive.

Table 3.5 Refined atomic positions for Mo_5N_6 based on neutron Rietveld refinement.

	Wycoff	*x*, *y*, z	Occupancy	U_{ij} or U_{iso}(Å^2)
Mo_{prism}	2*a*	0, 0, 1/4	1.0	U_{iso} = 0.0048(2)
Mo_{oct}	2*b*	0, 0, 0	0.70(1)	U_{iso} = 0.0048(2)
N	4*f*	1/3,2/3, 0.1302(1)	1.0	U_{11}= U_{22}=0.0035(8) U_{33} = 0.0147(4) U_{12} = 0.00175 U_{13}= U_{23}=0

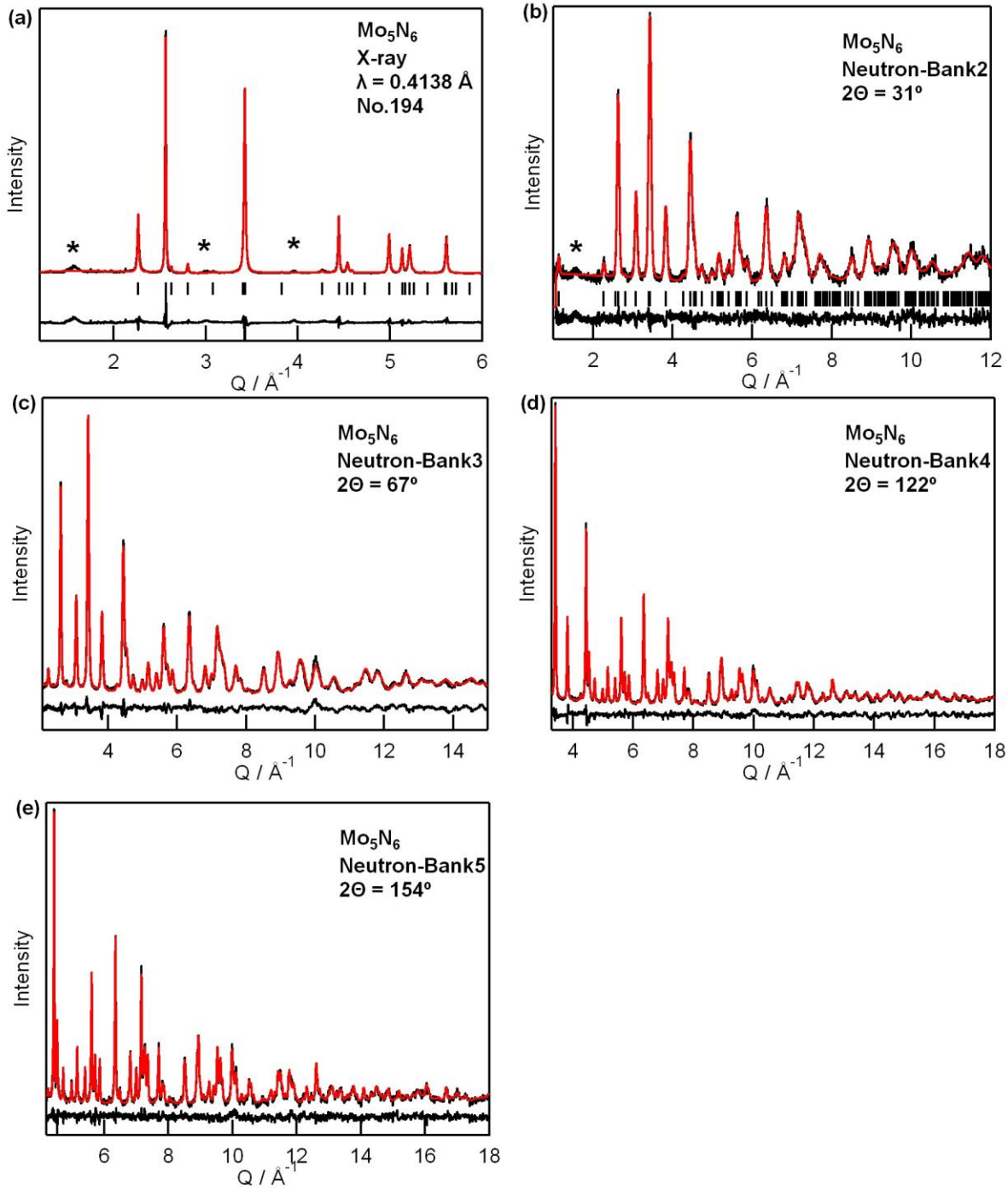

Figure 3.7 Rietveld refinement profiles for Mo_5N_6 using space group No. 194. (a) Synchrotron X-ray data (λ = 0.4138 Å). Neutron data are ordered by increasing scattering angles: (b) bank 2-2θ=31°; (c) bank 3-2θ=67°; (d) bank 4-2θ=122°; (e) bank 5-2θ=154°. The black line indicates the observed data, the red line indicates the calculated data and the lower black line indicates the difference curve.

Efforts to explicitly model the Mo_5N_6 structure using the full $\sqrt{3}\times\sqrt{3}\times4$ superstructure were also carried out. It is difficult to carry out space group determination using powder diffraction data. A search for higher symmetry based on the previsouly proposed Mo_5N_6 structure indicated space group $P6_3/mcm$ (No. 193) as a plausible alternative. In this space group, a smaller number of Wykoff sites completely describe the atom positions, with N at the 12*k* site and Mo at 2*a* (prismatic), 4*c* (prismatic) and 4*d* (octahedra) site. However, the Rietveld refinement results based on this space group gave larger R_{wp} values. This model should not be considered to be absolutely correct. This is apparent both in transimission electron microscopy studies,[132] which found abundant stacking faults and in the synchrotron data of the present study, which exhibits a number of additional weak peaks at high *d* spacings suggesting the presence of more complex or multiple superstructures (Fig. 3.8). These fine details of the structure are expected to be sensitive to non-stoichiometry relative to the ideal Mo_5N_6. Further studies investigating the relationship between synthesis condition and crystal structure are still merited.

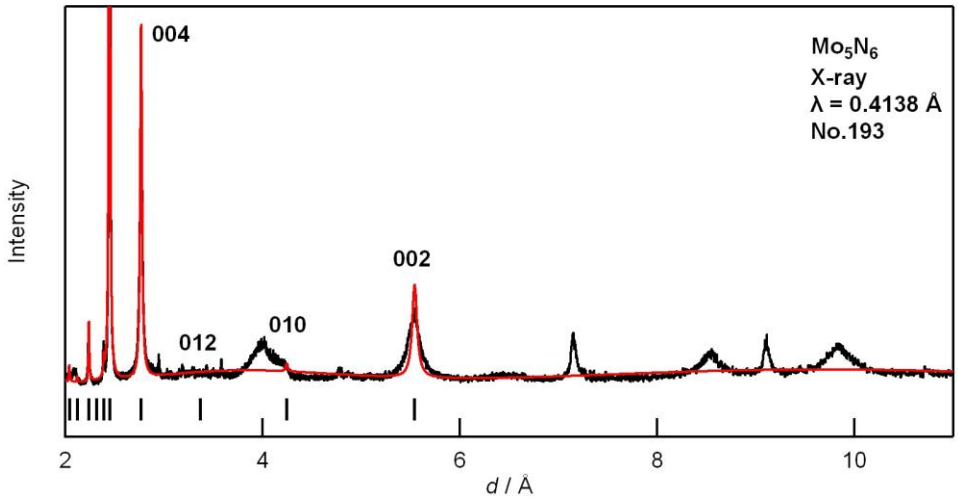

Figure 3.8 Lebail refinement profile of Mo_5N_6 based on structure model No. 193 using synchrotron X-ray data.

Given the complexities observed in the analysis of the bulk structures, the local structure and bond length are investigated according to neutron PDF measurements. The local structures of these nitrides are consistent with their average bulk structures. The first peak in neutron PDF pattern is attributed to molybdenum-nitrogen bond (Fig. 3.9 and Table 3.6). It can be clearly seen that the PDF peaks are substantially broader in Mo_2N than in the other two binary nitrides. This is consistent with the relatively large displacement parameters seen for both the Mo and the N sites. This wide distribution is attributed to the inhomogenous local environments, as on average only three of the six nitrogen sites around each Mo cation are occupied, and this occurs in a disordered manner judging from the very simple average structure observed for this compound. Mo-N bond length in Mo_2N is 2.095 Å, shorter than that in other binary nitrides despite the larger ionic radius expected for the low valence Mo (+1.5) ions in this nitride. This is a consequence of the reduced coordination number of Mo, which is well-known to cause significant reduction in bond lengths for a given cation valence.

As mentioned above, there are two types of Mo coordination environments in hexagonal nitrides. In δ-MoN, Mo_{oct}-N is 2.183 Å while Mo_{prism}-N is 2.151 Å. The shorter bond length leads to a higher oxidation state. Therefore, Mo located at octahedral site has a lower oxidation state. Insights into Mo valence states can be obtained by comparing Mo-N bond lengths to those in reference nitrides. In Mo_5N_6, the bond length of Mo_{oct}-N (2.177 Å) is similar to that of reported Mo^{3+}-N. Hence, Mo on octahedral site can be assigned a valence of 3+. The smaller Mo_{prism}-N bond distance (2.103 Å) is comparable to the bond length in $MnMoN_2$ (2.12 Å), indicating Mo on trigonal prismatic site has a valence state near 4+ or higher than 4+.[144] Mo-N bond lengths of δ-MoN on both sites are longer than those of Mo_5N_6, meaning δ-MoN has a lower oxidation state than Mo_5N_6 which is consistent with the stoichiometry.

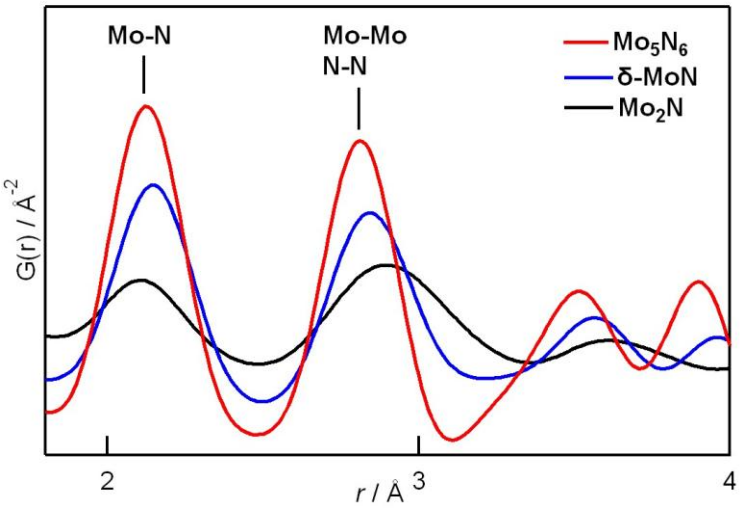

Figure 3.9 Overlay of neutron PDF patterns of Mo_2N, Mo_5N_6, δ-MoN in the range of 1.7 to 4 Å. Peaks within the PDF can be assigned to various atom-atom correlations.

Table 3.6 Summary of bond length for Mo_2N, Mo_5N_6, δ-MoN obtained through neutron PDF refinement results.

	Distance (Å)		
Compounds	Mo_2N	δ-MoN	Mo_5N_6
Mo_{oct}-N	2.095(1)×6	2.183(4)×6	2.177(3)×6
Mo_{prism}-N		2.151(3)×6	2.103(2)×6

These molybdenum nitrides exhibit different stabilities upon air exposure. Bulk Mo_2N and Mo_5N_6 are stable against air and moisture. MoN will be partially oxidized in ambient moisture environment. These nitrides can be fully oxidized to MoO_3 by heating them in oxygen at 500 °C. TGA experiments were performed to estimate the stoichiometry of these nitrides (Fig. 3.10). A weight loss at 150 °C was observed for all three molybdenum nitrides that indicated water was adsorbed on the nitride surface. For Mo_2N, the final weight gain of 27.92% is much lower than theoretical value of 39.83% which indicates Mo_2N contains residual oxygen owing to the incompletion nitridation of oxide precursor. The calculated stoichiometry for Mo_2N is

therefore $Mo_2(NO)_{1.2}$. The weight gain for MoN (21.94%) is lower than the calculated value (30.92%). Because δ-MoN contains impurity phase and it might be oxidized somehow when it is exposed to air, the accurate composition of MoN can not be well determined. For Mo_5N_6, the weight gain is 23.42 % which is slight smaller than theoretical weight gain (27.67%). The corresponding stoichiometry is Mo_4N_6. The fact that experimental mass gains are smaller than expected values is possibly caused by the partial evaporation of MoO_3 at high temperature. A more accurate elemental analysis of light atoms can be approached via combustion method.

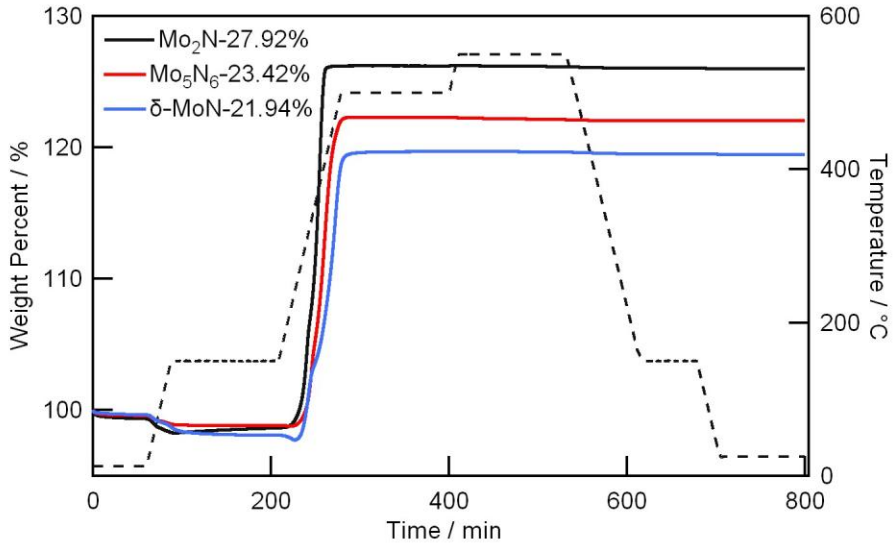

Figure 3.10 TGA analysis of Mo_2N, Mo_5N_6 and δ-MoN under flowing O_2 from room temperature to 550 °C.

3.3.3 Morphology

Molybdenum nitrides prepared via different precursors exhibit various morphologies shown in Fig.3.11. Morphology has an important impact on the catalytic activity for ORR. It can be seen that Mo_2N exhibits a size distribution of 0.2 μm to 1 μm (Fig.3.11a). Mo_5N_6 has a featuring lamellar structure where the retention of the morphology on nitridation of layered MoS_2 was observed (Fig.3.11b). Multiple morphologies, such as plate and toroid shape crystals,

exist in δ-MoN which indicates this nitride might contain several phases and domains (Fig.3.11c). In addition, SEM is useful to evaluate the homogeneity of samples on a large scale. Mo_2N and Mo_5N_6 are more homogeneous than δ-MoN.

TEM analysis was performed to study their morphologies on a smaller scale compare to SEM analysis. TEM images indicate that these nitrides form agglomerates with a size distribution from 10 nm to 150 nm (Fig.3.12). The tendency of high aggregation is due to the strong interactions between particles which have metallic properties.[145] Moreover, Mo_2N was observed to have a porous property. The length of the flake for Mo_5N_6 is about 150 nm and the thickness of the flake is about 30 nm.

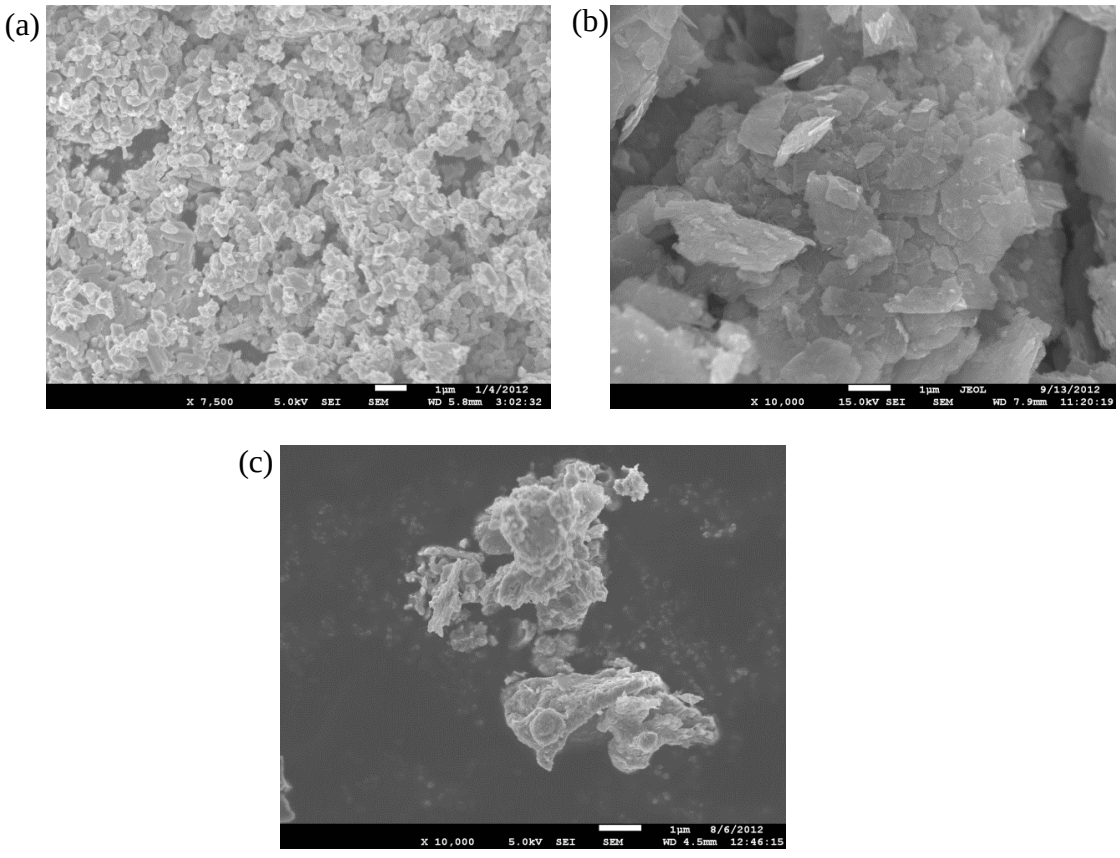

Figure 3.11 SEM images of (a) Mo_2N, (b) Mo_5N_6, (c) δ-MoN (scale bar: 1 μm).

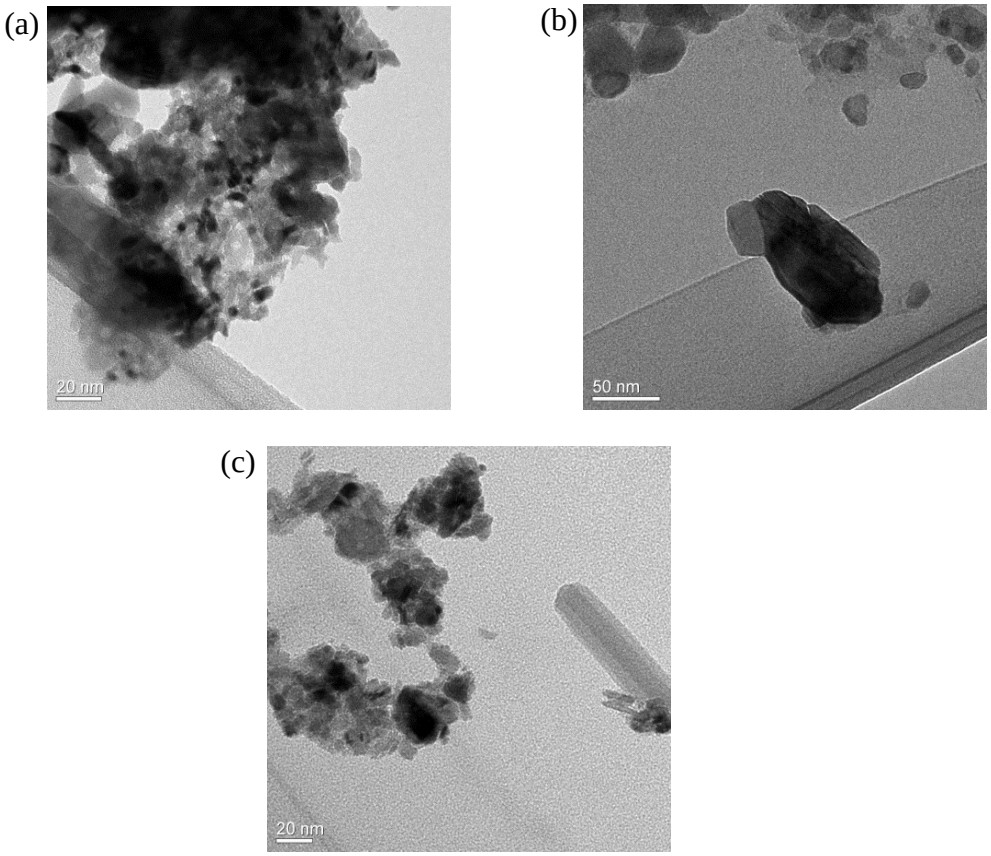

Figure 3.12 TEM images of (a) Mo_2N (scale bar-20 nm), (b) Mo_5N_6 (scale bar-50 nm), (c) δ-MoN (scale bar-20 nm).

3.3.4 Magnetic Property

Molybdenum nitrides have shown superconductivity under zero-field-cooled conditions (Fig. 3.13). Mo_2N shows a superconducting transition with a T_c near 4.0 K. This value is lower than previously reported value which is probably influenced by the slightly different stoichiometry.[146-148] The superconducting transition of δ-MoN is around 5.6 K which agrees with the reported value. It is known that the degree of disorder has an impact on the T_c of δ-MoN. The highly disordered phase has a T_c of 4.2 K whereas the ordered phase has a T_c of 12.1 K.[140] The superconducting transition temperature of δ-MoN indicates disorder to some extent is present in this nitride which is also supported by refinement results.

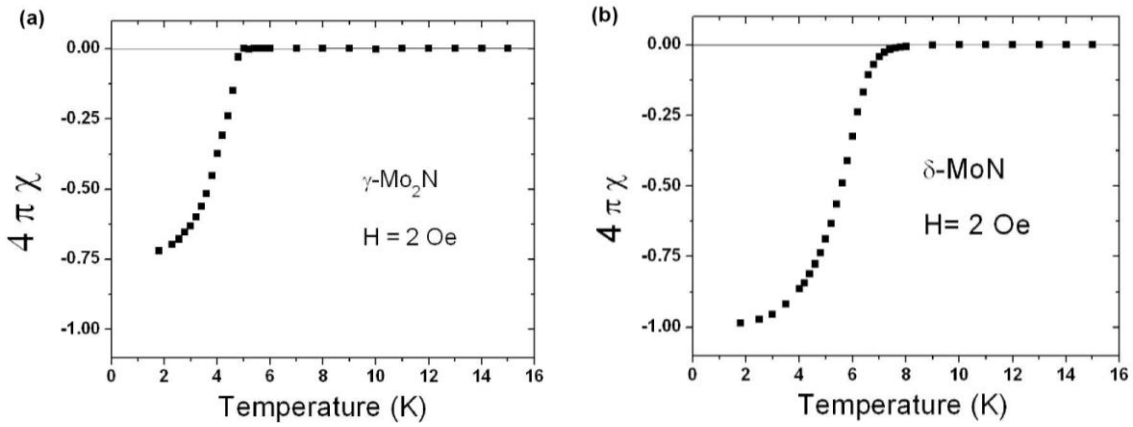

Figure 3.13 Temperature dependence of magnetic susceptibilities for (a) Mo_2N and (b) δ-MoN.

3.3.5 Density of States Calculations

Lattice parameters in Table 3.3 are used to calculate the electronic band structures of Mo_2N and δ-MoN through the plane-wave-based density functional method. The total (TDOS) and local density of states (LDOS) for molybdenum nitrides are plotted in Fig. 3.14 to understand the changes in the electronic structures. There are three energy regions in LDOS: (i) the lowest energy region is mainly from N 2s states. (ii) the lower region of valence band originates from Mo 5s and N 2p states and the upper region of valence band consists of Mo 4d and N 2p states. (iii) the conduction band above the Fermi level contains unoccupied Mo 4d states. It is clearly that N 2p orbitals hybridize strongly with Mo 4d orbitals. The electronic structure of molybdenum nitrides may originate from the interaction between N 2p electrons and Mo 4d electrons.[149,150] This hybridization influences the bonding properties and material properties to some degree (eg. superconductivity). Total energies of molybdenum nitrides have been calculated by Jaouen *et al.*[149] It is evidenced that cubic phases have a higher total energy than hexagonal phases. Thus, it can be concluded that hexagonal nitrides are more stable. From TDOS of δ-MoN with two different nitrogen stacking sequences, the density of state near Fermi

level (E_F) increases for δ-MoN (187), whereas the density of state lies in a lip for δ-MoN (194). The latter structure is more stable than the former structure. Total energy calculation demonstrates that δ_3 phase is more stable than δ_1 phase.[149] δ_3-MoN contains octahedral ordering of nitrogen while δ_1-MoN contains trigonal prismatic layers of nitrogen. Since δ-MoN (194) consists of alternating octahedral and trigonal prismatic layers, this type of ordering should have a lower energy than δ_1-MoN (187) which agrees with the DOS calculation.

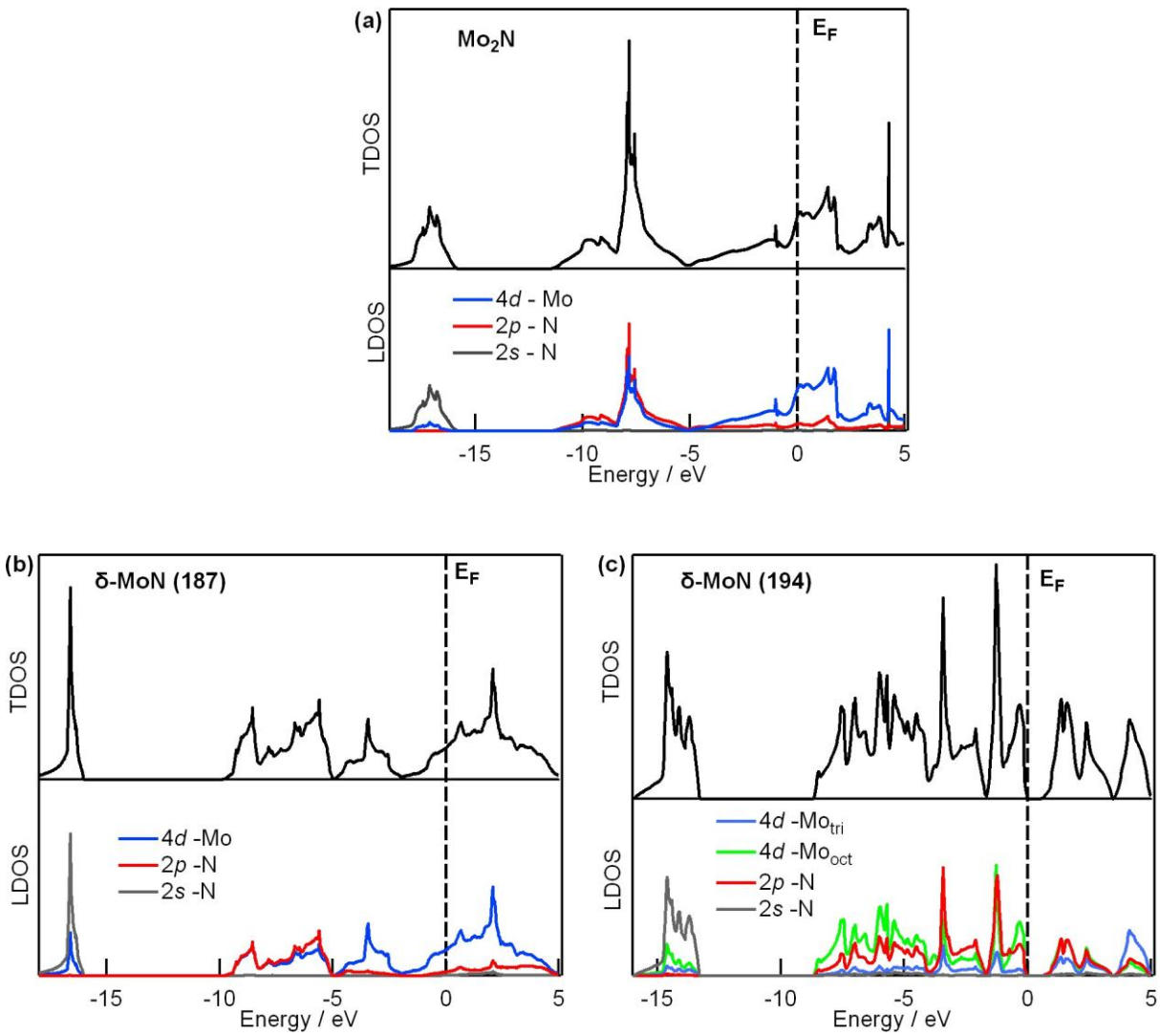

Figure 3.14 Total DOS (top) and local DOS (bottom) for (a) Mo_2N, (b) δ-MoN (space group 187) and (c) δ-MoN (space group 194).

3.4 Conclusions

In summary, binary molybdenum nitrides with different crystal structures have been investigated as ORR catalysts for PEMFC. Structural factor plays an important role on the catalytic property. Molybdenum nitrides were synthesized by ammonolysis of various precursors at different temperatures (600-750°C). Face centered cubic Mo_2N synthesized via MoO_3 showed poor ORR activity (E_{onset} = 0.420 V) in acid electrolyte while hexagonal δ-MoN (prepared via $MoCl_5$) and Mo_5N_6 (prepared via MoS_2) exhibited enhanced catalytic performance (E_{onset} = 0.680 and 0.675 V). DOS calculations indicate that the hybridization of N 2p electrons and Mo 4d electrons lead to the electronic structures of molybdenum nitrides. Cubic Mo_2N has a higher total energy than hexagonal phases. Hence, the hexagonal molybdenum nitrides are more stable and more suitable for ORR catalysis.

In both δ-MoN and Mo_5N_6, Mo atoms are located in the center of octahedral or trigonal prismatic layers. Disorder of nitrogen layers is observed in δ-MoN while Mo_5N_6 consists of alternative stacking MoN_6 layers. Mo atom located on octahedral site has a lower oxidation state than that located on trigonal prismatic site based on bond distance analysis derived from neutron PDF data. Modifying synthesis method to prepare homogeneous powder or thin film molybdenum nitrides with a hexagonal unit cell will improve its electrochemical activity and will help understand factors influencing the activity better.

Chapter 4. Ternary Cobalt Molybdenum Nitride Electrocatalyst for Oxygen Reduction Reaction and Hydrogen Evolution Reaction

4.1 Introduction

The hydrogen evolution reaction (HER) is a central reaction in the renewable production of hydrogen fuel from water, regardless of whether this process is driven directly (solar fuels production using photons harvested by semiconductors or molecular dyes) or indirectly (electrolysis of water powered by photovoltaics).[151,152] Hydrogen produced in this manner is more easily stored and transported than electricity generated through competing photovoltaic (PV) technologies, though the overall efficiency of hydrogen production is invariably lower than that of the simply generating electricity due to the energy barriers of the reactions required to produce molecular products.[153] Efficient solar energy utilization therefore requires efficient catalysts. Unfortunately, the best current HER catalysts incorporate noble metals such as Pt, whose terrestrial scarcity and high cost limit the viability of renewable H_2 production.[154]

The high cost of noble metals limits their utilization in practical electrolyzer and drives the demands to search low-cost materials as alternatives. Unlike the known classes of Ni-based HER catalysts which are only stable under alkali conditions,[93] Notable recent progress has been made in the last decade in developing acid-stable HER catalysts, resulting in the discovery of excellent HER activity for MoS_2, Mo_2C, MoB, Ni-Mo, Ni-Mo-N, and Ni_2P, which all contain Mo and/or Ni.[83,93,97,99,103-106] A good framework for understanding the influence of crystal structure on the HER activity of these compounds does not yet exist. Although methods for tuning the energy levels and catalytic activity of metallic alloys are known,[89] it is less clear how the simple binary structures of MoS_2, Mo_2C, and MoB can be tuned to optimize their activity. The bimetallic Ni-Mo-N catalyst may be more amenable to optimization, though catalytically active

samples were found to contain a mixture of an ionic rock salt phase (γ-Mo_2N-type) and a Ni_2Mo_3N (Mo_3Al_2C-type) phase in which Mo is expected to be metallic in nature (valence near zero) and it is not yet established which phase is responsible for the observed HER activity.[105]

We were therefore motivated to investigate the electrocatalytic activity of more complex ternary molybdenum nitrides in which the valence and electronic states of Mo can be more readily tuned than in binary molybdenum nitrides. We hypothesized that doping MoN with Co would be an effective method of tuning its properties and potentially enhancing the catalytic activity beyond the relatively low intrinsic activity of MoN. Such a strategy was recently employed to enhance the oxygen reduction reaction (ORR) activity of Mo_2N by the substitution of CoO into its rock salt structure.[107] In this study, the ORR and HER activity of a nanostructured ternary cobalt molybdenum nitride produced using a low temperature synthesis route has been characterized. Neutron diffraction studies indicate that this compound has a complex layered structure that can not be effectively resolved in X-ray diffraction experiments. This compound is demonstrated to have excellent activity toward HER despite belonging to a layered structural family for which HER activity has not previously been reported.

4.2 Experiment Section

4.2.1 Sample Preparation

An oxide precursor $CoMoO_4$ was prepared by dropwise addition of 20 mL (0.165 M) aqueous $CoCl_2$ (Alfa Aesar, 99.7%) into a 10 mL (0.33 M) solution of Na_2MoO_4 (Alfa Aesar). The resulting purple suspension was stirred for 1 hour, filtered, washed, and dried at 120 °C overnight. Co_3Mo_3N was prepared via two different methods in which nitrogen was provided by ammonia in either a gaseous form (flowing NH_3) or a solid form (urea with flowing Ar), and the reaction products are therefore denoted Co_3Mo_3N and Co_3Mo_3N(s), respectively. Co_3Mo_3N was

synthesized by annealing $CoMoO_4$ at 750 °C (5 °C / min heating rate) for 12 hours under flowing ammonia (50 mL / min) inside a fused quartz tube. Co_3Mo_3N(s) was synthesized by annealing $CoMoO_4$ together with urea (molar ratio 1 : 5) at 800 °C for 3 hours under flowing Ar (50 mL / min). The final product $CoMoN_2$ ($CoMoN_2$(s)) was synthesized by annealing Co_3Mo_3N (or Co_3Mo_3N(s)) in NH_3 (150 cm^3 / min) for 1 hour at 400 °C.[155] δ-MoN was produced by treating $MoCl_5$ (Alfa Aesar, 99.6%) at 600 °C in NH_3 (150 cm^3 / min) for 3 hours, and this sample is described in the text as δ-MoN based on the hexagonal unit cell seen in X-ray diffraction experiments. The precise polytype (δ_1, δ_2, δ_3) cannot be resolved in these experiments, though the δ_1 polytype has been reported to form under these conditions.[132]

4.2.2 Physical Characterization

Laboratory X-ray powder diffraction patterns were obtained from a D8 Advance X-ray diffractometer (Bruker, AXS) with a Bragg-Brentano geometry using Cu K_α radiation (1.54056Å). Scans were collected with a fixed divergence slit width of 0.6°, a 2θ range of 7 to 120°, a collection time of 1.5 s per step, a diffraction radius of 300 mm, and a 192 channel LynxEye position sensitive detector. Synchrotron X-ray diffraction data were collected at the high resolution beamline 11-BM at the Advanced Photon Source (APS) of Argonne National Laboratory using a 0.8 mm diameter Kapton capillary with $\lambda = 0.413832$ Å.

Time-of-flight (TOF) neutron diffraction measurements were performed on the nanoscale-ordered materials diffractometer (NOMAD) at the Spallation Neutron Source (SNS), Oak Ridge National Laboratory. About 100 mg of powder were loaded into a 2 mm diameter capillary, with data acquisition time of 100 min per sample for a total proton charge of 5.4×10^{12}. Data processing of both pair distribution function (PDF) and Bragg diffraction data was done

using custom beamline-specific software coded in IDL. The TOPAS software package (Version 4.2, Bruker AXS) was used for Le Bail and Rietveld refinements of data.

Scanning electron microscopy (SEM) analysis was carried out on a JEOL 7600F high resolution microscope with capabilities for energy-dispersive X-ray spectroscopy (EDX). Transmission electron microscopy (TEM) was performed on a JEOL 1400 microscope operated at an accelerating voltage of 120 kV.

Thermogravimetric analysis (TGA) was done on a Q5000IR system (TA instruments). For $CoMoN_2$ samples, TGA scans were run under flowing O_2 (25 mL / min) with ramp rates of 1 °C / min and holds at 500 °C for 10 hours and then at 600 °C for 5 hours.

A PHI 3056 X-ray Photoelectron Spectroscopy (XPS) spectrometer with an Al source in a 2×10^{-10} Torr vacuum chamber was used to characterize sample surfaces. The instrument was calibrated before use with Au and Ag foils. Samples were pressed into In foil (Alfa Aesar), which foil was attached to the sample holder using carbon tape. High resolution scans were taken with a 5.85 eV pass energy, 0.05 eV energy step, and with 100 repeats to reduce instrument noise. Charging effects were compensated by shifting binding energies based on adventitious C 1s peak (284.8 eV). Reference MoO_2 (Alfa Aesar, 99.95%) and MoO_3 (Alfa Aesar - Puratronic) powders were used to determine the Mo $3d_{5/2}$ / Mo $3d_{3/2}$ ratio for the instrument. Peak fits and atomic surface concentration analysis was performed using PHI Multipack software.

4.2.3 Electrochemical Measurements

Catalyst inks for electrochemical testing were prepared by adding a mixture of 2 mg sample (Co, δ-MoN or nominal $CoMoN_2$) and 2 mg carbon black (Vulcan XC72) to a solution of 500 μL Milli-Q ultrapure deionized water (18.2 MΩ), 500 μL isopropyl alcohol (70% v/v, Aldrich), and 50 μL Nafion-117 (5 % in a mixture of lower aliphatic alcohols and water,

Aldrich), and then sonicating for 30 min to disperse the catalysts in the ink. Afterwards, 25 μL of fresh catalyst ink was dropped onto a glassy carbon electrode (0.196 cm^2 geometrical area, Pine Research Instrument) and dried at room temperature. The loading was 0.24 mg/cm^2 for nitride samples and 0.023 mg/cm^2 for Pt. Electrochemical measurements were conducted in a three electrode conventional glass cell with an electrolyte solution of 0.1 M $HClO_4$, an Ag/AgCl reference electrode, and a Pt counter electrode (separated from the electrolyte by a glass frit). All potentials are given with respect to the reversible hydrogen electrode (RHE).

4.2.3.1 Electrochemical Measurements for ORR

Both cyclic voltammetry (CV) and rotating disk electrode (RDE) measurements were performed by sweeping from 0.05 to 1.0 V vs. RHE at a scan rate of 10 mV/s. CVs were recorded in solutions saturated with either Ar or O_2 gas. RDE measurements were collected in O_2-saturated solutions with a rotation speed of 400-2500 rpm. Durability tests were conducted in air saturated 0.1 M $HClO_4$ from 0.05 to 0.8 V vs. RHE at a scan rate of 100 mV/s for 2000 cycles.

4.2.3.2 Electrochemical Measurements for HER

HER measurements on a rotating disk electrode (RDE) were collected in H_2-saturated solutions sweeping from +0.2 to -0.5 V vs. RHE with a scan rate of 5 mV / s and a rotation speed of 1600 rpm using Volta PGZ402 potentiostat (VoltaLab 80, Radiometer Analytical). HER measurements on carbon paper (1 cm^2 geometrical area, Avcarb, purchased from Fuel Cell Store) were carried out in H_2-saturated 1 M $HClO_4$ from +0.05 to -0.5 V vs. RHE at a scan rate of 10 mV / s. Electrochemical impedance measurement was applied to both RDE and carbon paper configurations to determine the resistance. The Ohmic resistance used for *iR*-correction was determined from the high frequency resistance obtained through electrochemical impedance

spectroscopy measurements in the same electrolyte at a dc potential of 0 V vs. RHE with a peak-to-peak perturbation of 20 mV. The measured resistance of $Co_{0.6}Mo_{1.4}N_2$ catalyst on the RDE in 0.1 M $HClO_4$ was about 25 Ω, while its resistance on carbon paper in 1 M $HClO_4$ was about 4 Ω. Long-term durability tests were performed by cyclic voltammetry (CV) sweeps at 100 mV / s from +0.2 to -0.3 V vs. RHE for 3000 cycles.

HER measurements on a RDE in 0.1 M KOH solution were collected in H_2-saturated solutions sweeping from +0.2 to -0.5 V vs. RHE with a scan rate of 5 mV / s and a rotation speed of 1600 rpm using Volta PGZ402 potentiostat (VoltaLab 80, Radiometer Analytical). The measured resistance of $Co_{0.6}Mo_{1.4}N_2$ catalyst on the RDE in 0.1 M $HClO_4$ was about 48 Ω.

Quantification of evolved H_2 gas during HER testing was performed in 0.1 M $HClO_4$ using the same three-electrode cell. The $Co_{0.6}Mo_{1.4}N_2$ catalyst was cast onto carbon paper (1 cm^2 geometric area, catalyst loading ~ 0.24 mg/cm^2). Carbon paper was attached to a Ti rod using Ag epoxy, and then the rod was threaded into a tygon tube in order to isolate it from the electrolyte. This modified working electrode was inserted into an inverted electrolyte-containing vial. A cathodic current of 10 mA was chosen and maintained for 3000 s. The volume of H_2 produced in the vial was marked and measured. $Co_{0.6}Mo_{1.4}N_2$ produced about 3.45 mL H_2, which is 92% of the theoretical H_2 yield of 3.74 mL for 30 coulombs of charge at 1 atm and 20 °C.[106] This yield is not clearly distinguishable (within the limited precision of this method to collect and quantify evolved hydrogen gas) from that expected from the fully Faradaic production of H_2 gas. However, some potential chemical origins of reduced H_2 yields are the production of H_2 on portions of the Ti rod which were not fully protected from electrolyte, the incomplete release of H_2 gas from catalyst particles, and the competing reduction processes associated with the

activation of the $Co_{0.6}Mo_{1.4}N_2$ electrode that are responsible for the slight change in the measured response over the first 50 cycles during in durability testing.

4.3 Results and Discussion

4.3.1 Crystal Structure

The direct ammonolysis of $CoMoO_4$ at temperatures between 600 °C and 650 °C was found to produce a hexagonal nitride of nominal formula $CoMoN_2$, but the reaction product also contained large amounts of impurity phases like cobalt metal, rock salt type Mo_2N analogues, and cubic Co_3Mo_3N. Higher temperature reactions were found to produce phase-pure Co_3Mo_3N with a lattice parameter of a = 11.0383(2) Å that we have tested and found to show weak catalytic activity for ORR and HER reaction. The low fraction of nitrogen in Co_3Mo_3N suggests that Co and Mo are nearly metallic (a result confirmed by prior XPS studies[126]) and that the reaction conditions are too reducing.

Although the direct synthesis of $CoMoN_2$ from a $CoMoO_4$ precursor phase was found to be ineffective, Co_3Mo_3N can serve as a very effective precursor for the rapid synthesis of $CoMoN_2$ at low temperatures.[155] Our best results were obtained by treating Co_3Mo_3N under flowing NH_3 at 400 °C for 1 hour, which produced $CoMoN_2$ with Co metal as the only observable impurity phase; reactions carried out at higher temperatures or for longer times exhibited increased impurity contents. A two-step ammonolysis reaction (first making Co_3Mo_3N as a precursor) was therefore used to produce bulk $CoMoN_2$ for structural and catalytic characterization.

Powder X-ray diffraction studies on $CoMoN_2$ suggest that it is isostructural with δ-MoN (Fig.4.1a),[132] with a = 2.85 Å, c = 2.75 Å, and space group symmetry *P-6m2* (No. 187). However, it should be noted that X-ray diffraction is dominated by scattering from Mo and Co

atoms and is very insensitive to the contributions of N atoms. This is particularly problematic in the case of three MoN polytypes (δ_1, δ_2, δ_3) which all contain the same arrangement of Mo atoms and differ only in the location of N atoms. These polytypes can all be indexed based on the simple WC-type lattice of δ-MoN when diffraction peaks are broad (as is the case for $CoMoN_2$) and XRD superstructure peaks are not resolvable. This occurs since only weakly scattering N atoms contribute intensity to the reflections of the superstructure peaks of δ_2-MoN (1 × 1 × 2 superstructure) and δ_3-MoN (2 × 2 × 2 superstructure),[132] where the ratio of the *a*- and *c*-lattice parameters relative to the simpler δ_1-MoN sublattice are specified. Based on prior structural data, all three molybdenum nitride structures can be described as having close packed layers of N atoms, with Mo atoms found in the voids between nitrogen layers. The coordination environment of the Mo ions is in either trigonal prismatic or octahedral, depending on whether successive nitrogen layers have the same lateral coordinates (*ie* AA) or are offset (*ie* AB).[132] Intriguingly, enhancement of the MoS_2 HER activity was recently achieved by converting the Mo environment from trigonal prismatic (2H polytype) to octahedral (1T polytype) by Li-intercalation.[97]

In order to overcome the sensitivity limitations of X-rays, neutron diffraction experiments were carried out to resolve the structure of $CoMoN_2$ since the scattering length of N (9.36 fm), Mo (6.72 fm) and Co (2.49 fm) are significantly different, giving excellent sensitivity to all species. Indexing of neutron diffraction data indicates that $CoMoN_2$ crystallizes in a 1 × 1 × 4 supercell (*a* ~2.85 Å, *c* ~11.01 Å) of δ_1-MoN. Different crystal structures previously reported for transition metal nitrides were tested via Rietveld refinement, and it was found that only the $Li_{0.67}NbS_2$ structure type with $P6_3/mmc$ (No. 194) space group symmetry effectively described the $CoMoN_2$ structure (Fig. 4.1b and Fig.4.2). To solve the structure, observed nuclear density

map derived from Fourier transformation is applied. In Fig. 4.3a, the nitrogen position can be clearly resolved due to the strong N coherent scattering length (9.36 fm) and is strongly elongated in the *c*-axis direction. The octahedral cation site (at $z = 0$ and 0.5) is less intense than the trigonal prismatic cation site (at $z = 0.25$ and 0.75) due to the smaller scattering factor for Co (2.49 fm) than for Mo (6.715 fm). In this structure, N ions are found in close packed layers with a repeating AABB stacking sequence while all transition metal ions are found between the N layers at the coordinates directly above/below the unoccupied C layer positions of nitrogens. This leads to alternating layers of trigonal prismatic and octahedral coordination for the transition metals (Fig. 4.3b).

Data suitable for Rietveld refinement was collected from three instruments in different configurations: on a laboratory X-ray diffractometer ($\lambda = 1.54$ Å) in a flat plate geometry, on the 11-BM high-intensity / high-resolution synchrotron X-ray diffraction beamline ($\lambda = 0.414$ Å) in transmission mode using an 0.8 mm diameter Kapton capillary, and on the time-of-flight neutron diffractometer NOMAD in transmission mode using a 2 mm diameter capillary. Although all three data sets could be co-refined using the TOPAS software package, this induced complications due to the different samples used in some experiments, the very different counting statistics of the different beamlines, and the different absorption corrections needed for the different instrument wavelengths and sample geometries (none for flat plate geometry, a refined cylindrical absorption correction with a packing fraction of 0.38 for the synchrotron data, and an empirical absorption correction for the neutron data produced by scaling the data as d^{4-p} instead of d^4, where a value of $0 < p < 1$ was refined independently for each bank). Since only the neutron diffraction data gave good sensitivity to all elements, this data set was used for the final structural refinement though with the lattice parameters provided from a fixed geometry

laboratory X-ray diffractometer to avoid the strong influence of the sample position on the observed neutron diffraction lattice parameters. The Co fraction on the octahedral site typically refined to a lower value in X-ray diffraction experiments (0.45 – 0.50) than in the neutron diffraction experiments (0.72 – 0.82); a similar value of 0.65 was obtained in neutron PDF refinements (carried out using PDFGui). The final Co content was therefore fixed to an intermediate value of 0.60 in the final refinement to combine the information from these two refinements. A common isotropic displacement parameter was used for all three cations (Mo on trigonal prismatic site, Mo on octahedral site, and Co on octahedral site). Anisotropic displacement parameters were refined for the nitrogen site, a treatment justified based on the highly elongated nuclear density seen in the calculated density maps. Two isotropic split N sites were less effective in modeling this density than a single anistropic N site. The major axes of the N anisotropic displacement parameters (ADPs) typically had a 1:1:10 ratio which was slightly aphysical, but probably represents the tendency of these variables to compensate for other imperfections in the refinement. A more reasonable 1:1:2 ratio of major axes was observed in pair distribution function (PDF) refinements. The PDF refinements are more directly sensitive to displacement parameters (results in a broadening of the PDF peaks), and probably represent more correct values of the ADPs.

Structural analogies to compounds such as $Fe_{0.8}Mo_{1.2}N_2$ suggest that Mo prefers the trigonal prismatic site (2a Wykoff position) while Co prefers the octahedral site (2b Wykoff position).[134] Although synthesis reactions were initiated with equimolar amounts of Co and Mo, and though there were no indications of the loss of Co through volatilization during the reactions, the presence of impurity peaks in the reaction product assigned to Co metal suggests that the cobalt molybdenum nitride phase is Mo-rich. The final crystallographic refinement was therefore

carried out with a Co/Mo mixture on the octahedral site. No evidence was found for non-stoichiometry on the trigonal prismatic Mo site or the nitrogen site during refinement. The cobalt molybdenum nitride was found to have the stoichiometry $Co_{0.6}Mo_{1.4}N_2$. This formula is consistent with the weight fraction of Co metal (~20%) present as a second phase obtained from Rietveld refinements of X-ray diffraction data, though it should be noted that this phase fraction determination is not precise due the broad Co diffraction peaks (Table 4.1-4.4).

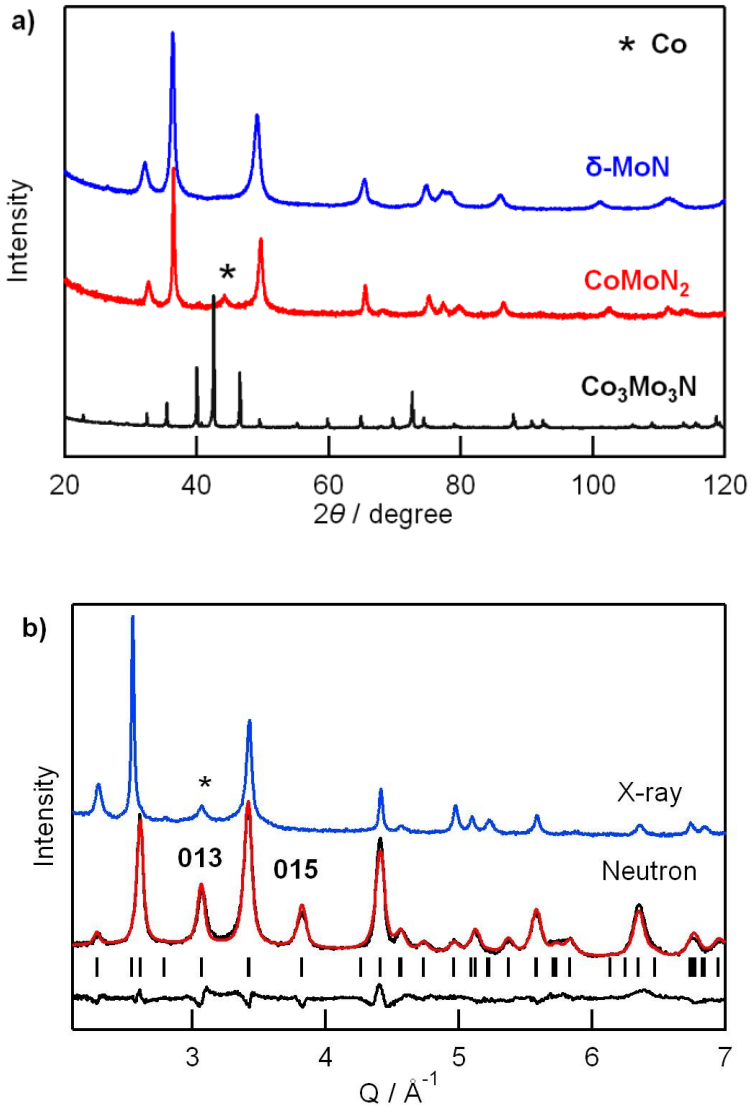

Figure 4.1 (a) Lab X-ray powder diffraction patterns of Co_3Mo_3N, $CoMoN_2$ and δ-MoN. Asterisk marks the impurity peak of cobalt metal. (b) Rietveld refinements of neutron diffraction for $CoMoN_2$ showing observed data (black line), calculated pattern (red line) and difference curve (bottom line). Lab X-ray diffraction data (blue line) in same Q (=2π/d) range between 2 and 7 $Å^{-1}$ do not clearly show superstructure peaks such as the 013 and 015 reflections which are intense in neutron diffraction data.

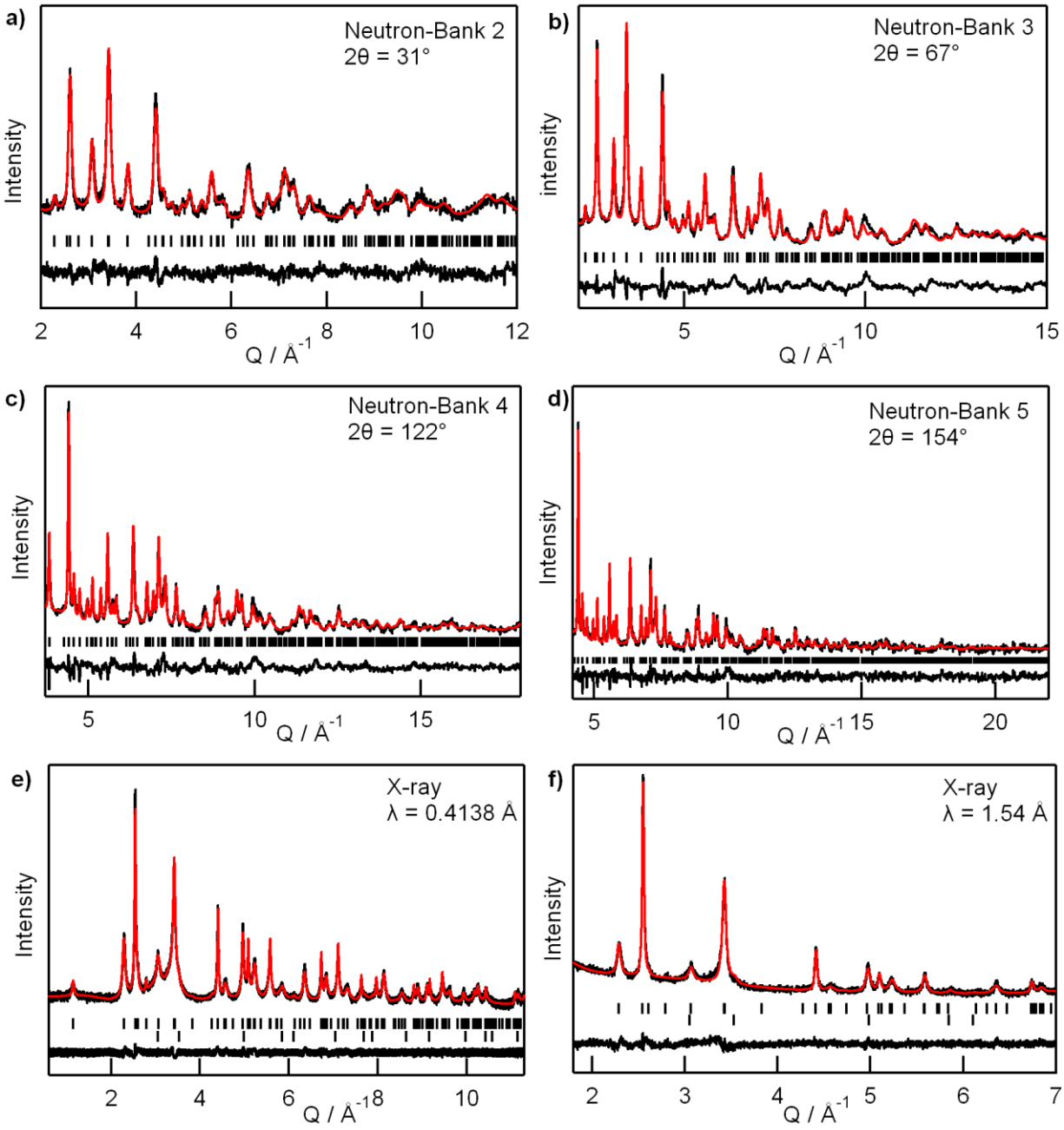

Figure 4.2 Rietveld refinement profiles for $CoMoN_2$ ($Co_{0.6}Mo_{1.4}N_2$ + Co metal) using time of flight neutron diffraction and X-ray data. The neutron detector banks are ordered by increasing scattering angles: (a) bank 2-2θ = 31°; (b) bank 3-2θ = 67°; (c) back 4-2θ = 122°; (d) bank 5-2θ = 154°.[9] X-ray data: (e) synchrotron X-ray (λ = 0.4138 Å); (f) lab X-ray (λ = 1.54 Å). The black line indicates the observed experimental data, the red line indicates the calculated data and the lower solid line indicates the difference curve. For X-ray data, upper tick marks are hkl for $Co_{0.6}Mo_{1.4}N_2$ phase while lower tick marks are hkl for Co phase.

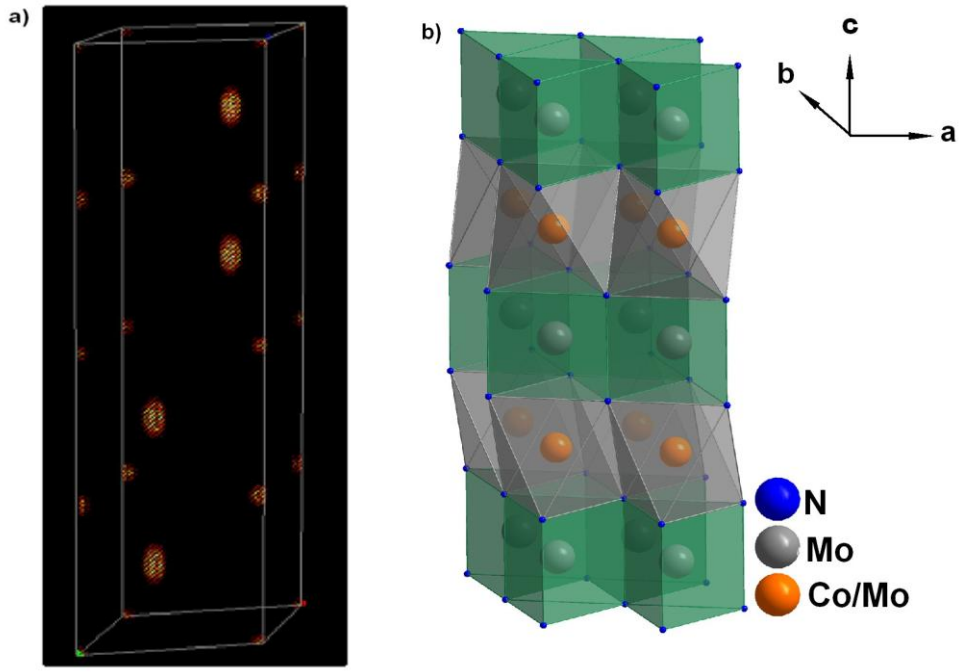

Figure 4.3 (a) Observed nuclear density map calculated for $Co_{0.6}Mo_{1.4}N_2$ using the time-of-flight neutron diffraction data from Bank 4. (b) Four-layered crystal structure of $Co_{0.6}Mo_{1.4}N_2$.

Table 4.1 Crystallographic data for $Co_{0.6}Mo_{1.4}N_2$.

Radiation	TOF neutron	NPDF	X-ray
Formula	$Co_{0.6}Mo_{1.4}N_2$	$Co_{0.6}Mo_{1.4}N_2$	$Co_{0.6}Mo_{1.4}N_2$
Crystal system	Hexagonal	Hexagonal	Hexagonal
Space group	*P*6$_3$/*mmc*	*P*6$_3$/*mmc*	*P*6$_3$/*mmc*
a (Å)	2.85176(2)	2.851(1)	2.85148(3)
c (Å)	10.9862(3)	11.009(8)	10.9890(3)
V (Å^3)	77.38	77.46	77.380(3)
λ	0.1Å – 3Å	0.1Å – 3Å	0.413832Å
R_{Bragg}	N/A	N/A	4.148%
R_{wp}	5.935%	14.65%	11.344%
R_p	4.975%	N/A	9.414%
χ^2	N/A	N/A	1.540

Table 4.2 Refined atomic positions for $Co_{0.6}Mo_{1.4}N_2$ based on neutron Rietveld refinement.

	Wyckoff	*x*	*y*	*z*	occupancy	U_{iso} *or* U_{ij} (Å^2)
Mo1	2*a*	0	0	1/4	1.0	0.0068(5)
Mo2	2*b*	0	0	0	0.4	0.0068(5)
Co	2*b*	0	0	0	0.6	0.0068(5)
N	4*f*	1/3	2/3	0.1269(2)	1.0	U_{11}= U_{22}=0.0010(3) U_{33}=0.0315(7) U_{12} =0.0005 U_{13}= U_{23}=0

Table 4.3 Refined atomic positions for $Co_{0.6}Mo_{1.4}N_2$ based on synchrotron X-ray Rietveld refinement.

	Wyckoff	*x*	*y*	*z*	occupancy	B_{eq} (Å^2)
Mo1	2*a*	0	0	1/4	1.0	0.54(2)
Mo2	2*b*	0	0	0	0.434	0.54(2)
Co	2*b*	0	0	0	0.566(5)	0.54(2)
N	4*f*	1/3	2/3	0.1295(6)	1.0	1.31(6)

Table 4.4 Refined atomic positions for $Co_{0.6}Mo_{1.4}N_2$ based on neutron pair distribution function data.

	Wyckoff	*x*	*y*	*z*	occupancy	*U* (Å^2)
Mo1	2*a*	0	0	1/4	1.0	U_{11}= U_{22}=U_{33}=0.0068(2)
Mo2	2*b*	0	0	0	0.36	U_{11}= U_{22}=U_{33}=0.0061 (3)
Co	2*b*	0	0	0	0.64	U_{11}= U_{22}=U_{33}=0.0061(3)
N	4*f*	1/3	2/3	0.1287(6)	1.0	U_{11}= U_{22}=0.0077(6) U_{33}=0.016(2) U_{12} =0.0038 U_{13}= U_{23}=0

Additional insights into the crystal structure of $Co_{0.6}Mo_{1.4}N_2$ have been obtained through "small box" fitting of the neutron pair distribution function (PDF) data, shown in Fig. 4.4. It can be seen that this structural model gives an excellent fit to the observed local structure over the length scale of 1.7 – 20 Å, suggesting that the average structure provides a very complete description of this compound even on the atomic scale. This indicates that amorphous phases are not present, as even glasses will give well-defined peaks in PDF spectra. As such, it is expected that the local environments of Co and Mo in the octahedral layer are indistinguishable, and that both ions are found at the same crystallographic position without clustering or ordering of ions within this layer. In contrast, the simple WC or NiAs structural models cannot effectively fit the PDF data (Fig. 4.5), confirming the presence of multiple Mo coordination environments, and highlighting the importance of the superstructure despite its visual absence in laboratory powder X-ray diffraction data.

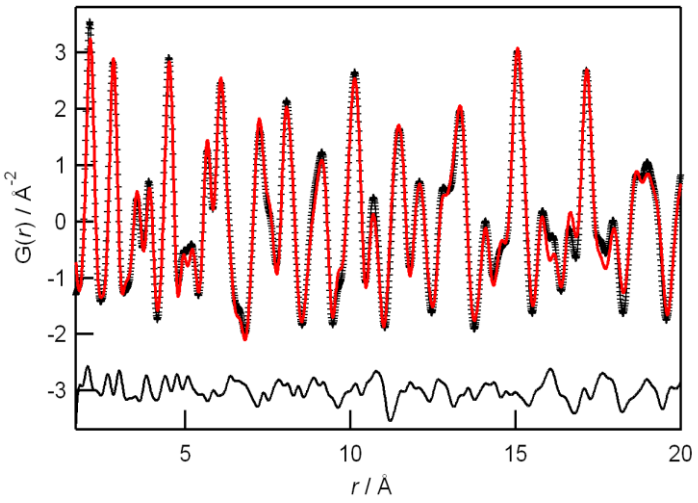

Figure 4.4 Neutron PDF fit from r = 1.7 Å to 20 Å for a two-phase nominal $CoMoN_2$ sample with a 1 × 1 × 4 WC-superstructure phase with $P6_3/mmc$ symmetry and Co metal (Fm-3m, No.225, a = 3.56 Å).

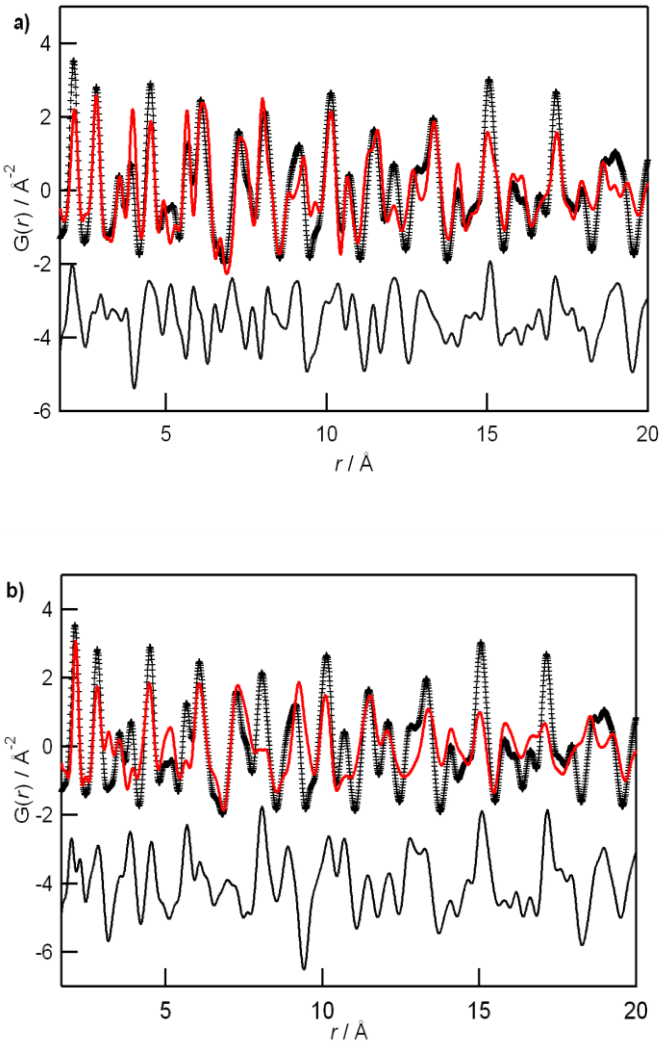

Figure 4.5 Neutron PDF fit from r = 1.7 Å to 20 Å for $CoMoN_2$ using rejected alternative models. (a) WC-type model (*P*-6*m*2, No. 187) with a random Co/Mo mixture on the trigonal prismatic site (R_{wp} = 55%). (b) NiAs-type model ($P6_3/mmc$, No. 194) with a random Co/Mo on the octahedral site (R_{wp} = 72%). For comparison, R_{wp} is 16% when the four layered structure model ($P6_3/mmc$, No. 194) is used.

4.3.2 Composition

The stoichiometry of the nominal $CoMoN_2$ sample can also be indirectly determined by thermogravimetric analysis. Black $CoMoN_2$ was completely oxidized to purple $CoMoO_4$ by heating the nitride in an oxygen atmosphere, as judged by powder X-ray diffraction (Fig. 4.6). The thermal response indicates that this is not a direct conversion. Two intermediate transitions were observed at mass gains of ~6% (~200 °C) and ~12% (~300 °C), and the maximum mass gain is seen at 500 °C, beyond which there is a slight mass decrease to a stable plateau which persists over a wide temperature range (600 – 800 °C). The product at 500 °C is mainly β-$CoMoO_4$ while product at higher temperature is a mixture of both α- and β-$CoMoO_4$. Based on a structural and bonding analysis of these phases, we believe that only β-$CoMoO_4$ contains integer valence metals (Co 2+ and Mo 6+) while the other α-$CoMoO_4$ polytype has slightly reduced Mo cations which are charge-compensated by oxygen deficiencies and a true stoichiometry of α-$CoMoO_{4-\delta}$. Thus only β-$CoMoO_4$ was used as a mass reference. The observed weight gain of $CoMoN_2$ during oxidation is 24.55 wt %, which is a little smaller than the theoretical weight gain of 25.16 wt % for the $CoMoN_2$ sample ($Co_{0.6}Mo_{1.4}N_2$ with the balance of Co present as Co metal). The smaller mass gain than expected during oxidation is attributed to the presence of a small amount of oxygen (0.61 wt %, 1.54 mol %) in the sample, which might be residing on the surface of the Co metal phase rather than being found in the $Co_{0.6}Mo_{1.4}N_2$ nitride phase. Residual oxygen is also observed in SEM-EDX analysis (Fig. 4.8) and XPS data (Table 4.6). The active material composition of $Co_{0.6}Mo_{1.4}N_2$ is therefore supported by TGA data.

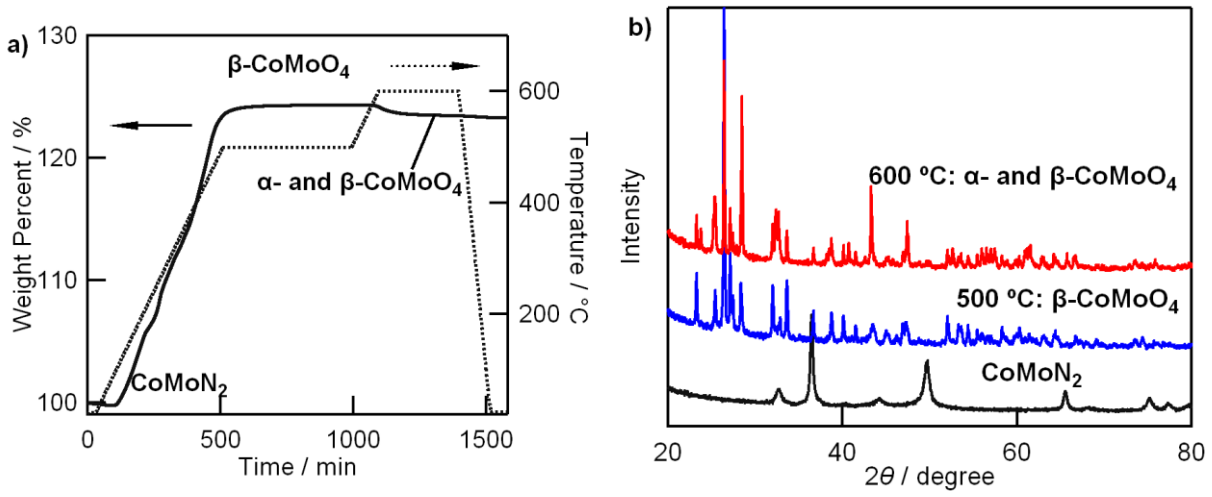

Figure 4.6 (a) Thermogravimetric response of $CoMoN_2$ ($Co_{0.6}Mo_{1.4}N_2$ + Co metal) heated under oxygen from room temperature to 600 °C. (b) XRD patterns of $CoMoN_2$ sample after decomposing at 600 °C (blue) and 500 °C (red) under flowing O_2 in TGA experiments, and before heating (black). The product heated at 500 °C consists of β-$CoMoO_4$ and the product heated at 600 °C contains a mixture of both α- and β-$CoMoO_4$ (α-$CoMoO_4$: β-$CoMoO_4$ = 62.50 wt% : 37.50 wt%).

4.3.3 Morphology

Insights into particle size and morphology were obtained from electron microscopy studies (Fig. 4.7). The oxide precursors $CoMoO_4$ are nanorods with diameters of 20-50 nm and lengths up to 200 nm. After ammonia treatment, the nanorod morphology is not retained. It can be seen in SEM images that the primary particle size of $Co_{0.6}Mo_{1.4}N_2$ has nanoscale dimensions (< 100 nm), and these primary particles are aggregated into larger secondary particles which can be more than a micron across. The secondary particle size is comparable with that of the Co_3Mo_3N precursor used in the synthesis. The primary particles of δ-MoN were substantially larger, suggesting that Co plays a role in minimizing the $Co_{0.6}Mo_{1.4}N_2$ particle size. TEM studies are able to resolve isolated crystallites of $Co_{0.6}Mo_{1.4}N_2$, and show that primary particles are typically obtained with a maximum dimension of ~80 nm but without well-defined facets. EDX analysis confirms that the existence of nitrogen species and the formation of nitride phase.

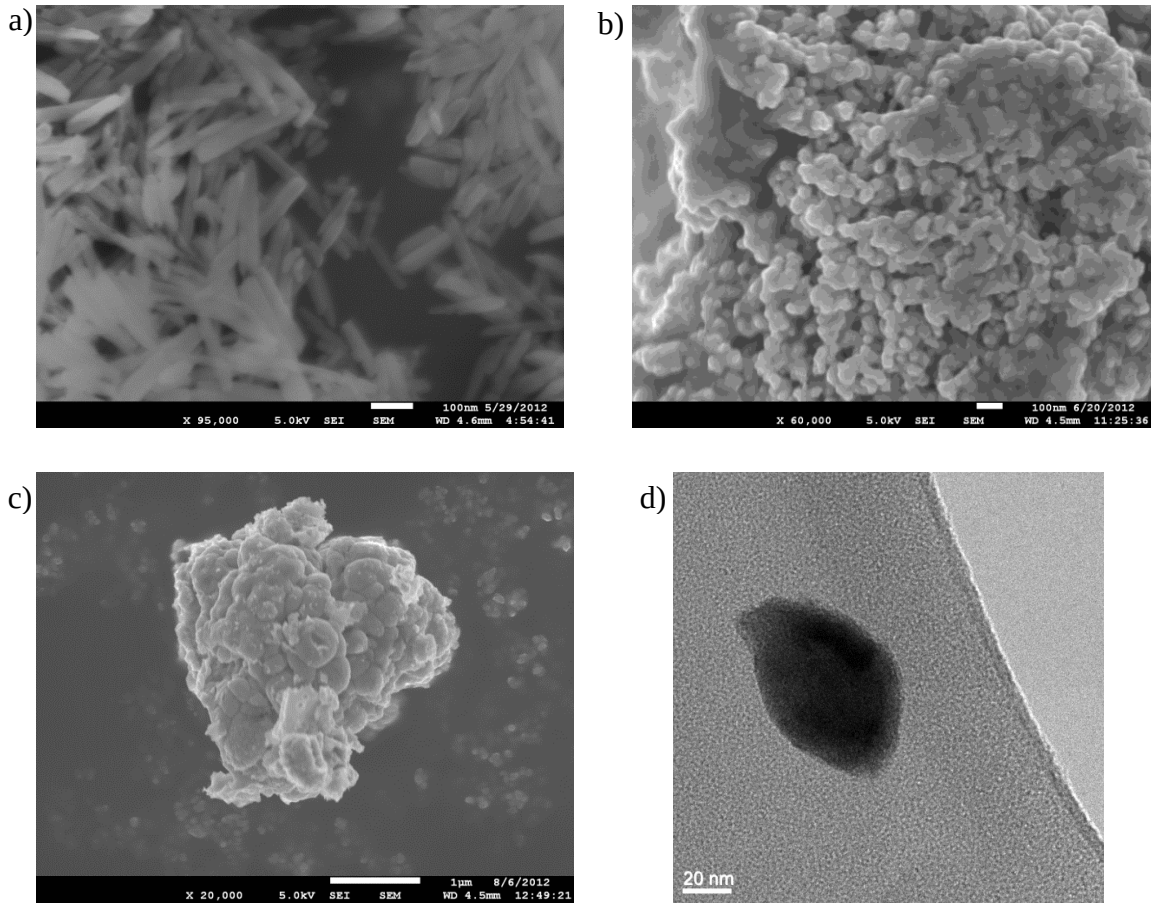

Figure 4.7 SEM images of (a) Amorphous $CoMoO_4$ precursor (scale bar: 100 nm); (b) $Co_{0.6}Mo_{1.4}N_2$ prepared at 400 °C (scale bar: 100 nm); (c) δ-MoN synthesized at 600 °C (scale bar: 1 µm) and TEM image of (d) single crystallite of $Co_{0.6}Mo_{1.4}N_2$ (scale bar: 20 nm).

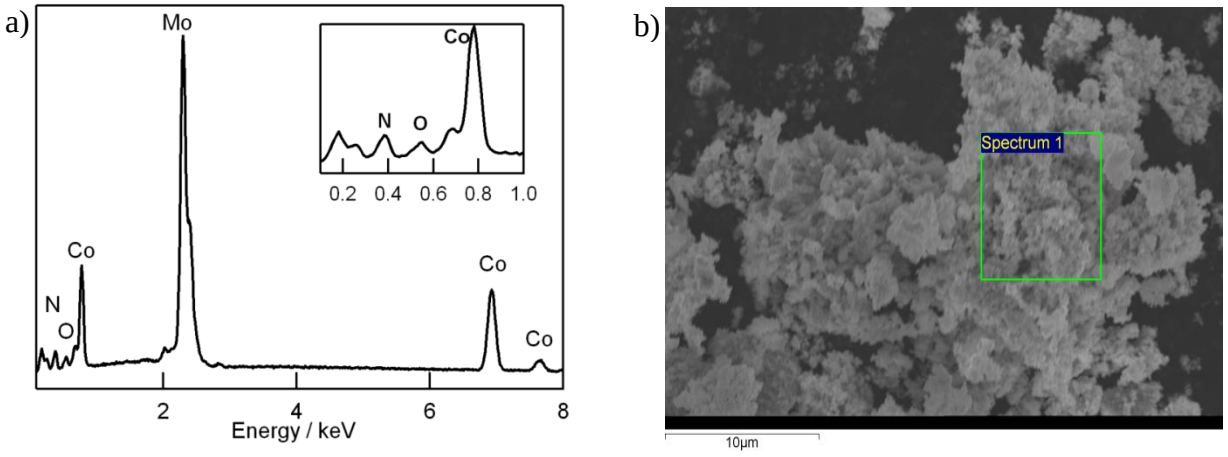

Figure 4.8 (a) EDX spectra of $Co_{0.6}Mo_{1.4}N_2$ showing the presence of Co, Mo, N and O based on the peaks in the emitted X-ray spectrum. The atomic ratio of Co: Mo: N: O is 30.37%: 24.61%: 42.44%: 2.58%. (b) SEM image indicating region over which EDX spectra were collected.

4.3.4 Valence and Bonding

Even in absence of detailed knowledge about the ORR and HER reaction mechanism in molybdenum nitrides, it is expected that catalytic activity will be sensitive to the Mo valence and coordination environment. Curiously, a wide range of different bulk Mo valence states are expected for MoS_2 (4+), MoN (3+), MoB (3+), and Mo_2C (2+). The idealized formula of ternary $CoMoN_2$ is expected to correlate with a 4+ valence of Mo that is raised relative to the 3+ valence of binary MoN, though the non-stoichiometric formula of $Co_{0.6}Mo_{1.4}N_2$ indicates a more complex situation. The composition of $Co_{0.6}Mo_{1.4}N_2$ corresponds to an average Mo valence of +3.4 if all Co is divalent, though the presence of cation vacancies in the structure will result in more oxidized Mo ions.

While a bond valence sum (BVS) analysis is often used to gain quantitative insights into the valence of oxides, it is difficult to apply this methodology to the present system since there are not enough close structural analogues with well-defined valence states and well-characterized structures to construct an accurate parameterization. However, meaningful insights into the Mo valence can still be obtained by comparing the Mo-N bond distances in the octahedral (2.17 Å) and trigonal prismatic (2.11 Å) sites of $Co_{0.6}Mo_{1.4}N_2$ to those in reference nitride compounds which also have 6-coordinate Mo (Table 4.5). MoN is an appropriate reference for 3+ Mo, and has been reported to have Mo-N bond distances of 2.16 – 2.17 Å in δ_1-MoN. Similar distances were reported for δ_2 and δ_3 polytypes.[132] These distances are in very good agreement with the sum of the Shannon ionic radii Mo^{3+} and N^{3-} with appropriate coordination number.[156] The octahedral sites in $Co_{0.6}Mo_{1.4}N_2$ can therefore be assigned a valence of 3+, while the trigonal prismatic sites must be higher in valence to account for their reduced Mo-N bond lengths.

The smaller trigonal prismatic average Mo-N bond length (0.06 Å shorter than the octahedral site) in $Co_{0.6}Mo_{1.4}N_2$ suggests a higher valence for this site. The Shannon ionic radii suggest a decrease in ionic radius of 0.04 Å on moving from Mo^{3+} to Mo^{4+}, though it should be noted that the ionic radii of these ions were assigned based on a limited data set (two halide structures for 3+, one halide structure for 4+). Based on its bond length (2.11 Å), the Mo valence on the trigonal prismatic site of $Co_{0.6}Mo_{1.4}N_2$ should be similar to that observed for $MnMoN_2$ (2.12 Å Mo-N bond length) and $Fe_{0.8}Mo_{1.2}N_2$ (2.13 Å) and is probably near 4+ based on these analogies.[134,144] This is larger than the +3.6 valence of the trigonal prismatic site calculated for the $Co_{0.6}Mo_{1.4}N_2$ stoichiometry obtained (assuming that the octahedral site is a mixture of divalent Co and trivalent Mo), though this valence could be raised all the way to +4 if there are ~20% vacancies on the octahedral cation site. The compound $LiMoN_2$ is expected to have a 5+ Mo valence, and has been reported to have Mo-N bond length of 2.09 Å[157] which is substantially shorter than observed for $Co_{0.6}Mo_{1.4}N_2$. An analysis of crystal field levels (Fig. 4.9) suggests that Mo^{4+} (d^2) can benefit from the distortions associated with a trigonal prismatic environment while Mo^{3+} (d^3) cannot, and that the observed structure of $Co_{0.6}Mo_{1.4}N_2$ does an excellent job of satisfying the bonding preferences associated with the partial oxidation of Mo^{3+}. Similar bonding factors presumably drive the conversion of trigonal prismatic 2H-MoS_2 to octahedral 1T-Li_xMoS_2 (and the accompanying increase in catalytic activity) during the reductive intercalation of Li. In contrast to octahedral 1T-MoS_2 (which was found to transform back to 2H-MoS_2 over a period of weeks[97]), the charge balance in $Co_{0.6}Mo_{1.4}N_2$ is provided by a divalent ion that should be fully immobilized at room temperature allowing the trivalent octahedral Mo^{3+} that is presumably responsible for the enhanced HER activity to be very effectively stabilized.

Table 4.5 Comparison of refined bond distances for $Co_{0.6}Mo_{1.4}N_2$ obtained through diffraction data (neutron and X-ray) and through neutron PDF fitting results.

Bond	Distance (Å)		
	Neutron	Neutron PDF	X-ray
Mo1-N	2.111(2)	2.120(5)	2.113(4)
Co/Mo2-N	2.178(2)	2.171(6)	2.176(5)
Co/Mo2-Mo1	2.747	2.752(2)	2.747
Co/Mo2-Co/Mo2	2.852	2.851(1)	2.852
Mo1-Mo1	2.852	2.851(1)	2.852
N-N [a]	2.642(6)	2.67(2)	2.65(1)

[a] N – N distance refers to the vertical distance between trigonal prismatic nitrogen layers. The in-plane N – N distances are exactly equal to the *a*-lattice parameter (2.85 Å).

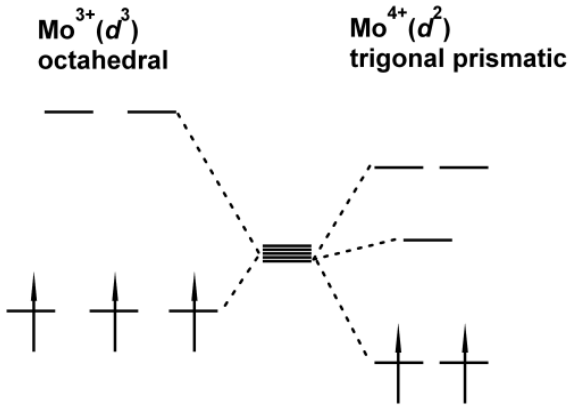

Figure 4.9 Mo^{3+} (d^3) configuration of an octahedral site (left) and Mo^{4+} (d^2) configuration in a trigonal prismatic site (right), both of which represent the preferred geometry for their indicated oxidation state.

4.3.5 Surface Property

Further insights into the valence of transition metals at the $Co_{0.6}Mo_{1.4}N_2$ catalyst surface were obtained through XPS measurements (Fig. 4.10). Although Co species may not be directly involved in the ORR and HER reaction mechanism, knowledge of the Co valence will be helpful in understanding the Mo valence through charge balance arguments, and the results of the XPS are summarized in Table 4.6. Surprisingly, the composition determined from the XPS analysis (Table 4.7) suggests that the sample surface is enriched in Co relative to Mo (1.8:1 Co:Mo ratio, vs. 1:1 ratio of starting materials in synthesis). The dominant peak (49%) in the Co $2p_{3/2}$ XPS spectrum at 781.1 eV is from Co^{2+} coordinated to O or N ions, and is attributed to the $Co_{0.6}Mo_{1.4}N_2$ phase. The impurity phase of metallic Co can be seen at 778.5 eV (12%) and the Co^{3+}-O/N bonds which appear at 784 eV (22%) are probably due to the surface oxidation of metallic Co. The remainder of the contribution from the Co metal phase is observed at 787 eV (17%) associated with Co-OH moieties resulting from the reaction of Co metal (or even oxides) with moisture in air.[158] The assignment of a bulk Co valence of 2+ in $Co_{0.6}Mo_{1.4}N_2$ catalyst is supported by this XPS data despite the small amount of observed Co^{3+}, which is believed to only occur through surface oxidation.

The analysis of the $Co_{0.6}Mo_{1.4}N_2$ Mo 3d XPS spectra is more complex due to a spin-orbit coupling feature that splits the 3d response into separate $3d_{5/2}$ and $3d_{3/2}$ peaks. MoO_3 was used as a reference to determine the separation and relative intensities of Mo $3d_{5/2}$ and $3d_{3/2}$ peaks. Fitting of the $Co_{0.6}Mo_{1.4}N_2$ data reveals three Mo $3d_{5/2}$ species: $Mo^{2/3+}$ (229 eV, 55%), $Mo^{3/4+}$ (230 eV, 22%) and Mo^{6+} (232 eV, 22%). In the context of the analysis of bond distances, the first peak is ascribed to Mo^{3+}, the second peak is assigned to Mo^{4+} in the prismatic layer, and the final peak of Mo^{6+} is attributed to surface Mo species that have been oxidized upon air exposure.

There is clearly strong ionic character in $Co_{0.6}Mo_{1.4}N_2$, unlike the precursor compound Co_3Mo_3N which exhibits a substantial fraction of Mo^0 and Co^0 character in its XPS spectra (Table 4.6). The observed mixture of valence states in $Co_{0.6}Mo_{1.4}N_2$ suggests that the ORR and HER electrocatalysis is associated with either the 3+/4+ or 4+/6+ pairs of valence states.

Understanding N 1s XPS peaks is important for nitride compounds, but can only be accomplished after accounting for the effects of partially overlapping Mo $3p_{3/2}$ peaks. This allows two N 1s peaks to be resolved. The major species is N-Co/Mo (397 eV, 77%) which confirms that the surface of $Co_{0.6}Mo_{1.4}N_2$ remains a nitride even after air exposure. This is consistent with the composition calculated by analyzing peak areas (Table 4.7), which suggests that the majority of anions at the surface are nitrogens. The N-Co/Mo binding energy is closer to the value expected for Mo-N bonds (396.7 eV) than for Co-N bonds (398.1 eV).[126] The other visible N 1s species is assigned to NH groups (399 eV, 23%) which demonstrates that H species are abundant at the sample surface. Although the origin of the surface H is likely due to an adventitious process such as incomplete reaction with NH_3 or reaction with moisture, this signal does indicate that N ions at the sample surface are able to strongly interact with H species, and that a large number of N-H moieties should be available to participate in the HER reaction mechanism if a reaction pathway of this type is energetically favorable.

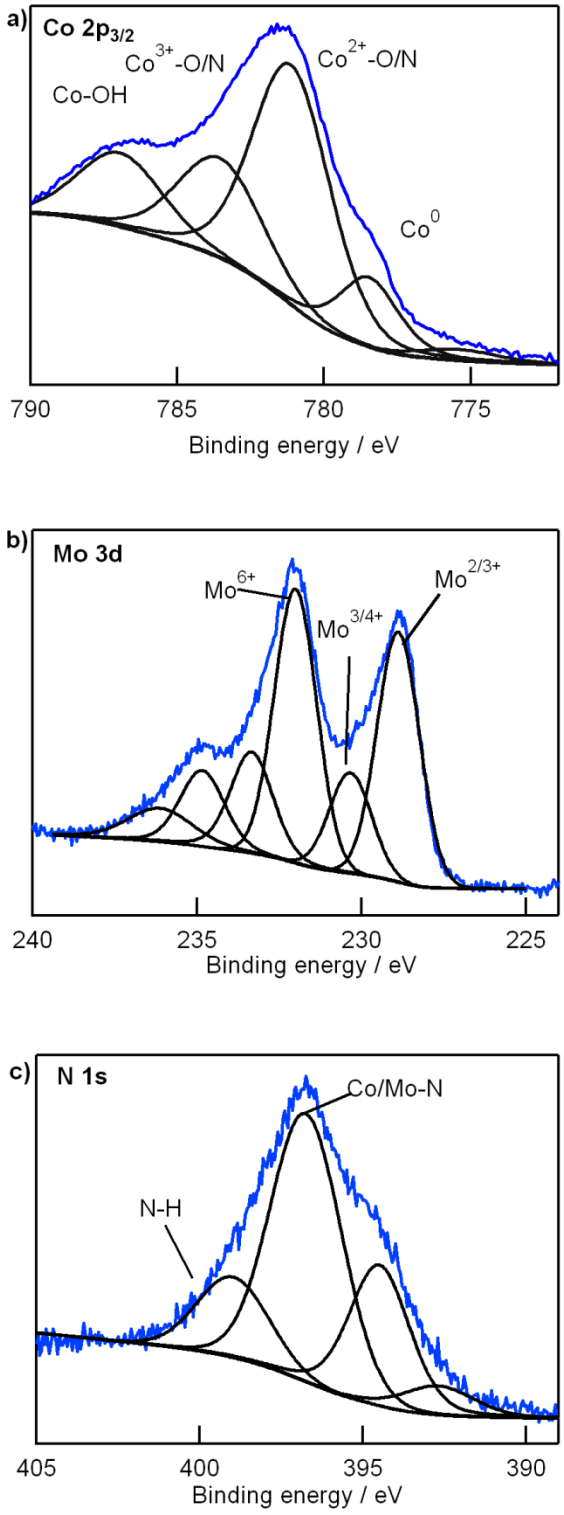

Figure 4.10 XPS spectra of $Co_{0.6}Mo_{1.4}N_2$: (a) Co 2p, (b) Mo 3d and (c) N 1s.

Table 4.6 XPS analysis of Co_3Mo_3N and $CoMoN_2$.

Sample	Mo $3d_{5/2}$			Mo $3d_{5/2}$ / $3d_{3/2}$	Co $2p_{3/2}$			
	Mo^0	$Mo^{2/3+}$	$Mo^{3/4+}$	Mo^{6+}	Co^0	Co^{2+}-O/N	Co^{3+}-O/N	Co^{2+} -OH
Co_3Mo_3N	227.77	228.86	231.09	232.25	778.39	781.16	783.54	
%[a]	26.7	28.6	39.9	4.8	24.0	51.7	24.3	
$CoMoN_2$		228.89	230.34	232.01	778.49	781.12	783.55	786.96
%[a]		55.4	22.2	22.4	12.0	49.0	22.3	16.7

Sample	Mo $3p_{3/2}$		N 1s		O 1s	
			Co/Mo-N	N-H	Co/Mo-O	Co/Mo-OH or C-O
Co_3Mo_3N	393.81	395.64	397.73	399.79	530.46	533.52
%[b]			83.7	16.3	90.0	10.0
$CoMoN_2$	392.67	394.50	396.75	398.98	531.10	
%[b]			77.0	23.0	100	

[a] Due to the overlap of the Mo $3d_{3/2}$ signals from the $Mo^{2/3+}$ and $Mo^{3/4+}$ species with the Mo$3d_{5/2}$ signal of Mo^{6+} the concentrations of $Mo^{2/3+}$, $Mo^{3/4+}$ and Mo^{6+} species were estimated by measuring the Mo $3d_{5/2}$ and Mo $3d_{3/2}$ signals, using a least squares fit for MoO_3, and calculating the relative intensity of these two signals (Mo $3d_{5/2}$:Mo $3d_{3/2}$ = 1.8). This factor was used to estimate the Mo $3d_{3/2}$ intensity from the $Mo^{2/3+}$ and $Mo^{3/4+}$ species, which overlap with the Mo $3d_{5/2}$ signal for Mo^{6+} (~233 eV). The percent of each Mo^{6+} surface species was then estimated by subtracting the calculated Mo $3d_{3/2}$ signal from the $Mo^{2/3+}$ and $Mo^{3/4+}$ species, then normalizing the percent species to this calculated value.

[b] N concentrations calculated removing Mo 3p component.

Table 4.7 Atomic fractions calculated from XPS analysis of Co_3Mo_3N and $CoMoN_2$.

Sample	C:Co:Mo:O:N	Co:Mo:O:N
Co_3Mo_3N	15.8:15.1:13.7:35.0:20.3	18.0:16.3:41.6:24.2
$CoMoN_2$	18.7:16.2:9.1:36.3:19.8	19.9:11.2:44.6:24.3

4.3.6 ORR Performance

The ORR electrocatalytic activity of $Co_{0.6}Mo_{1.4}N_2$ was tested to determine the influence of cobalt-doping and particle morphology on performance, and to learn if enhancements could be achieved relative to δ-MoN. Figure 4.11 shows the typical voltammograms for oxygen reduction using a $Co_{0.6}Mo_{1.4}N_2$ modified electrode in 0.1 M $HClO_4$ solution. The reduction peak around 0.33 V vs. RHE is observed under both atmosphere and for other molybdenum nitrides. Hence, this peak is attributed to the reduction of Mo species to Mo^{3+}.[135] The current difference of CVs collected under Ar and O_2 is considered to be the ORR current. The ORR onset potential, E_{onset} is defined as the potential when the current density is 25 μA/cm^2. E_{onset} of $CoMoN_2$ reaches 0.713 V vs. RHE which is higher than that of δ-MoN (E_{onset} = 0.680 V). As can be seen in Fig. 4.12a, $Co_{0.6}Mo_{1.4}N_2$ exhibits a larger current density than hexagonal δ-MoN at all relevant potentials. $Co_{0.6}Mo_{1.4}N_2$ also has a smaller Tafel slope (90 mV/dec) than δ-MoN (100 mV/dec) which further supports the conclusion that oxygen can be reduced more easily on $Co_{0.6}Mo_{1.4}N_2$ than on monometallic MoN (Fig. 4.12b). The enhanced activity of $Co_{0.6}Mo_{1.4}N_2$ relative to δ-MoN is due to changes in both morphology and the electronic structure that Co substitution induces.

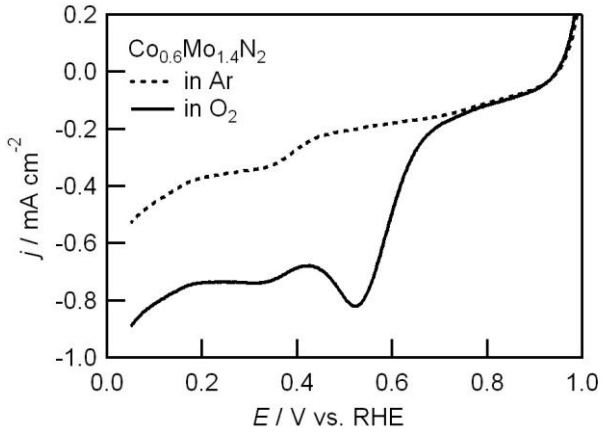

Figure 4.11 Linear sweep voltammograms for $Co_{0.6}Mo_{1.4}N_2$ in Ar and O_2 collected in 0.1 M $HClO_4$.

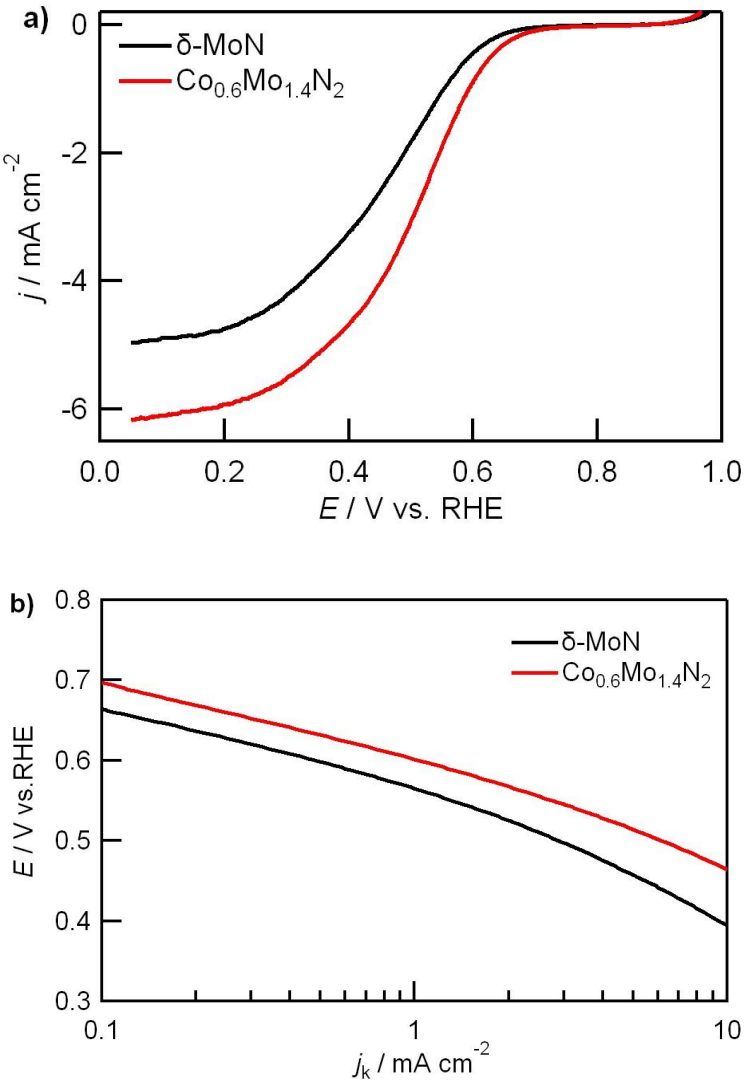

Figure 4.12 (a) RDE curves of δ-MoN and $Co_{0.6}Mo_{1.4}N_2$ collected in O_2-saturated 0.1 M $HClO_4$. (b) Corresponding Tafel plots of δ-MoN and $Co_{0.6}Mo_{1.4}N_2$.

To test the influence of substitution element on activity, the ORR activities of $FeMoN_2$ and $CoMoN_2$(s) are also compared to that of $Co_{0.6}Mo_{1.4}N_2$ (Fig. 4.13). $CoMoN_2$(s) synthesized by solid form has a lower cobalt doping level than $Co_{0.6}Mo_{1.4}N_2$ synthesized by gaseous form and that results in a lower ORR activity of $CoMoN_2$(s). The catalytic activity of $FeMoN_2$ is shifted to more negative potentials by about 0.10 V, indicating that the activity is robust in this structural family while Co is more effective in increasing the activity. It should again be noted that Co_3Mo_3N is inactive for ORR, and that more than just the presence of these three atom types is needed for good catalytic activity. It therefore suggested that the major enhancements are the introduction of Co and the change of crystal structure.

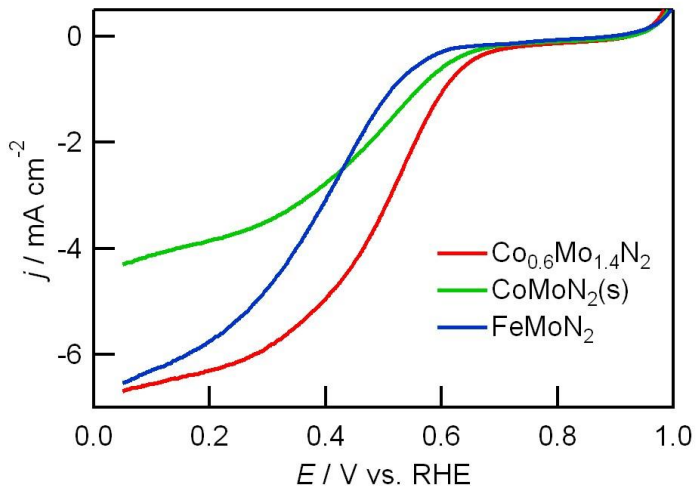

Figure 4.13 RDE curves of $Co_{0.6}Mo_{1.4}N_2$, $CoMoN_2$(s) and $FeMoN_2$ in O_2-saturated 0.1 M $HClO_4$.

The ORR mechanism of $Co_{0.6}Mo_{1.4}N_2$ was studied through RDE measurements at different rotation speeds (Fig. 4.14). Polarization curves collected at 400 to 2500 rpm were used to determine the number of transferred electrons, *n*, during the oxygen reduction process. Below 0.50 V vs. RHE, the calculated electrons *n* is 4.07 – 4.14 which indicates a four-electron pathway is dominant for ORR in that potential range. Above 0.50 V vs. RHE, oxygen reduction occurs through both two and four electron pathways. Further optimization on $Co_{0.6}Mo_{1.4}N_2$ is needed in order to catalyze the ORR via a 4*e* process at higher electrode potential. Although cobalt-containing compounds are typically easily dissolved in acid solution, $Co_{0.6}Mo_{1.4}N_2$ is relatively stable under strongly acidic conditions. The electrochemical capacitance after durability tests showed a slight reduction which indicated the decrease of active surface area or dissolution of Co metal (Fig. 4.15a). However, the ORR performance of $Co_{0.6}Mo_{1.4}N_2$ remained active after 2000 cycles and no obvious decay was observed (Fig. 4.15b).

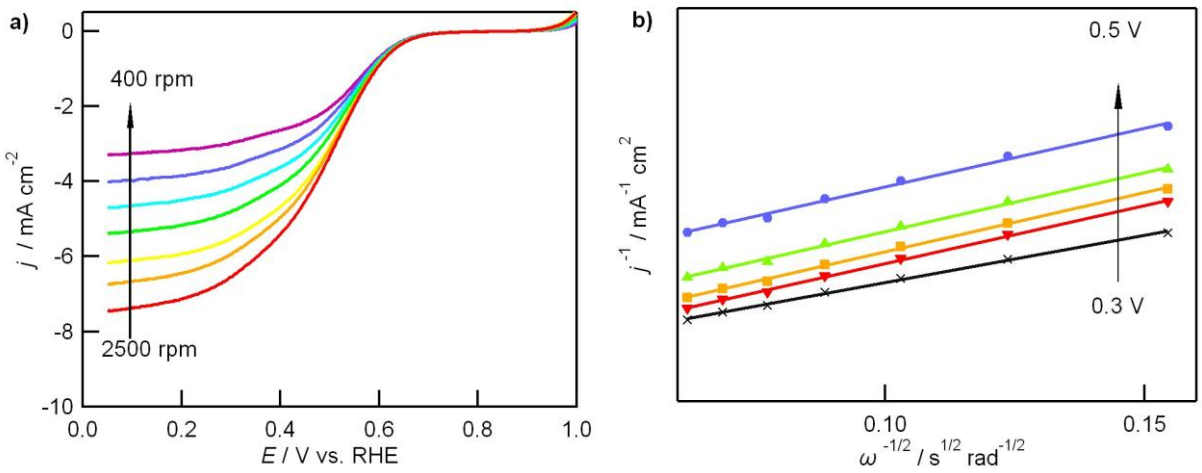

Figure 4.14 ORR data collected in 0.1 M $HClO_4$: (a) RDE curves of $Co_{0.6}Mo_{1.4}N_2$ at the rotating speed of 400 to 2500 rpm. (b) Corresponding Koutecky-Levich plots in the potential range of 0.30 V to 0.50 V vs. RHE.

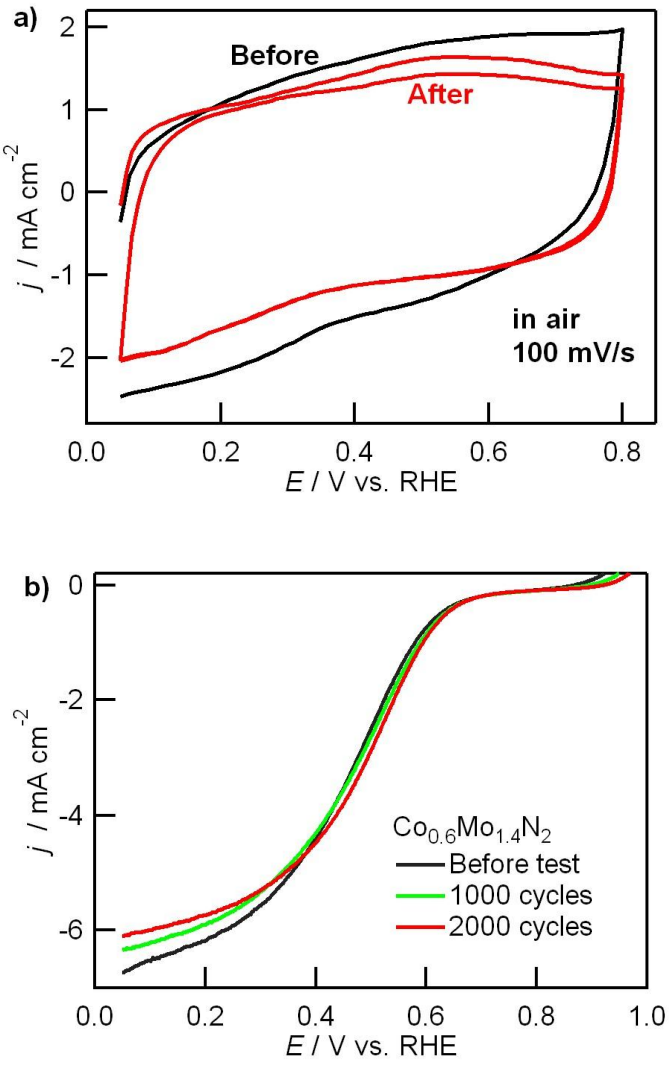

Figure 4.15 (a) CV curves of $Co_{0.6}Mo_{1.4}N_2$ before (black) and after (red) durability test. CVs were measured in air saturated 0.1 M $HClO_4$ from 0.05 to 0.8 V vs. RHE at a scan rate of 100 mV/s. (b) RDE curves of $Co_{0.6}Mo_{1.4}N_2$ in O_2 before and after durability tests. Durability tests were performed by applying linear potential sweeps between 0.05 to 0.8 V vs. RHE at a scan rate of 100 mV/s.

4.3.7 HER Performance

The characterization of ternary $Co_{0.6}Mo_{1.4}N_2$ for HER activity is of particular interest given the high activity for chemical analogues such as MoS_2 [83,97,99] and Ni-Mo-N nanosheets[105]. A typical polarization curve of $Co_{0.6}Mo_{1.4}N_2$ in acidic media (0.1 M $HClO_4$) under H_2 atmosphere measured in a RDE configuration is shown in Fig. 4.16, and it can be seen that large currents are achieved at modest overpotentials (~0.2 V), indicating excellent catalytic activity in samples prepared using a Co_3Mo_3N precursor that shows poor activity for HER.

Data are also shown for Co metal and δ-MoN which were produced by nitridation to simulate the plausible binary reaction byproducts (Fig. 4.17). The activity of $Co_{0.6}Mo_{1.4}N_2$ is far higher than the binary phases which are stable under reaction conditions, strongly suggesting that $Co_{0.6}Mo_{1.4}N_2$ is the active phase for HER. The as-measured $Co_{0.6}Mo_{1.4}N_2$ reaction currents do not directly reflect the intrinsic sample behavior due to the effects of Ohmic resistance, which was determined to be approximately 25 Ω measured by electrochemical impedance spectroscopy (EIS). An *iR* correction was therefore applied to the initial data, and this corrected data (dashed line, Fig. 4.17) was used for further analysis. A catalytic current of 10 mA/cm^2 is achieved at a potential of -0.20 V vs. RHE, with this overpotential only about 0.1 V larger than needed for a Pt/C catalyst system tested under identical conditions.

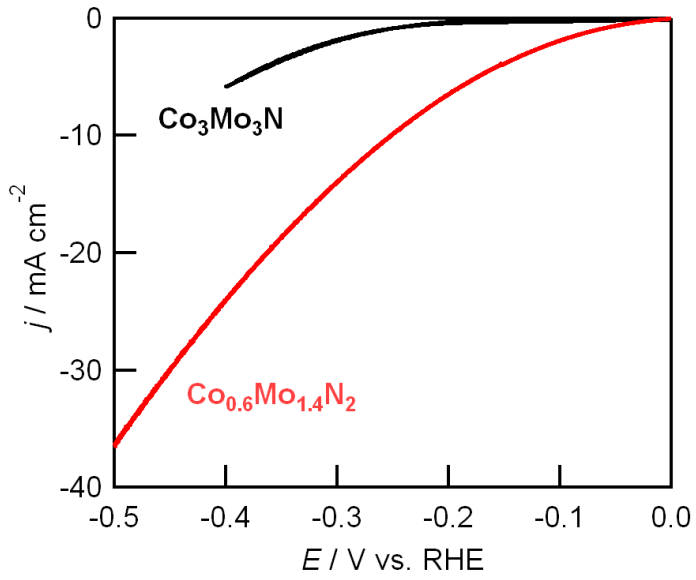

Figure 4.16 Polarization curves for Co_3Mo_3N (0.24 mg/cm^2) and $Co_{0.6}Mo_{1.4}N_2$ (0.24 mg/cm^2) measured on RDE (1600 rpm) in H_2-saturated 0.1 M $HClO_4$ without *iR* correction.

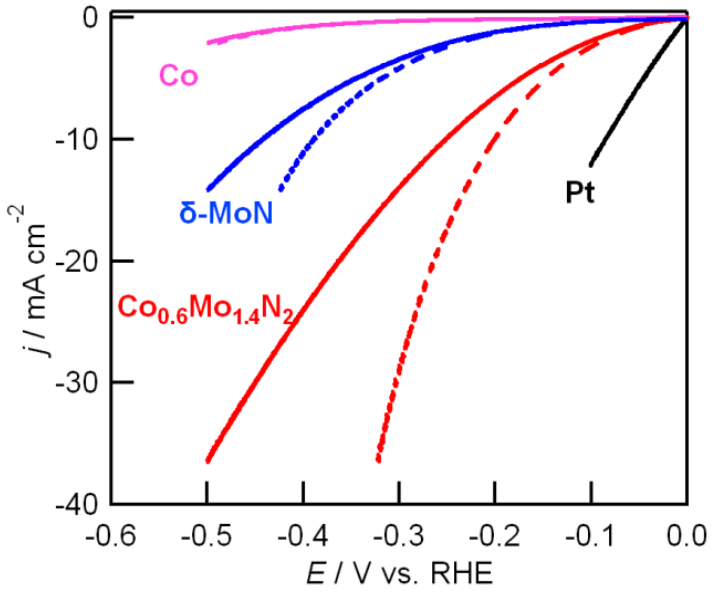

Figure 4.17 Polarization curves of Co, δ-MoN, $Co_{0.6}Mo_{1.4}N_2$ and Pt in H_2-saturated 0.1 M $HClO_4$ with (dotted line) and without (solid line) *iR*-correction.

Although the $Co_{0.6}Mo_{1.4}N_2$ samples prepared from Co_3Mo_3N have a reasonable electronic conductivity and show good activity even in the absence of additives, the catalytic current is approximately halved when a conductive additive (carbon black) is omitted from the catalyst ink (Fig. 4.18). Another factor potentially limiting the measured HER activity is the bubbles of gaseous hydrogen evolved during the reaction. However, measurements carried out using carbon paper with good porosity and a low resistance (3.5 Ω by EIS) in place of a RDE show a lower HER activity (Fig. 4.19). This indicates that mass diffusion is limiting electrocatalytic activity in the absence of electrode rotation, as might be expected for a highly active catalyst.

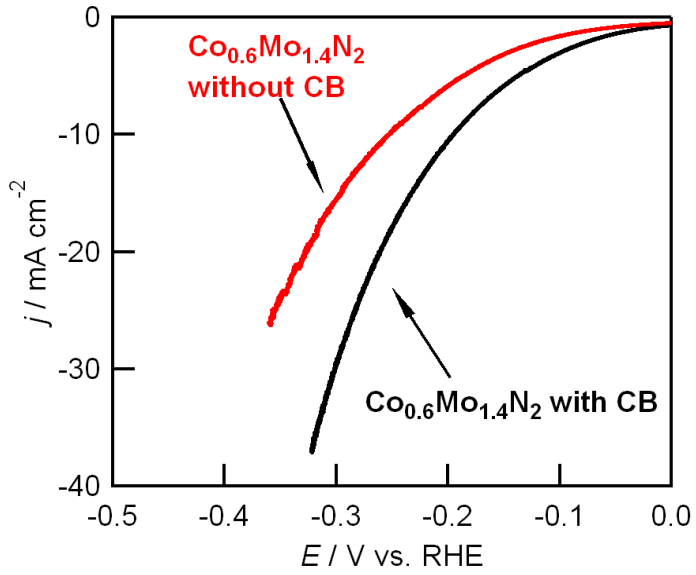

Figure 4.18 Polarization curves for $Co_{0.6}Mo_{1.4}N_2$ ink with (black line) and without (red line) carbon black measured on RDE (1600 rpm) in H_2-saturated 0.1 M $HClO_4$ after *iR* correction.

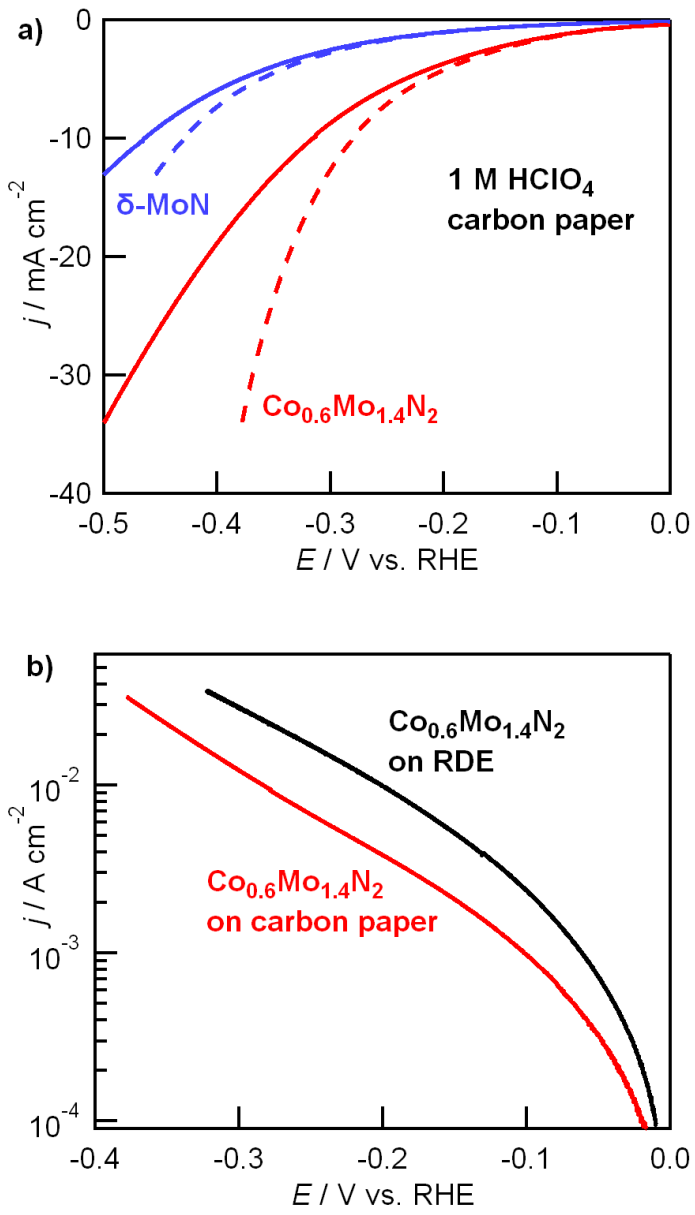

Figure 4.19 (a) Polarization curves for δ-MoN (0.105 mg/cm^2) and $Co_{0.6}Mo_{1.4}N_2$ (0.224 mg/cm^2) measured on carbon paper in H_2-saturated 1 M $HClO_4$ with (solid line) and without (dashed line) *iR* correction. (b) Comparison of $Co_{0.6}Mo_{1.4}N_2$ activity measured on RDE (1600 rpm) and on carbon paper in acidic solution after *iR* correction.

The *iR*-corrected activity of $Co_{0.6}Mo_{1.4}N_2$ is rescaled and shown in the form of a Tafel plot together with the data on δ-MoN and Pt (Fig. 4.20), which can be used to better understand the relative performance of these systems. The simpler binary system δ-MoN requires a large overpotential (~0.3 V) before substantial catalytic currents of 5 mA/cm^2 are obtained. The lower activity of δ-MoN is reflected in the low exchange current density, j_0, of 1.5 × 10^{-5} A/cm^2 obtained from curve fitting using a unidirectional Butler-Volmer equation

$$j = j_0[\exp(\frac{\alpha n F \eta}{RT})] \quad (4.1)$$

At small current density (low overpotential) region, the Eq.4.1 can be simplified to Eq.4.2

$$j = j_0 \frac{nF}{RT}\eta \quad (4.2)$$

while j_0 = 0.8 × 10^{-5} A/cm^2 for δ-MoN is found from linear fits to the low-overpotential region (Fig. 4.21).[159] The δ-MoN exchange current is far less than the j_0 = 2.2 × 10^{-3} A/cm^2 obtained from Pt in the linear regime. In contrast, a $Co_{0.6}Mo_{1.4}N_2$ exchange current of j_0 = 2.3 × 10^{-4} A/cm^2, which is within a single order of magnitude of the Pt activity, illustrates the high catalytic activity of this system. This exchange current density compares favorably with other Mo-based catalysts (Table 4.8). A simple analysis of the Tafel slope of $Co_{0.6}Mo_{1.4}N_2$ is not possible as the logarithm of current density does not increase linearly with overpotential, signifying that the current is mass-transport controlled[160] and/or that evolved hydrogen gas is limiting the available surface area and reaction rate at higher current densities. A robust mechanistic analysis will require more crystalline films, which will be the subject of future investigations.

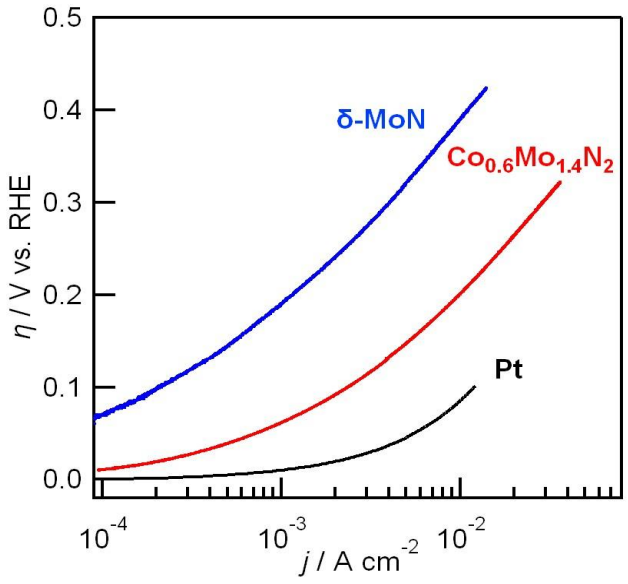

Figure 4.20 Tafel plots of δ-MoN, $Co_{0.6}Mo_{1.4}N_2$ and Pt in 0.1 M $HClO_4$ with *iR*-correction.

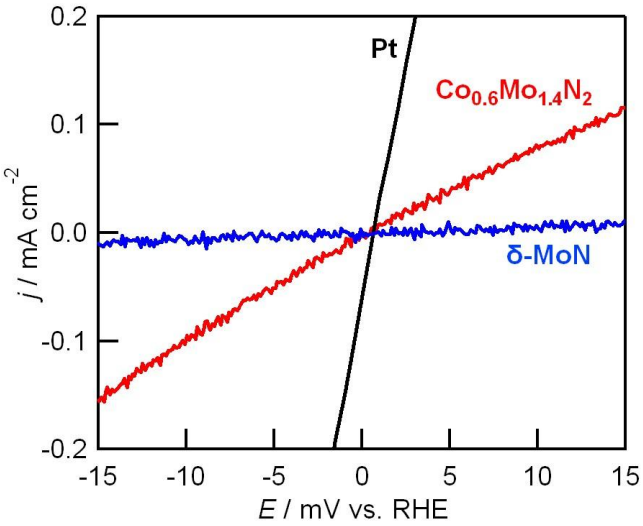

Figure 4.21 Current densities of δ-MoN, $Co_{0.6}Mo_{1.4}N_2$ and Pt in 0.1 M $HClO_4$ at low overpotentials after *iR*-correction.

Table 4.8 Comparison of HER activity measured for $Co_{0.6}Mo_{1.4}N_2$ with that reported for other systems with known HER activity under acidic conditions.[83,93,97,99,103-106]

Catalyst	Loading (mg/cm^2)	Electrode	Electrolyte	Current density (mA/cm^2)	Over-potential (mV vs. RHE)	Exchange current density (A/cm^2)
$Co_{0.6}Mo_{1.4}N_2$	0.243	Glassy carbon	0.1M $HClO_4$	10	~190	2.3×10^{-4}
Ni_2P	1	Ti foil	0.5M H_2SO_4	20	130	3.3×10^{-5} 4.91×10^{-4}
2H-MoS_2 film	N/A	Glassy carbon	0.5M H_2SO_4	1	300	2.2×10^{-6}
MoS_2/ MoO_3	N/A	FTO	0.5M H_2SO_4	2	200	N/A
1T-Li_xMoS_2	N/A	Graphitic rod	0.5M H_2SO_4	10	185	N/A
Bulk Mo_2C	3.3	Carbon paste electrode	0.5M H_2SO_4	20	~240	1.3×10^{-6}
Bulk MoB	2		0.5M H_2SO_4	20	~240	1.4×10^{-6}
Mo_2C/CNT	2	Carbon paper	0.1M $HClO_4$	10	~150	1.4×10^{-5}
Ni-Mo-N	0.25	Glassy carbon	0.1M $HClO_4$	3.5	~200	2.4×10^{-4}
Ni-Mo	3	Ti foil	0.5M H_2SO_4	10	80	N/A

The faradaic yield of H_2 production by $Co_{0.6}Mo_{1.4}N_2$ after delivery of 30 Coulombs of charge was determined to be essentially stoichiometric (> 90%) by galvanostatic electrolysis. The stability of $Co_{0.6}Mo_{1.4}N_2$ during hydrogen production is excellent, as illustrated in Fig. 4.22. The activity of the catalyst slightly changes over the first 50 cycles due to surface cleaning or molybdenum reduction between +0.2 and -0.3 V vs. RHE, but remains unchanged afterwards over the test period of 3000 cycles in 0.1 M $HClO_4$. This suggests that there is an initial conditioning of the catalyst through a reductive process which contributes extra current at low overpotentials. After conditioning, steady currents can be achieved.

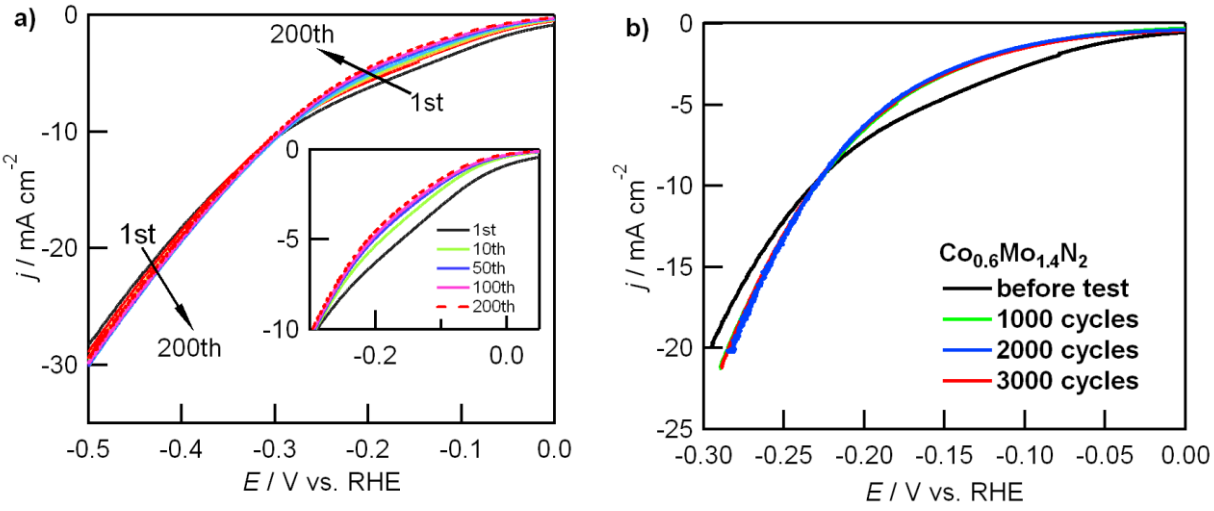

Figure 4.22 (a) Polarization curves for $Co_{0.6}Mo_{1.4}N_2$ without *iR* correction illustrating the conditioning of the electrode that occurs over the first 50 cycles. (b) Stability data for $Co_{0.6}Mo_{1.4}N_2$ measured over 3000 cycles (+0.2 to -0.3 V vs. RHE, 100 mV / s) on RDE in H_2-saturated 0.1 M $HClO_4$ with *iR* correction applied.

In addition to being active for HER under acidic conditions, $Co_{0.6}Mo_{1.4}N_2$ system also exhibits good activity for the HER under alkaline conditions (Fig. 4.23) though with less activity (shift to voltages ~0.1 V more negative). $Co_{0.6}Mo_{1.4}N_2$ exhibits superior activity over δ-MoN in both acidic and basic conditions, which further suggests that this activity is inherent to the

ternary phase. Both δ-MoN and $Co_{0.6}Mo_{1.4}N_2$ have a Tafel slope of about 80 mV/ decade, though the exchange current density of $Co_{0.6}Mo_{1.4}N_2$ (5.6×10^{-5} A/cm^2) is substantially higher than that of δ-MoN (1.1×10^{-6} A/cm^2).

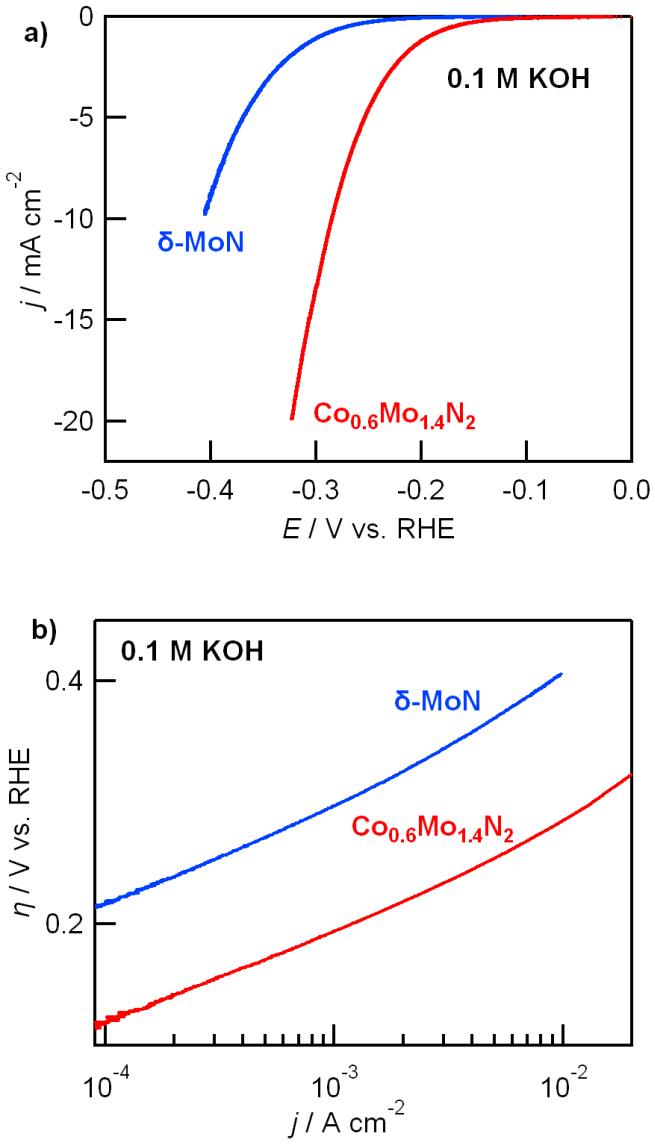

Figure 4.23 (a) Polarization curves for δ-MoN and $Co_{0.6}Mo_{1.4}N_2$ measured on a RDE (1600 rpm) in H_2-saturated 0.1 M KOH with *iR* correction. (b) Corresponding Tafel plot.

In both acidic and alkaline environments, the activity of ternary $Co_{0.6}Mo_{1.4}N_2$ is very much improved over that of binary δ-MoN. Although further experimental and theoretical studies will be required to obtain a full understanding of the origins of this enhancement, some hypotheses can be put forward by an examination of structural relationship between $Co_{0.6}Mo_{1.4}N_2$ and other Mo-containing HER catalysts. The HER activity observed for MoS_2, Mo_2C, MoB, δ-MoN and Ni-Mo-N suggest that the HER activity in $Co_{0.6}Mo_{1.4}N_2$ originates from surface Mo sites though likely without the severe geometry restrictions of MoS_2 (for which only edge sites are highly active[83]). Given the layered structure, it is expected that catalytically active Mo ions at the surface of $Co_{0.6}Mo_{1.4}N_2$ are coordinated by an interior triangle of three N ligands in a close-packed plane regardless of whether they originate in the trigonal planar or octahedral layers, and that Mo ions have flexibility in their exterior ligands (N^{3-}, NH^{2-}, O^{2-}, OH^-, H^-, H, *etc*.) whose number and charge may vary during the catalytic cycle. The electronic states of surface Mo species in $Co_{0.6}Mo_{1.4}N_2$ can be tuned by both the strain (smaller *a*-lattice than δ-MoN) and by the chemical bonding originating with the 3d transition metal Co, which may be expected to shift both the position and width of the *d*-electron manifold associated with the surface Mo ions. Since Co ions are readily dissolved under acidic conditions, it is also possible that the activity enhancement is geometric in nature, in which the Co ions in the mixed Co/Mo octahedral layers are removed upon exposure to acid resulting in a large number of highly exposed Mo ions being presented at the catalyst surface. Although synergistic effects due to the presence of both Co and Mo ions at the surface could be postulated, it seems unlikely that this would be responsible for the activity enhancement given the ease with which exposed Co ions can be dissolved in acid. In contrast, Co ions in bulk octahedral layers are protected from acid exposure by Mo ions present

within the octahedral layer and by covering Mo ions in neighboring trigonal prismatic layers, allowing good acid stability of bulk Co ions in this electrocatalysis.

4.4 Conclusions

A synthetic route for producing highly active nanostructured non-noble metal electrocatalysts ($Co_{0.6}Mo_{1.4}N_2$) for ORR and HER has been demonstrated. $Co_{0.6}Mo_{1.4}N_2$ was prepared by two-step annealing under flowing ammonia. First annealing at 750°C produced cubic Co_3Mo_3N which barely showed catalytic activity for ORR and HER. The following annealing of Co_3Mo_3N at 400°C produced hexagonal $Co_{0.6}Mo_{1.4}N_2$ with nanoscale morphology which exhibited enhanced ORR and HER performance over structural related δ-MoN. A current density of 10 mA/cm^2 at overpotential of 200 mV was achieved for $Co_{0.6}Mo_{1.4}N_2$, which illustrated its superior activity toward HER. $Co_{0.6}Mo_{1.4}N_2$ remained highly stable in acidic condition and no remarkable deterioration in performance was observed after 2000-3000 cycles.

This electrocatalyst is shown by neutron diffraction to have a four-layered mixed closed packed structure with alternating layers of octahedral sites (occupied by divalent Co and trivalent Mo) and trigonal prismatic sites (occupied by Mo with a valence larger than three but not more than four), and has not previously been reported to exhibit HER activity. It is expected that the layered nature of this structure allows the 3d transition metal to tune the electronic states of molybdenum at the catalyst surface without disrupting the catalytic activity and that alternative substitutions on the octahedral site of this structure type may lead to even better ORR and/or HER activity. It is desirable to further develop synthetic routes that give more control over particle size and/or access different Mo oxidation states in order to achieve optimal catalytic activity in this structure type, and to gain additional experimental and theoretical insights into the mechanism of HER activity in this structure type.

Chapter 5. Synthesis, Structural Characterization and Activity of Iron Tungsten Nitride

5.1 Introduction

Nitrides exhibit technologically useful properties for diverse applications such as catalysts, electronic and magnetic materials. Transition metal nitrides have high melting points, good hardness and corrosion resistance which are desired properties for catalysts. Binary nitrides have been widely studied. The ORR activity of W_2N/C was studied under half and single fuel cell conditions. W_2N displayed effective activity in sulfuric acid with a maximum power density of ~40 mW/cm^2 in a single cell PEMFC test. It also displayed stable activity for 80 hrs without deactivation.[45]

It is intriguing to explore ternary nitrides since they may have enhanced properties relative to binary nitrides. Iron based oxide and nitride compounds have been extensively investigated due to the natural abundance of iron. In general, moderate or low temperature synthesis is needed for the successful preparation of ternary nitrides. Ternary nitrides such as Li_3FeN_2 and Ca_6FeN_5 can be synthesized by reacting alkali or alkaline earth nitrides/amides with transition metal nitrides.[161] An alternative synthesis route is reacting ternary oxide precursors with ammonia. For example, $FeWN_2$ was synthesized by ammonolysis of $FeWO_4$ under NH_3 at 700 °C.[144] In previous chapter, ternary cobalt molybdenum nitride has shown superior catalytic activity. The structurally related iron tungsten nitride may have similar behavior. In this section, we report the synthesis, crystal structure, morphology and electronic structure of $FeWN_2$ based on diffraction (X-ray and neutron) and electron microscopy (SEM and TEM) measurements. Electrochemical measurements of $FeWN_2$ have been performed to test its capability for catalyzing oxygen reduction.

5.2 Experiment Section

5.2.1 Synthesis

An oxide precursor $FeWO_4$ was prepared by dropwise addition of 20 mL (0.165 M) aqueous $FeCl_2$ (Alfa Aesar, 99.7%) into a 10 mL (0.33 M) solution of $Na_2WO_4 \cdot 2H_2O$ (Alfa Aesar). The resulting brown suspension was stirred for 1 hour, filtered, washed, and dried at 120 °C overnight. $FeWN_2$ was synthesized by heating amorphous $FeWO_4$ at 700 °C (5 °C / min heating rate) for 15 hours under flowing ammonia (50 mL / min) inside a fused quartz tube. After 15 hours, the sample was cooled rapidly to room temperature.

5.2.2 Characterization

Laboratory X-ray powder diffraction patterns were obtained using a D8 Advance X-ray diffractometer (Bruker, AXS) with a Bragg-Brentano geometry using Cu K_α radiation (λ = 1.54056 Å). Scans were collected with a fixed divergence slit width of 0.6°, a 2θ range of 7 to 120°, a collection time of 1.5 s per step, a diffractometer radius of 300 mm, and a 192 channel LynxEye position sensitive detector. Synchrotron X-ray diffraction data were collected at the beamline X7B (λ = 0.3196 Å) and X14A (λ = 0.7788 Å) of the National Synchrotron Light Source (NSLS) at Brookhaven National Laboratory.

Time-of-flight (TOF) neutron diffraction measurements were performed on the nanoscale-ordered materials diffractometer (NOMAD) at the Spallation Neutron Source (SNS), Oak Ridge National Laboratory. About 100 mg of powder were loaded into a 2 mm diameter capillary, with data acquisition time of 100 min per sample for a total proton charge of 5.4×10^{12}. Data processing of both pair distribution function (PDF) and Bragg diffraction data was done using custom beamline-specific software coded in IDL. The TOPAS software package (Version 4.2, Bruker AXS) was used for Le Bail and Rietveld refinements of data.

Scanning electron microscopy (SEM) analysis was carried out on a JEOL 7600F high resolution microscope with capabilities for energy-dispersive X-ray spectroscopy (EDX). Transmission electron microscopy (TEM) was performed on a JEOL 1400 microscope operated at an accelerating voltage of 120 kV. Thermogravimetric analysis (TGA) was done on a Q5000IR system (TA instruments). TGA scans were run under flowing O_2 (25 mL / min) with ramp rates of 1 °C / min and held at 900 °C for 4 hours.

A PHI 3056 X-ray Photoelectron Spectroscopy (XPS) spectrometer with an Al source in a 2×10^{-10} Torr vacuum chamber was used to characterize sample surfaces. The instrument was calibrated before use with Au and Ag foils. Powder sample was pressed into In foil (Alfa Aesar), which was attached to the sample holder using carbon tape. High resolution scans were taken with a 5.85 eV pass energy, 0.05 eV energy step, and with 100 repeats to reduce instrument noise. Charging effects were compensated by shifting binding energies based on adventitious C 1s peak (284.8 eV). Peak fits and atomic surface concentration analysis was performed using PHI Multipack software.

5.2.3 Electrochemical Measurement

Catalyst inks for electrochemical testing were prepared by adding a mixture of 2 mg nitride sample and 2 mg carbon black (Vulcan XC72) to a solution of 500 μL Milli-Q water, 500 μL isopropyl alcohol (70% v/v, Aldrich), and 50 μL Nafion-117 (5 wt%, Aldrich), and then sonicating for 30 min to disperse the catalysts in the ink. Afterwards, 25μL of fresh catalyst ink was dropped onto a glassy carbon (GC) disk electrode (0.196 cm^2 geometrical area, Pine Research Instrument) and dried at room temperature. All electrochemical measurements were conducted in a three electrode conventional glass cell with an electrolyte solution of 0.1 M $HClO_4$. Ag/AgCl was used as reference electrode and Pt foil was used as auxiliary electrode.

Both cyclic voltammetry (CV) and rotating disc electrode (RDE) measurements were performed by sweeping from 0.05 to 1.0 V vs. RHE at a scan rate of 10 mV/s. CV data were recorded in acid solution saturated with either Ar or O_2 gas. RDE measurements were collected in O_2-saturated solution with a rotation speed of 1600 rpm.

5.3 Results and Discussion

5.3.1 Crystal Structure and Composition

Indexing of powder diffraction patterns (X-ray and neutron) for $FeWN_2$ gave a hexagonal unit cell of a = 2.8767 Å and c = 10.9458 Å (Fig. 5.1). On the basis of previous investigation, the space group $P6_3/mmc$ (No. 194) was chosen for refinements.[144] Careful analysis of the X-ray diffraction data revealed the formation of a small amount of iron nitride (Fe_3N) impurity. The impurity phase is generated at lower temperature than $FeWN_2$ and is dependent on the cooling rate as a slow cooling rate gives more impurity. Owing to the presence of impurity, iron tungsten nitride actually is iron deficient. Therefore, the site occupancy of iron was allowed to vary and the Fe occupancy was found to be between 0.80 and 0.84 for different data sets. The crystallographic parameters freely refined for $FeWN_2$ include the positions of nitrogen, the site occupancy of Fe and the thermal displacements for each atom. Refinements of synchrotron X-ray data did not provide resonable thermal displacement parameters due to the high absorption of tungsten and the insensitivity to light nitrogen atom. Rietveld refinement of neutron data was instead used to determine its crystal structure (Table 5.1). The refinement results show that nominal "$FeWN_2$" is structurally related to $(Co_{0.6}Mo_{0.4})MoN_2$ described in Chapter 4. In $(Co_{0.6}Mo_{0.4})MoN_2$, the 2*b* site is occupied by both Co and Mo. In "$FeWN_2$", the 2*b* site consists of Fe and vacancies while W is only located at the 2*a* site. The nitride formula can be written as $(Fe_{0.8}\square_{0.2})WN_2$, whereas $\square$ denotes vacancies. W atoms can potentially be mixed with Fe at the

same site if different synthesis protocols are used. It has been reported that $(Fe_{0.8}W_{0.2})WN_2$ is synthesized using $Fe_2(WO_4)_3$.[162] Nitrogen atoms exhibit anisotropic thermal displacements (ellipsoids are elongated along *c*-axis) which were also found for $(Co_{0.6}Mo_{0.4})MoN_2$.

The $(Fe_{0.8}\square_{0.2})WN_2$ structure contains layers of edge-shared octahedra (FeN_6) alternating with layers of edge-shared trigonal prisms (WN_6), where the octahedra and trigonal prisms are face-shared in *c*-direction. Iron tungsten nitride has an identical or similar stacking sequence with a number of other nitrides, including $(Fe_{0.8}W_{0.2})WN_2$, $(Fe_{0.8}Mo_{0.2})MoN_2$, $MnWN_2$, $LiMoN_2$, Ta_5N_6 and Nb_5N_6.[134,157,162]

Table 5.1 Refined atomic positions for $Fe_{0.8}WN_2$ based on neutron Rietveld refinement.

Formula	Space group	*a* (Å)	*c* (Å)	V(Å^3)	R_{wp}	R_p
$Fe_{0.8}WN_2$	$P6_3/mmc$	2.8767(2)	10.9458(8)	78.44	4.841	5.827

	Wycoff	*x*, *y*, *z*	Occupancy	U_{ij} or U_{iso}(Å^2)
W	2*a*	0, 0, 1/4	1.0	U_{iso} = 0.0023(2)
Fe	2*b*	0, 0, 0	0.799 (5)	U_{iso} = 0.0118(6)
N	4*f*	1/3, 2/3, 0.1326(1)	1.0	U_{11}= U_{22}= 0.0030(3) U_{33} = 0.018(1) U_{12} = 0.0015 U_{13}= U_{23}= 0

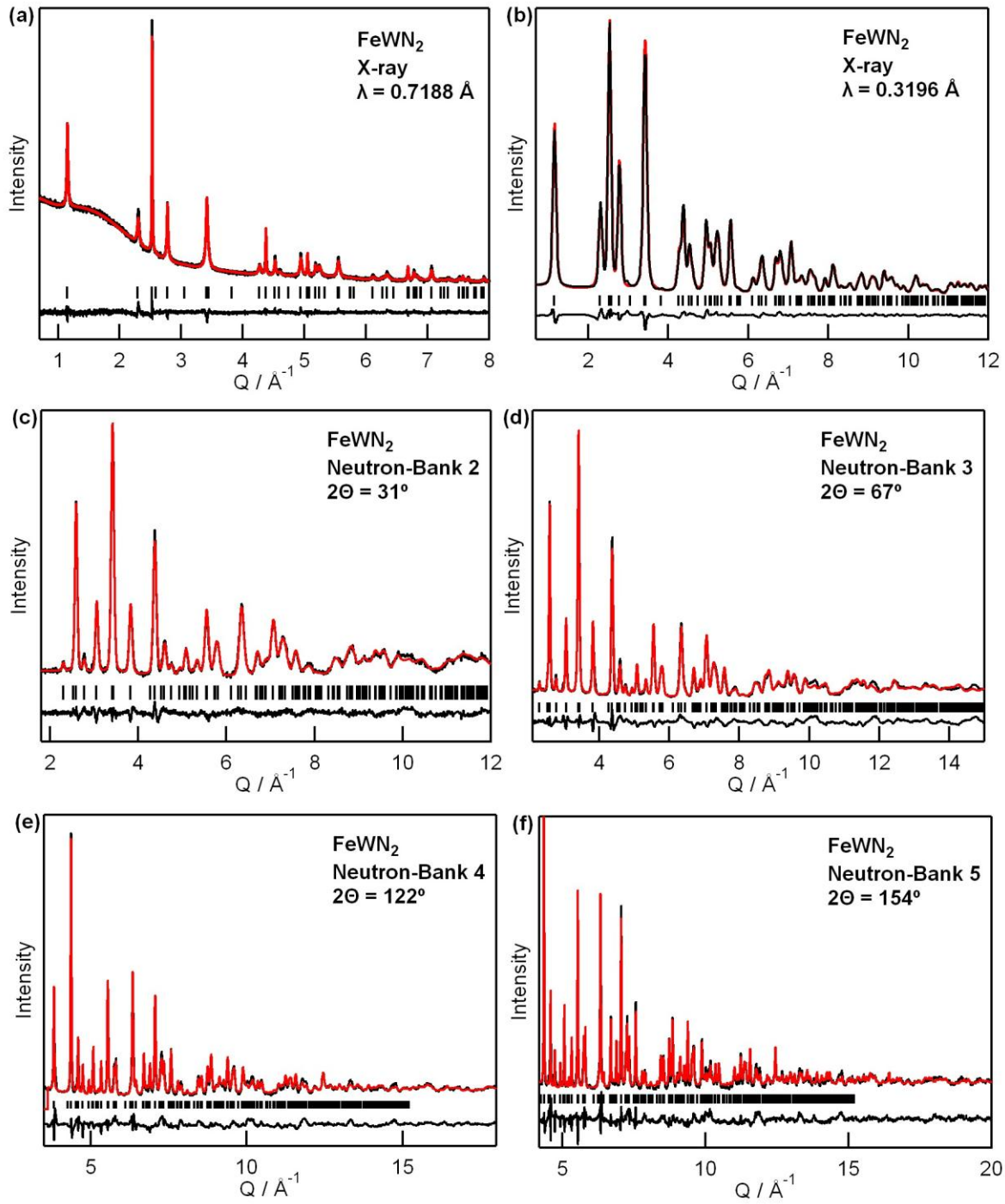

Figure 5.1 Rietveld refinement profiles for $Fe_{0.8}WN_2$ using X-ray and time of flight neutron data. Synchrotron X-ray data: (a) λ = 0.7188 Å; (b) λ = 0.3196 Å. Neutron data are ordered by increasing scattering angles: (c) bank 2-2θ=31°; (d) bank 3-2θ=67°; (e) bank 4-2θ=122°; (f) bank 5-2θ=154°. The black line indicates the observed data, the red line indicates the calculated data and the lower black line indicates the difference curve.

The composition of iron tungsten nitride can be indirectly examined by TGA analysis (Fig. 5.2). The nitride was decomposed in oxygen at 900 °C, where the oxidation products were identified as a mixture of Fe_2WO_6 and WO_3, both containing fully oxidized W^{6+}. No evaporation of WO_3 at high temperature (900 °C) was observed. The weight gain is 14.67 wt% which is slightly smaller than theoretical value (15.27 wt% for $Fe_{0.8}WN_2$ and 16.02 wt% for mixture of $Fe_{0.8}WN_2$ and Fe_3N). The smaller mass gain may indicate the presence of residual oxygen (1.17 wt%) in the bulk nitride. Small amounts of oxygen are also detected by EDX measurements.

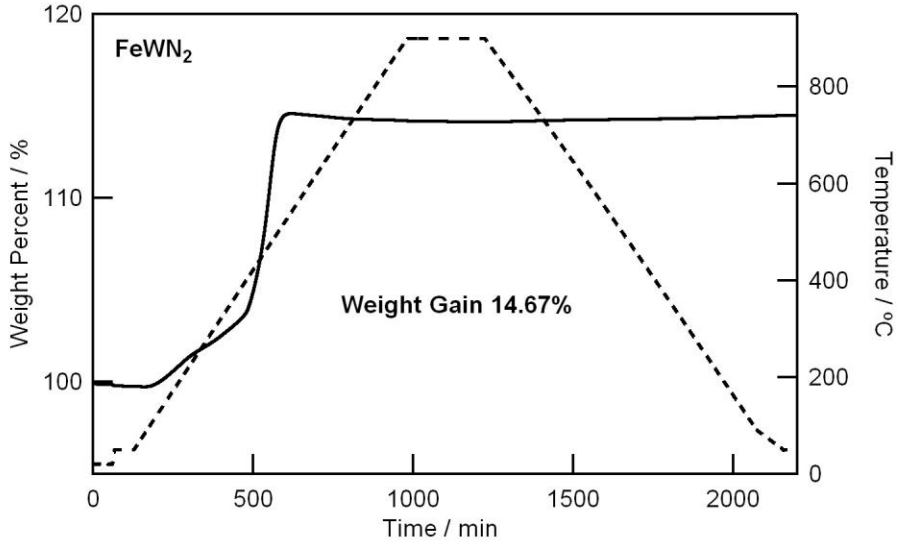

Figure 5.2 Thermogravimetric response of $Fe_{0.8}WN_2$ (with 4.5 wt% impurity Fe_3N) heated under oxygen from room temperature to 900 °C.

Local structure and atom-atom correlations were probed via pair distribution function analysis (Fig. 5.3). According to neutron PDF refinement result, the local structure at the atomic scale can be well described by the four-layered structure with alternating FeN_6 octahedral and WN_6 trigonal prismatic stacking sequences which is in good agreement with the average structure (Table 5.2). The occupancy of Fe is refined to be 0.81, confirming the presence of vacancies at the octahedral site. The fit of X-ray PDF data is not as good as the fit of neutron PDF data which may be due to the different percentages of impurity Fe_3N phase present in

samples measured by X-ray and neutron radiation respectively. Samples for X-ray PDF experiments contained more impurity phase which was confirmed by lower occupancy of Fe (~0.68) in nitrides.

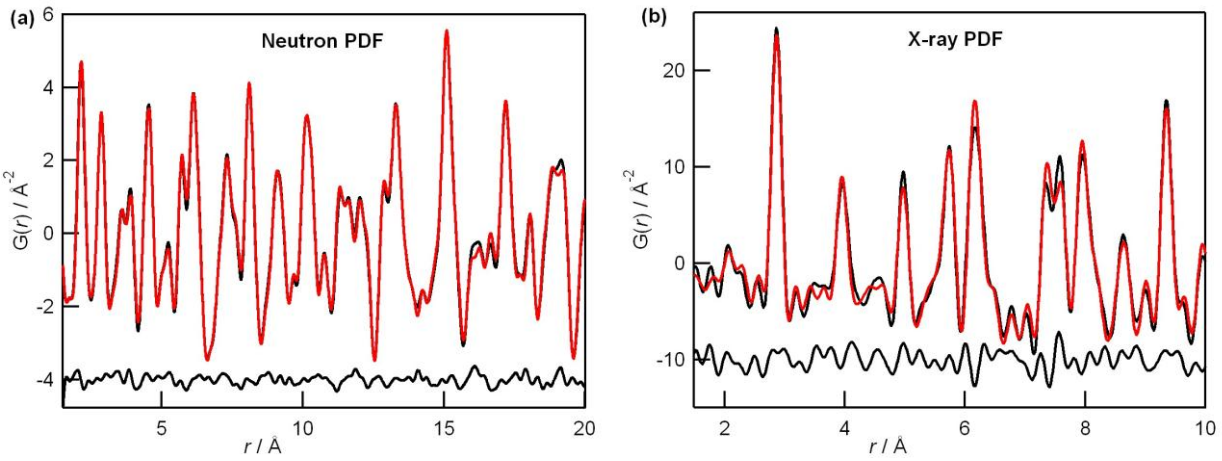

Figure 5.3 (a) Neutron PDF fit from r = 1.7 Å to 20 Å for $Fe_{0.8}WN_2$. (b) X-ray PDF fit from r = 1.7 Å to 10 Å for $Fe_{0.8}WN_2$.

Table 5.2 Refined atomic positions for $Fe_{0.8}WN_2$ based on neutron PDF (a = 2.8739 (8) Å and c = 10.928(4) Å).

Formula	Space group	a (Å)	c (Å)	V(Å^3)	R_{wp}
$Fe_{0.8}WN_2$	$P6_3/mmc$	2.8739(8)	10.928(4)	78.17	7.460

	Wycoff	x, y, z	Occupancy	U_{ij} or U_{iso}(Å^2)
W	2a	0, 0, 1/4	1.0	U_{iso} = 0.006(1)
Fe	2b	0, 0, 0	0.81(4)	U_{iso} = 0.013(2)
N	4f	1/3, 2/3, 0.1309(4)	1.0	U_{11}= U_{22}= 0.0091(5) U_{33} = 0.011(1) U_{12} = 0.0045 U_{13}= U_{23}= 0

PDF analysis can provide insights into the bond lengths and valence states in $Fe_{0.8}WN_2$. The bond length derived from neutron PDF is consistent with that from Rietveld refinement result of neutron data (Table 5.3). However, the bond lengths between transition metal and nitrogen (Fe-N and W-N) are very different from prior literature result ("$FeWN_2$", a = 2.8763 Å, a = 10.932 Å) while the metal-metal bonds are quite similar. The difference is mainly caused by the inaccurate nitrogen coordinate that is calculated from laboratory X-ray diffraction data. Compared to stoichiometric $FeWN_2$, the charge balance of non-stoichimetric $Fe_{0.8}WN_2$ can be maintained by oxidation of Fe/W or incorporation of protons. Herein, the shorter W-N distance means the oxidation of W whereas the longer Fe-N distance indicates the reduction of Fe.

Although it is challenging to verify the oxidation states in transition metal nitrides, a bond valence calculation can still be instructive to understand the metal-nitrogen bond distances and bond types. Using bond valence method described by Brese and O'Keefe,[163] the valence state of transition metals can be tabulated. The bond valence parameters used for the calclutions are 1.86 Å for Fe-N and 2.06 Å for W-N. According to the bond valence calculations, iron has a valence of +2.5 (Fe-N is 2.202 Å from neutron refinement, calculated Fe^{2+}-N is 2.27 Å and Fe^{3+}-N is 2.12 Å) while tungsten has a valence of +5.3 (W-N is 2.103 Å from neutron refinement, calculated W^{4+}-N is 2.21 Å, W^{5+}-N is 2.13 Å and W^{6+}-N is 2.06 Å). Based on the stoichiometry of the nitride, the oxidation state for W is +4 if Fe is +2.5 or the oxidation state of Fe is +0.875 if W is +5.3. This result indicates that the metal-nitrogen bond lengths are shorter than expected and the nitride is not fully ionic. Metal-nitrogen bonds in this ternary nitride have both ionic and covalent bonding characters. The interplanar N-N bond length is 2.603 Å, shorter than the sum of the ionic radii (2.92 Å), confirming the partially covalent *M*-N bonds.

Table 5.3 Refined bond distances for $Fe_{0.8}WN_2$ obtained through neutron diffraction data and through neutron PDF fitting results.

Bond	Distance (Å)		
	Neutron	Neutron PDF	"$FeWN_2$"[144]
W-N	2.103(1)	2.109(3)	2.156
Fe-N	2.202	2.191(3)	2.145
N-N	2.580(4)	2.603(9)	2.75
Fe-W	2.73644	2.732(1)	2.73301
Fe-Fe (W-W)	2.87668	2.8739(8)	2.87630

5.3.2 Surface Property

Information about the composition and oxidation states at the nitride surface was obtained from XPS measurements (Fig. 5.4). The overall XPS spectrum includes peaks from Fe, W, N and O. Although the bulk material is a nitride which only contains a small amount of oxygen, the surface of the nitride contains a much higher concentration of oxygen that is commonly observed for other nitride materials after air exposure. Two types of oxygen peaks are present. The dominant peak at 529.97 eV is from the oxidation of nitride phase and indicates the formation of Fe-O or W-O bond. The minor peaks at 531.54 eV and 534.05 eV are from Fe/W-$(OH)_x$ species presumably due to the adsorption of moisture from air.

The W spectra consist of two peaks, the W $4f_{7/2}$ peak which is at lower binding energy and the W $4f_{5/2}$ peak, which is at higher binding energy. The separation between these two peaks is about 2 eV. The binding energy of W^{4+} is between 32.0 eV and 33.4 eV while W^{6+} is around 36 eV. Based on these prior assignments, most of the W is reduced and in a state close to 4+ (85%), however there is still a small concentration of W^{6+} in the top few nanometers of the

surface. The Fe spectra demonstrate that $Fe_{0.8}WN_2$ surface contains about 63% Fe^{3+} and 37% Fe^{2+}. Relative to tungsten, it is much easier for iron to be oxidized to its highest oxidation state. The N 1s spectrum indicates that nitrogen species are still on or near the surface even though the surface contains oxygen. Similar to other nitrides, both Fe/W-N and N-H species are present. The majority of nitrogen species (98%) is ascribed to metal-nitrogen bonding, consistent with the bulk phase. Only a small quantity of N-H species is induced from the NH_3 reaction, unlike Co-Mo-O-N and $Co_{0.6}Mo_{1.4}N_2$.

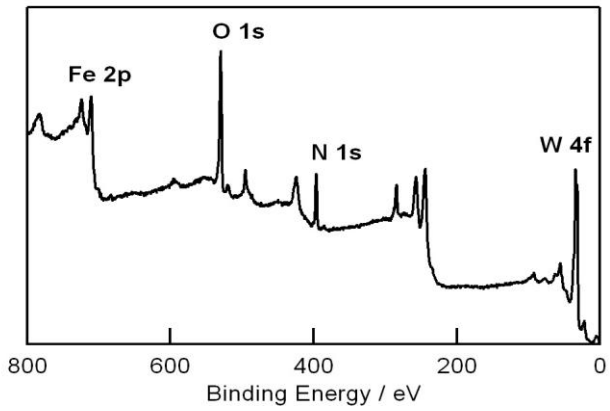

Figure 5.4 Overall XPS spectrum of $Fe_{0.8}WN_2$ showing Fe 2p, O 1s, N 1s and W 4f spectra.

Table 5.4 XPS analysis of $Fe_{0.8}WN_2$.

Sample	W^{4+}		W^{6+}			Fe $2p_{3/2}$			
	$4f_{7/2}$	$4f_{5/2}$	$4f_{7/2}$	$4f_{5/2}$	$5p_{3/2}$	Fe^{2+}	Fe^{3+}	Fe^{2+}-OH	Fe^{3+}-OH
$Fe_{0.8}WN_2$	32.18	34.31	35.49	37.26	39.5	708.07	710.45	712.13	713.80
%	84.7		15.3			17.0	52.0	20.3	10.7

Sample	N 1s			O 1s		
	W/Fe-N		N-H	Fe/W-O	Fe/W-OH	Fe/W-$(OH)_2$
$Fe_{0.8}WN_2$	396.72	398.19	399.66	529.97	531.54	534.05
%	88.3	9.7	2.0	68.3	23.3	8.4

5.3.3 Morphology

Changes of both morphology and particle size occur during ammonolysis (Fig. 5.5). Amorphous $FeWO_4$ has an average particle size of around 100 nm. After ammonia treatment, the resulting $Fe_{0.8}WN_2$ contains plate-like crystals ~1 μm across and ~ 50 nm in thickness. Some crystallites have a hexagonal shape (Fig. 5.6), indicating the nitrogen layers are parallel to the hexagonal surface of the particle. EDX spectra show a nitrogen peak, confirming the formation of the nitride phase. The ratio of Fe/W was semi-quantitatively determined by EDX. In certain areas, Fe/W is ~ 0.83 which corresponds to $Fe_{0.8}WN_2$ and it is ~1 in other areas, which corresponds to a combination of $Fe_{0.8}WN_2$ and Fe_3N.

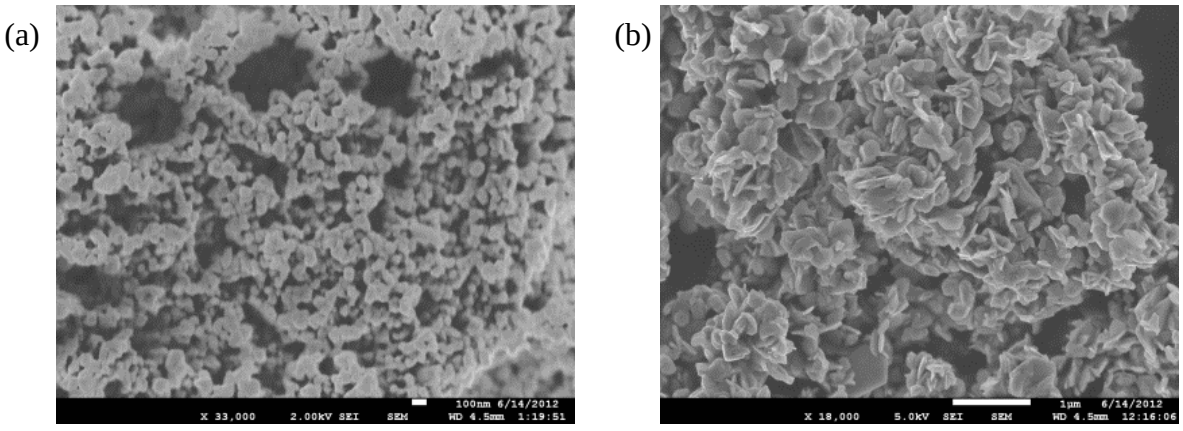

Figure 5.5 SEM image of (a) Amorphous $FeWO_4$ (scale bar: 100 nm) and (b) $Fe_{0.8}WN_2$ (scale bar: 1 μm).

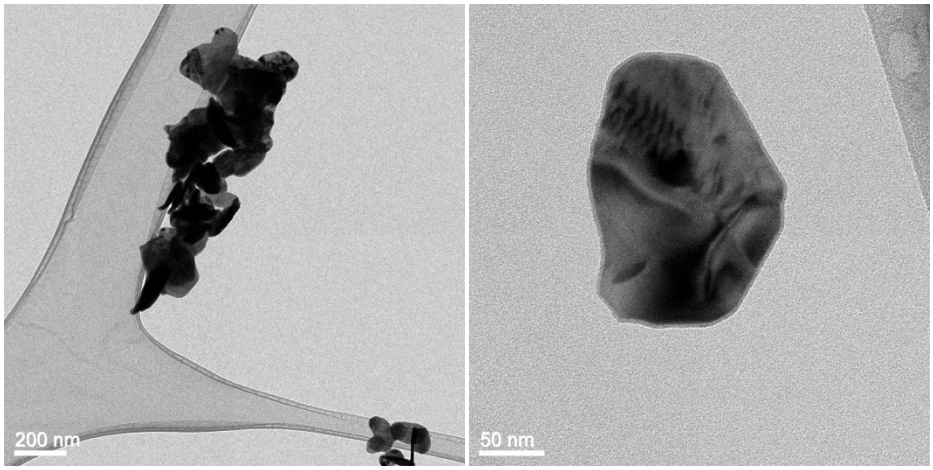

Figure 5.6 TEM images of $Fe_{0.8}WN_2$.

5.3.4 Density of States Calculations

The electronic structure of $FeWN_2$ is shown in Fig. 5.7. It is found that the density of states is different from reported calculation which investigated the electronic structures of ferromagnetic and antiferromagnetic $FeWN_2$ respectively.[164] Here, the calculation does not consider the magnetic moment of Fe in $FeWN_2$ that may cause the difference. The TDOS of $FeWN_2$ suggest that the nitride is metallic, though this result can not be considered robust since spin polarizations are not utilized. Similar to binary molybdenum nitrides in Chapter 3, the lower region is mainly occupied by N 2s states. The N 2p orbitals are more strongly hybridized with W orbitals rather than Fe 3d orbitals. The hybridization indicates that W-N bond is more covalent and Fe-N bond is more ionic. Moreover, the W d orbitals are more delocalized while the Fe d orbitals are more localized and centralized near Fermi level (E_F).

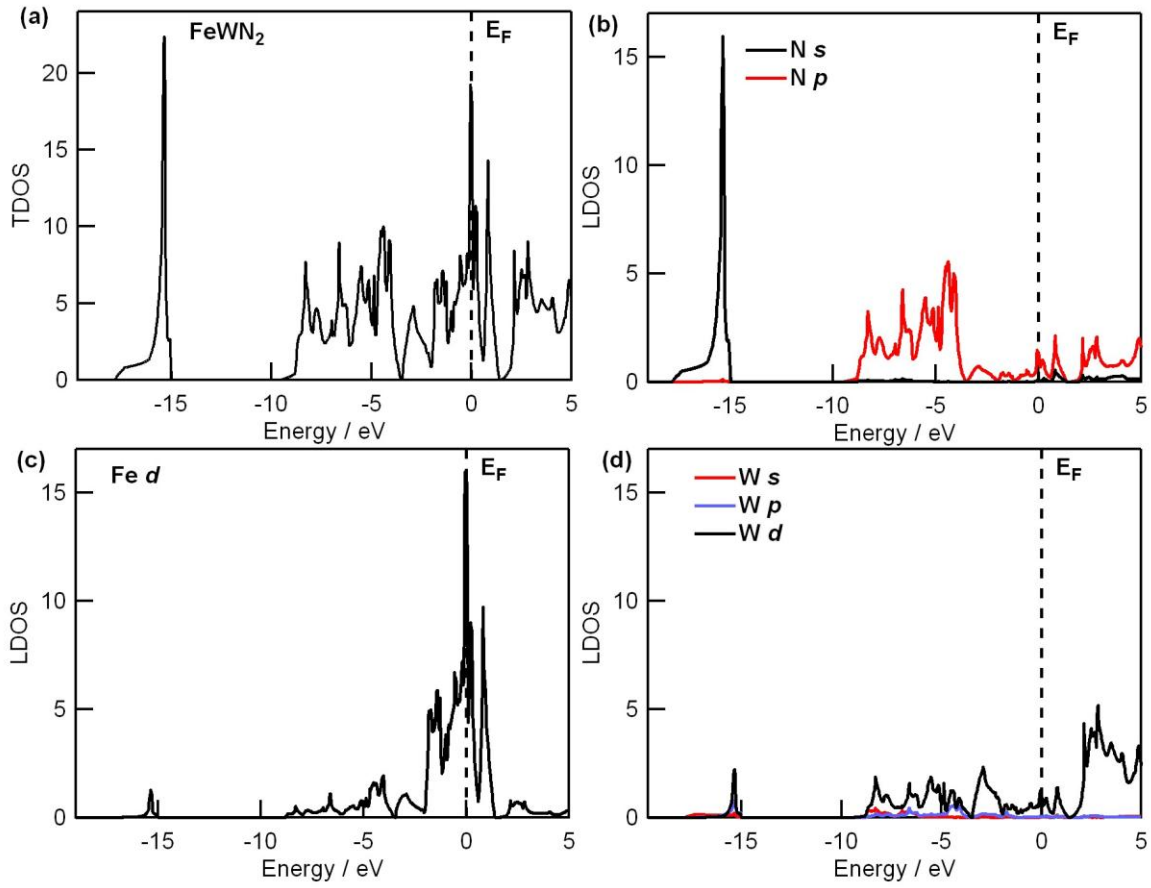

Figure 5.7 Calculated total density of states for $FeWN_2$ and the local density of states of N, Fe and W.

5.3.5 Electrochemical Performance

As described in Chapter 3 and Chapter 4, molybdenum nitrides (δ-MoN, Mo_5N_6 and $Co_{0.6}Mo_{1.4}N_2$) with a layered hexagonal structure have displayed an enhanced catalytic activity toward ORR. The ORR activity of $Fe_{0.8}WN_2$ was therefore measured to identify whether the W-based nitride with similar structural type exhibits good activity. However, $Fe_{0.8}WN_2$ shows a much lower ORR activity than $FeMoN_2$ and other Mo-based nitrides in acid electrolytes. It should be noted that nominal "$FeMoN_2$" is actually Mo rich due to the formation of FeN_x as a minor phase in the synthesis. Hence, both "$FeMoN_2$" and $Fe_{0.8}WN_2$ contain Fe deficiency and have four-layered hexagonal structures. One possible reason for the poor performance is that

$Fe_{0.8}WN_2$ has a large particle size around 1 μm, rather than the average particle size of $FeMoN_2$ (~ 100 nm). Besides the effect of particle size, chemical substitution on trigonal prismatic site is correlated with the catalytic property, suggesting Mo plays a critical role in activity. The energy barrier to catalyze oxygen reaction is probably lower for Mo-containing nitrides than that for W-containing nitrides. It is concluded that molybdenum nitrides are better potential catalyst candidates for ORR than tungsten nitrides. Although tungsten nitride can not be used as catalyst directly, it might be utilized as supporting substrates for noble metals in fuel cells. Previously, studies have compared the activity and stability of Pt supported on tungsten carbide with that of Pt supported on carbon black. An activity ten times larger on Pt-W_2C/C than on Pt/C was observed for ORR in alkaline. Tungsten carbide is more stable than the carbon aganist thermal oxidation and electrochemical oxidation.[165] Since transition metal nitrides have similar physicochemical properties to transition metal carbides, $Fe_{0.8}WN_2$ may be a good candidate for use as a fuel cell catalyst support.

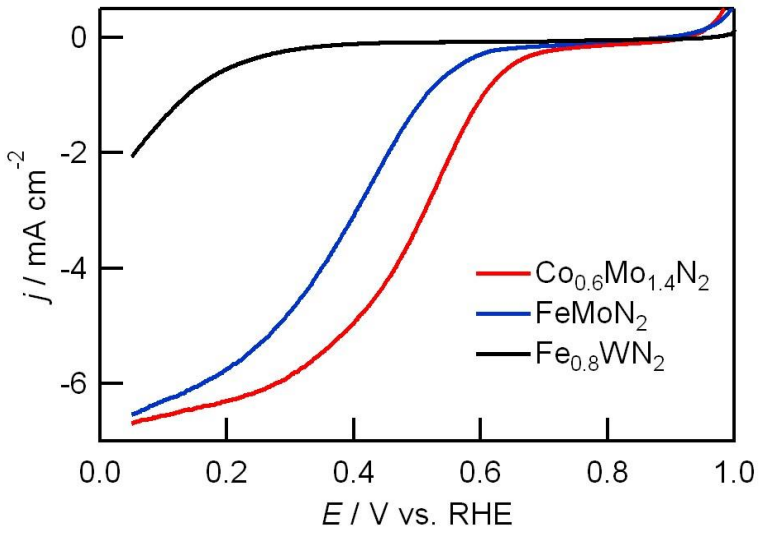

Figure 5.8 RDE curves (1600 rpm) of $Fe_{0.8}WN_2$, $FeMoN_2$ and $Co_{0.6}Mo_{1.4}N_2$ in O_2-saturated 0.1 M $HClO_4$.

5.4 Conclusions

Non-stoichiometric $Fe_{0.8}WN_2$ can be synthesized by a conventional ammonolysis process using the oxide precursor $FeWO_4$. $Fe_{0.8}WN_2$ has a four-layered structure of alternating WN_6 prismatic layers and FeN_6 octahedral layers. Iron vacancies are present on the octahedral site. Both bond valence analysis and density of states calculations suggest that ionic and covalent bond interactions are present in $Fe_{0.8}WN_2$ whereas Fe-N is more ionic and W-N is more covalent. XPS measurement of the sample surface suggests that W has a valence of 4+ and Fe has a valence of 3+ on the surface. This nitride does not show significant ORR activity in acidic solution due to its large particle size and inactive tungsten ions. However, it may be utilized as a supporting material of noble metals for catalysis applications.

Chapter 6. Conclusions

Non-nobel metal based transition metal nitrides and oxynitrides represent promising candidates for ORR and HER electrocatalysts with good performance. Although investigations of non-noble metal catalysts for ORR are growing, research interests are focused on developing transition metal macrocycles and there are limited studies on transition metal nitrides and oxynitrides. Therefore, we are motivated by the lack of fundamental studies of the structures, physicochemical properties and intrinsic electrochemical properties of nitrides and oxynitrides and we have sought to explore the structure-performance correlations. In this dissertation, we have focused on designing molybdenum based oxynitrides and nitrides with the objective of achieving highly effective catalysts. We have employed low-temperature ammonolysis synthesis method under ambient conditions in order to approach nanoparticles suitable for catalysis. The crystal structures and physicochemical properties (composition, morphology, valence state, bond length *etc*.) have been comprehensively studied. In terms of structures, we have utilized synchrotron X-ray diffraction, TOF neutron diffraction and pair distribution ananlysis to determine the crystal structure of nitrides (*eg*. position and displacements of nitrogen) more accurately. Factors linked to the electrochemical activity and durability have been postulated and investigated. With the in-depth understanding of structure-property relationships in electrocatalysis, it is anticipated that improved electrochemical performance of optimized molybdenum nitrides and oxynitrides can be achieved in the future.

In Chapter 2, carbon supported cobalt molybdenum oxynitrides with a rock salt structure were synthesized by the medium temperature ammonolysis of soluble metal precursors dispersed in aqueous solution. These oxynitrides were found to be active electrocatalysts for ORR. The effect of sintering temperature and composition on ORR activities was investigated, with the

highest activities observed in both acid and alkaline solutions for compounds synthesized at 823 K with equimolar amounts of Co and Mo ($Co_{0.5}Mo_{0.5}O_yN_z$/CB). Its onset potential reaches 0.645 V vs. RHE in acid and 0.918 V vs. RHE in alkaline. Koutechy-Levich analysis indicates that ORR occurs primarily through a four-electron process for low overpotentials in alkaline electrolytes. The oxynitride also retains activity after long-term durability tests in both electrolytes. Structural, spectroscopic and morphological studies were carried out using both bulk and atomic-scale probes. Although some cobalt metal is invariably formed during the synthesis, ionic cobalt is demonstrated to be substituted into the rock-salt structure to form a bimetallic cobalt molybdenum oxynitride with nanoscale texture that is catalytically active for the oxygen reduction.[107]

In Chapter 3-4, binary and ternary molybdenum nitrides have been investigated for ORR catalysis. δ-MoN and Mo_5N_6 with a hexagonal structure showed a enhanced activity than Mo_2N with a rock salt fcc structure which indicates structural factor plays an important role in determining its ORR performance. A two-step solid state reaction for preparing cobalt molybdenum nitride with a nanoscale morphology has been used to produce a highly active and stable electrocatalyst for the ORR and HER under acidic conditions. It exhibits higher ORR and HER activity over that of δ-MoN. Neutron powder diffraction and pair distribution function studies have been used to overcome the insensitivity of X-ray diffraction data to different transition metal nitride structural polytypes, and show that this cobalt molybdenum nitride crystallizes in space group $P6_3/mmc$ with lattice parameters of a = 2.85176(2) Å and c = 10.9862(3) Å and a formula of $Co_{0.6}Mo_{1.4}N_2$. This space group results from the four-layered stacking sequence of a mixed close packed structure with alternating layers of transition metals in octahedral and trigonal prismatic coordination, and is a structure type for which HER activity

has not previously been reported. Based on the accurate bond distances obtained from time-of-flight neutron diffraction data, it is determined that the octahedral sites contain a mixture of divalent Co and trivalent Mo, while the trigonal prismatic sites contain Mo in a higher oxidation state. X-ray photoelectron spectroscopy studies confirm that at the sample surface, nitrogen is present and N-H moieties are abundant. It is expected that the layered structure allows 3d transition metals to tune the electronic states of molybdenum at the catalyst surface and that alternative substitutions on the octahedral site may lead to a better HER activity. Further modifications such as decreasing particle size and tuning the oxidation states of Mo will be performed to achieve an optimal catalytic activity in this structure type.[108]

Besides molybdenum nitrides, we have also studied tungsten nitrides. In Chapter 5, non-stoichiometric $Fe_{0.8}WN_2$ consists of a four layered structure with alternating trigonal prismatic layers (occupied by W) and octahedral layers (occupied by Fe and vacancies), which is similar to $Co_{0.6}Mo_{1.4}N_2$. W-N bond interaction is more covalent while Fe-N bond interaction is more ionic, which is consistent with the presence of Fe deficiency. The electrochemical measurement result indicates that $Fe_{0.8}WN_2$ is not suitable for ORR catalysis. This nitride might be used as a substrate of noble metals for catalysis.

Molybdenum containing oxynitrides and nitrides need futher development in order to achieve an optimal compound for cathode catalysis. Firstly, modified synthetic routes are required to control the particle size and homogeneity. The NH_3 flow direction in ammonolysis described in this dissertation is horizontal which causes powder sample inhomogeneity. Instead, the vertical flow direction is preferred by rotating the horizontal set of tube furnce 90°. Flowing ammonia in the vertical setting will pass through and react with precursor sample more evenly and lead to a more homogeneous products. Besides using ammonia, other nitrogen sources can

be used to provide nitrogen species which may improve its homogeneity. For example, nitrogen agents such as urea ($CO(NH_2)_2$) and biuret ($H_2NCONHOCNH_2$) can be mixed with oxide precursors in specific molar ratio. The mixture will be heated under an inert atmosphere (Ar or N_2). During the heating, nitrogen agents will be decomposed at elevated temperature and provide nitrogen species that will react with the precursor and generate oxynitride or nitride phase. Besides preparing powder samples, it is intriguing to prepare thin film samples using chemical vapor deposition (CVD) or physical vapor deposition (PVD) techniques.

Secondly, the cubic rock salt structure and hexagonal layered structure allow the incorporation of 3d transition metals to tune the valence state and electronic structure of Mo in the compounds. It is viable to dope other active transition metal elements such as Cr, Mn, Fe, Ni and Cu into the cubic oxynitrides and hexagonal nitrides. The substituting effet will be evaluated by comparing their catalytic activity toward ORR and HER with that of Co doped sample. Diffraction and spectroscopy measurements will be performed to explore the changes of crystal structures (Mo coordinations) and physical properties (morphology, oxidation state, *etc*.) in the bulk and on the surface. A thorough understanding of inherent structure, electronic structure and intrinsic catalytic activity will help to further optimize the nitrides.

Thirdly, *ex situ* experiments are typically used to measure the structure and property before and after electrochemical tests. However, *ex situ* techniques are limited in their ability to probe the alternations of structure and property during the electrochemical catalysis process. Therefore, *in situ* characterizations will be applied to better understand factors influencing the activity. For instance, *in situ* XAS can be used to examine the change of bulk oxidation state and *in situ* XPS can be used to meaure the change of composition, valence state and species near the

surface. These *in situ* experiments will provide insights to further improve its activity and stability.

Finally, theoretical calculations such as DFT have been intensively used to elucidate factors linked to the performance. However, there is limited theoretical work on transition metal nitrides and oxynitrides. It is intriguing to explore the role of electronic structure of Mo (substituting effect) with catalytic activity using DFT calculations. The effective DFT approaches together with results from *ex situ* and *in situ* experiments should provide a comprehensive framework for designing optimal catalyst with enhanced activity and stability toward ORR and HER.

References

(1) Etacheri, V.; Marom, R.; Elazari, R.; Salitra, G.; Aurbach, D. *Energy & Environmental Science* **2011**, *4*, 3243.

(2) Black, R.; Adams, B.; Nazar, L. F. *Advanced Energy Materials* **2012**, *2*, 801.

(3) Girishkumar, G.; McCloskey, B.; Luntz, A. C.; Swanson, S.; Wilcke, W. *The Journal of Physical Chemistry Letters* **2010**, *1*, 2193.

(4) Winter, M.; Brodd, R. J. *Chemical Reviews* **2004**, *104*, 4245.

(5) Whittingham, M. S.; Zawodzinski, T. *Chemical Reviews* **2004**, *104*, 4243.

(6) Atkins, P. P. W.; De Paula, J. *Atkins' Physical Chemistry*; Oxford University Press, Incorporated, 2002.

(7) Hoogers, G. *Fuel cell technology handbook*; CRC press, 2002.

(8) Larminie, J.; Dicks, A.; McDonald, M. S. *Fuel cell systems explained*; Wiley New York, 2003; Vol. 2.

(9) Bockris, J. O. M.; Reddy, A. K.; Electrochemistry, M. *Electrodics in Chemistry, Engineering, Biology, and Environmental Science*; Springer, 2000.

(10) Damjanovic, A. *Modern aspects of electrochemistry* **1969**, 369.

(11) Tarasevich, M.; Sadkowski, A.; Yeager, E. *Oxygen electrochemistry*; Springer, 1983.

(12) Damjanovic, A. In *Electrochemistry in Transition*; Springer: 1992, p 107.

(13) Adzic, R. *Recent advances in the kinetics of oxygen reduction*, Brookhaven National Lab., Upton, NY (United States), 1996.

(14) Griffith, J. *Proceedings of the Royal Society of London. Series A. Mathematical and Physical Sciences* **1956**, *235*, 23.

(15) Pauling, L. *Nature* **1964**, *203*, 182.

(16) Yeager, E. *Journal of The Electrochemical Society* **1981**, *128*, 160C.

(17) Zagal, J. H. *Coordination Chemistry Reviews* **1992**, *119*, 89.

(18) Gasteiger, H. A.; Kocha, S. S.; Sompalli, B.; Wagner, F. T. *Applied Catalysis B: Environmental* **2005**, *56*, 9.

(19) Mayrhofer, K. J. J.; Blizanac, B. B.; Arenz, M.; Stamenkovic, V. R.; Ross, P. N.; Markovic, N. M. *The Journal of Physical Chemistry B* **2005**, *109*, 14433.

(20) Mukherjee, S.; Srinivasan, S.; Soriaga, M. P. *J. Electrochem. Soc* **1995**, *142*, 1409.

(21) Bing, Y.; Liu, H.; Zhang, L.; Ghosh, D.; Zhang, J. *Chemical Society Reviews* **2010**, *39*, 2184.

(22) Stamenkovic, V.; Schmidt, T.; Ross, P.; Markovic, N. *The Journal of Physical Chemistry B* **2002**, *106*, 11970.

(23) Stamenkovic, V. R.; Mun, B. S.; Arenz, M.; Mayrhofer, K. J.; Lucas, C. A.; Wang, G.; Ross, P. N.; Markovic, N. M. *Nature materials* **2007**, *6*, 241.

(24) Stamenkovic, V. R.; Mun, B. S.; Mayrhofer, K. J.; Ross, P. N.; Markovic, N. M. *J. Am. Chem. Soc.* **2006**, *128*, 8813.

(25) Adzic, R. R.; Zhang, J.; Sasaki, K.; Vukmirovic, M. B.; Shao, M.; Wang, J.; Nilekar, A. U.; Mavrikakis, M.; Valerio, J.; Uribe, F. *Topics in Catalysis* **2007**, *46*, 249.

(26) Wang, J. X.; Inada, H.; Wu, L.; Zhu, Y.; Choi, Y.; Liu, P.; Zhou, W.-P.; Adzic, R. R. *J. Am. Chem. Soc.* **2009**, *131*, 17298.

(27) Chen, Z.; Higgins, D.; Yu, A.; Zhang, L.; Zhang, J. *Energy & Environmental Science* **2011**, *4*, 3167.

(28) Ohms, D.; Herzog, S.; Franke, R.; Neumann, V.; Wiesener, K.; Gamburcev, S.; Kaisheva, A.; Iliev, I. *J. Power Sources* **1992**, *38*, 327.

(29) Wiesener, K.; Ohms, D.; Neumann, V.; Franke, R. *Materials Chemistry and physics* **1989**, *22*, 457.

(30) Van Veen, J. R.; van Baar, J. F.; Kroese, K. J. *Journal of the Chemical Society, Faraday Transactions 1: Physical Chemistry in Condensed Phases* **1981**, *77*, 2827.

(31) Jiang, R.; Chu, D. *Journal of The Electrochemical Society* **2000**, *147*, 4605.

(32) Li, S.; Zhang, L.; Kim, J.; Pan, M.; Shi, Z.; Zhang, J. *Electrochimica Acta* **2010**, *55*, 7346.

(33) Wu, G.; Chen, Z.; Artyushkova, K.; Garzon, F. H.; Zelenay, P. *Ecs Transactions* **2008**, *16*, 159.

(34) Zelenay, P. In *2010 Hydrogen program annual merit review and peer evaluation meeting, Washington, DC* 2010.

(35) Wu, G.; Artyushkova, K.; Ferrandon, M.; Kropf, A. J.; Myers, D.; Zelenay, P. *Ecs Transactions* **2009**, *25*, 1299.

(36) Li, X.; Liu, C.; Xing, W.; Lu, T. *J. Power Sources* **2009**, *193*, 470.

(37) Lefèvre, M.; Dodelet, J. P.; Bertrand, P. *The Journal of Physical Chemistry B* **2002**, *106*, 8705.

(38) Li, S.; Zhang, L.; Liu, H.; Pan, M.; Zan, L.; Zhang, J. *Electrochimica Acta* **2010**, *55*, 4403.

(39) Charreteur, F.; Jaouen, F.; Ruggeri, S.; Dodelet, J.-P. *Electrochimica Acta* **2008**, *53*, 2925.

(40) Rao, C. V.; Cabrera, C. R.; Ishikawa, Y. *The Journal of Physical Chemistry Letters* **2010**, *1*, 2622.

(41) Wang, X.; Lee, J. S.; Zhu, Q.; Liu, J.; Wang, Y.; Dai, S. *Chemistry of Materials* **2010**, *22*, 2178.

(42) Zen, J.-M.; Manoharan, R.; Goodenough, J. *J. Appl. Electrochem.* **1992**, *22*, 140.

(43) Beyerlein, R.; Horowitz, H.; Longo, J. *Journal of Solid State Chemistry* **1988**, *72*, 2.

(44) Raghuveer, V.; Kumar, K.; Viswanathan, B. *Indian Jounal of Engineering and Materials Sciences* **2002**, *9*, 137.

(45) Zhong, H.; Zhang, H.; Liang, Y.; Zhang, J.; Wang, M.; Wang, X. *J. Power Sources* **2007**, *164*, 572.

(46) Zhong, H.; Zhang, H.; Liu, G.; Liang, Y.; Hu, J.; Yi, B. *Electrochem. Commun.* **2006**, *8*, 707.

(47) Asahi, R.; Morikawa, T.; Ohwaki, T.; Aoki, K.; Taga, Y. *Science* **2001**, *293*, 269.

(48) Ishihara, A.; Lee, K.; Doi, S.; Mitsushima, S.; Kamiya, N.; Hara, M.; Domen, K.; Fukuda, K.; Ota, K. *Electrochem. Solid State Lett.* **2005**, *8*, A201.

(49) Liu, G.; Zhang, H. M.; Wang, M. R.; Zhong, H. X.; Chen, J. *J. Power Sources* **2007**, *172*, 503.

(50) Maekawa, Y.; Ishihara, A.; Kim, J.-H.; Mitsushima, S.; Ota, K.-i. *Electrochemical and Solid-State Letters* **2008**, *11*, B109.

(51) Houston, J.; Laramore, G.; Park, R. L. *Science* **1974**, *185*, 258.

(52) Yang, R.; Bonakdarpour, A.; Dhan, J. R. *Journal of The Electrochemical Society* **2007**, *154*, B1.

(53) McIntyre, D.; Vossen, A.; Wilde, J.; Burstein, G. *J. Power Sources* **2002**, *108*, 1.

(54) Yang, R.; Stevens, K.; Dahn, J. R. *Journal of The Electrochemical Society* **2008**, *155*, B79.

(55) Easton, E. B.; Bonakdarpour, A.; Yang, R.; Stevens, D. A.; Dahn, J. R. *Journal of The Electrochemical Society* **2008**, *155*, B547.

(56) Nam, K. D.; Ishihara, A.; Matsuzawa, K.; Mitsushima, S.; Ota, K.-i. *Electrochemical and Solid-State Letters* **2009**, *12*, B158.

(57) Ohgi, Y.; Ishihara, A.; Matsuzawa, K.; Mitsushima, S.; Ota, K. *Journal of The Electrochemical Society* **2010**, *157*, B885.

(58) Ohgi, Y.; Ishihara, A.; Matsuzawa, K.; Mitsushima, S.; Ota, K.-i. *Ecs Transactions* **2009**, *25*, 129.

(59) Ota, K.-i.; Mitsushima, S.; Ishihara, A. *Ecs Transactions* **2008**, *13*, 161.

(60) Lu, S.; Pan, J.; Huang, A.; Zhuang, L.; Lu, J. *Proceedings of the National Academy of Sciences* **2008**, *105*, 20611.

(61) Anastasijević, N.; Dimitrijević, Z.; Adžić, R. *Journal of Electroanalytical Chemistry and Interfacial Electrochemistry* **1986**, *199*, 351.

(62) Ramesh, K.; Shukla, A. *J. Power Sources* **1987**, *19*, 279.

(63) Yang, Y.-F.; Zhou, Y.-H.; Cha, C.-S. *Electrochimica Acta* **1995**, *40*, 2579.

(64) Pattabiraman, R. *Applied Catalysis A: General* **1997**, *153*, 9.

(65) Chatenet, M.; Aurousseau, M.; Durand, R.; Andolfatto, F. *Journal of The Electrochemical Society* **2003**, *150*, D47.

(66) Lima, F. H.; Ticianelli, E. A. *Electrochimica Acta* **2004**, *49*, 4091.

(67) Bidault, F.; Brett, D.; Middleton, P.; Brandon, N. *J. Power Sources* **2009**, *187*, 39.

(68) Chatenet, M.; Géniès-Bultel, L.; Aurousseau, M.; Durand, R.; Andolfatto, F. *J. Appl. Electrochem.* **2002**, *32*, 1131.

(69) Mao, L.; Zhang, D.; Sotomura, T.; Nakatsu, K.; Koshiba, N.; Ohsaka, T. *Electrochimica Acta* **2003**, *48*, 1015.

(70) Lima, F. H.; Calegaro, M. L.; Ticianelli, E. A. *Electrochimica Acta* **2007**, *52*, 3732.

(71) Cheng, F.; Su, Y.; Liang, J.; Tao, Z.; Chen, J. *Chemistry of Materials* **2009**, *22*, 898.

(72) King, W.; Tseung, A. *Electrochimica Acta* **1974**, *19*, 493.

(73) Guerrini, E.; Piozzini, M.; Castelli, A.; Colombo, A.; Trasatti, S. *J. Solid State Electrochem.* **2008**, *12*, 363.

(74) Tseung, A.; Yeung, K. *Journal of The Electrochemical Society* **1978**, *125*, 1003.

(75) Restovic, A.; Rios, E.; Barbato, S.; Ortiz, J.; Gautier, J. *Journal of Electroanalytical Chemistry* **2002**, *522*, 141.

(76) Liang, Y.; Li, Y.; Wang, H.; Zhou, J.; Wang, J.; Regier, T.; Dai, H. *Nature materials* **2011**, *10*, 780.

(77) Yuasa, M.; Sakai, G.; Shimanoe, K.; Teraoka, Y.; Yamazoe, N. *Journal of The Electrochemical Society* **2004**, *151*, A1690.

(78) Sunarso, J.; Torriero, A. A.; Zhou, W.; Howlett, P. C.; Forsyth, M. *The Journal of Physical Chemistry C* **2012**, *116*, 5827.

(79) Suntivich, J.; Gasteiger, H. A.; Yabuuchi, N.; Nakanishi, H.; Goodenough, J. B.; Shao-Horn, Y. *Nat Chem* **2011**, *3*, 546.

(80) Bard, A. J.; Faulkner, L. R. *Electrochemical methods: fundamentals and applications*; Wiley New York, 1980; Vol. 2.

(81) Carmo, M.; Fritz, D. L.; Mergel, J.; Stolten, D. *International Journal of Hydrogen Energy* **2013**, *38*, 4901.

(82) Pentland, N.; Bockris, J. O. M.; Sheldon, E. *Journal of The Electrochemical Society* **1957**, *104*, 182.

(83) Chen, Z.; Cummins, D.; Reinecke, B. N.; Clark, E.; Sunkara, M. K.; Jaramillo, T. F. *Nano Letters* **2011**, *11*, 4168.

(84) Sheng, W.; Gasteiger, H. A.; Shao-Horn, Y. *Journal of The Electrochemical Society* **2010**, *157*, B1529.

(85) Nørskov, J. K.; Bligaard, T.; Logadottir, A.; Kitchin, J. R.; Chen, J. G.; Pandelov, S.; Stimming, U. *Journal of The Electrochemical Society* **2005**, *152*, J23.

(86) Greeley, J.; Jaramillo, T. F.; Bonde, J.; Chorkendorff, I.; Norskov, J. K. *Nat Mater* **2006**, *5*, 909.

(87) Jaramillo, T. F.; Jørgensen, K. P.; Bonde, J.; Nielsen, J. H.; Horch, S.; Chorkendorff, I. *Science* **2007**, *317*, 100.

(88) Skulason, E.; Karlberg, G. S.; Rossmeisl, J.; Bligaard, T.; Greeley, J.; Jonsson, H.; Norskov, J. K. *Physical Chemistry Chemical Physics* **2007**, *9*, 3241.

(89) Stamenkovic, V. R.; Mun, B. S.; Arenz, M.; Mayrhofer, K. J. J.; Lucas, C. A.; Wang, G.; Ross, P. N.; Markovic, N. M. *Nat Mater* **2007**, *6*, 241.

(90) Skúlason, E.; Tripkovic, V.; Björketun, M. E.; Gudmundsdóttir, S. d.; Karlberg, G.; Rossmeisl, J.; Bligaard, T.; Jónsson, H.; Nørskov, J. K. *The Journal of Physical Chemistry C* **2010**, *114*, 18182.

(91) Esposito, D. V.; Hunt, S. T.; Stottlemyer, A. L.; Dobson, K. D.; McCandless, B. E.; Birkmire, R. W.; Chen, J. G. *Angewandte Chemie International Edition* **2010**, *49*, 9859.

(92) Cheng, F.; Chen, J. *Chemical Society Reviews* **2012**, *41*, 2172.

(93) McKone, J. R.; Sadtler, B. F.; Werlang, C. A.; Lewis, N. S.; Gray, H. B. *ACS Catalysis* **2012**, *3*, 166.

(94) Hinnemann, B.; Moses, P. G.; Bonde, J.; Jørgensen, K. P.; Nielsen, J. H.; Horch, S.; Chorkendorff, I.; Nørskov, J. K. *J. Am. Chem. Soc.* **2005**, *127*, 5308.

(95) Bonde, J.; Moses, P. G.; Jaramillo, T. F.; Norskov, J. K.; Chorkendorff, I. *Faraday Discussions* **2009**, *140*, 219.

(96) Li, Y.; Wang, H.; Xie, L.; Liang, Y.; Hong, G.; Dai, H. *J. Am. Chem. Soc.* **2011**, *133*, 7296.

(97) Lukowski, M. A.; Daniel, A. S.; Meng, F.; Forticaux, A.; Li, L.; Jin, S. *J. Am. Chem. Soc.* **2013**, *135*, 10274.

(98) Benck, J. D.; Chen, Z.; Kuritzky, L. Y.; Forman, A. J.; Jaramillo, T. F. *ACS Catalysis* **2012**, *2*, 1916.

(99) Kong, D.; Wang, H.; Cha, J. J.; Pasta, M.; Koski, K. J.; Yao, J.; Cui, Y. *Nano Letters* **2013**, *13*, 1341.

(100) Eijsbouts, S.; Heinerman, J. J. L.; Elzerman, H. J. W. *Applied Catalysis A: General* **1993**, *105*, 53.

(101) Appel, A. M.; DuBois, D. L.; Rakowski DuBois, M. *J. Am. Chem. Soc.* **2005**, *127*, 12717.

(102) Jaramillo, T. F.; Bonde, J.; Zhang, J.; Ooi, B.-L.; Andersson, K.; Ulstrup, J.; Chorkendorff, I. *The Journal of Physical Chemistry C* **2008**, *112*, 17492.

(103) Vrubel, H.; Hu, X. *Angewandte Chemie International Edition* **2012**, *51*, 12703.

(104) Chen, W. F.; Wang, C. H.; Sasaki, K.; Marinkovic, N.; Xu, W.; Muckerman, J. T.; Zhu, Y.; Adzic, R. R. *Energy & Environmental Science* **2013**, *6*, 943.

(105) Chen, W.-F.; Sasaki, K.; Ma, C.; Frenkel, A. I.; Marinkovic, N.; Muckerman, J. T.; Zhu, Y.; Adzic, R. R. *Angewandte Chemie International Edition* **2012**, *51*, 6131.

(106) Popczun, E. J.; McKone, J. R.; Read, C. G.; Biacchi, A. J.; Wiltrout, A. M.; Lewis, N. S.; Schaak, R. E. *J. Am. Chem. Soc.* **2013**, *135*, 9267.

(107) Cao, B.; Veith, G. M.; Diaz, R. E.; Liu, J.; Stach, E. A.; Adzic, R. R.; Khalifah, P. G. *Angewandte Chemie* **2013**, *125*, 10953.

(108) Cao, B.; Veith, G. M.; Neuefeind, J. C.; Adzic, R. R.; Khalifah, P. G. *J. Am. Chem. Soc.* **2013**, *135*, 19186.

(109) Stamenkovic, V.; Mun, B. S.; Mayrhofer, K. J. J.; Ross, P. N.; Markovic, N. M.; Rossmeisl, J.; Greeley, J.; Norskov, J. K. *Angew. Chem.-Int. Edit.* **2006**, *45*, 2897.

(110) Stamenkovic, V.; Mun, B. S.; Mayrhofer, K. J. J.; Ross, P. N.; Markovic, N. M.; Rossmeisl, J.; Greeley, J.; Nørskov, J. K. *Angewandte Chemie International Edition* **2006**, *45*, 2897.

(111) Wang, H.; Liang, Y.; Li, Y.; Dai, H. *Angewandte Chemie International Edition* **2011**, *50*, 10969.

(112) Liu, R.; von Malotki, C.; Arnold, L.; Koshino, N.; Higashimura, H.; Baumgarten, M.; Müllen, K. *J. Am. Chem. Soc.* **2011**, *133*, 10372.

(113) Jaouen, F. d. r.; Herranz, J.; Lefèvre, M.; Dodelet, J.-P.; Kramm, U. I.; Herrmann, I.; Bogdanoff, P.; Maruyama, J.; Nagaoka, T.; Garsuch, A.; Dahn, J. R.; Olson, T.; Pylypenko, S.; Atanassov, P.; Ustinov, E. A. *ACS Appl. Mater. Interfaces* **2009**, *1*, 1623.

(114) Wu, G.; More, K. L.; Johnston, C. M.; Zelenay, P. *Science* **2011**, *332*, 443.

(115) Ham, D.; Lee, J. *Energies* **2009**, *2*, 873.

(116) Xia, D.; Liu, S.; Wang, Z.; Chen, G.; Zhang, L.; Zhang, L.; Hui, S.; Zhang, J. *J. Power Sources* **2008**, *177*, 296.

(117) Doi, S.; Ishihara, A.; Mitsushima, S.; Kamiya, N.; Ota, K.-i. *Journal of The Electrochemical Society* **2007**, *154*, B362.

(118) Ishihara, A.; Lee, K.; Doi, S.; Mitsushima, S.; Kamiya, N.; Hara, M.; Domen, K.; Fukuda, K.; Ota, K.-i. *Electrochemical and Solid-State Letters* **2005**, *8*, A201.

(119) Ando, T.; Izhar, S.; Tominaga, H.; Nagai, M. *Electrochimica Acta* **2010**, *55*, 2614.

(120) Chisaka, M.; Suzuki, Y.; Iijima, T.; Sakurai, Y. *The Journal of Physical Chemistry C* **2011**, *115*, 20610.

(121) Yu, C. C.; Ramanathan, S.; Oyama, S. T. *J. Catal.* **1998**, *173*, 1.

(122) Ravel, B.; Newville, M. *J. Synchrot. Radiat.* **2005**, *12*, 537.

(123) Suntivich, J.; Gasteiger, H. A.; Yabuuchi, N.; Shao-Horn, Y. *Journal of The Electrochemical Society* **2010**, *157*, B1263.

(124) Li, N.; Wang, X.; Derrouiche, S.; Haller, G. L.; Pfefferle, L. D. *ACS Nano* **2010**, *4*, 1759.

(125) Rodriguez, J. A.; Chaturvedi, S.; Hanson, J. C.; Albornoz, A.; Brito, J. L. *The Journal of Physical Chemistry B* **1998**, *102*, 1347.

(126) Hada, K.; Nagai, M.; Omi, S. *The Journal of Physical Chemistry B* **2001**, *105*, 4084.

(127) Wang, B. *J. Power Sources* **2005**, *152*, 1.

(128) Ishihara, A.; Doi, S.; Mitsushima, S.; Ota, K.-i. *Electrochimica Acta* **2008**, *53*, 5442.

(129) Othman, R.; Dicks, A. L.; Zhu, Z. *International Journal of Hydrogen Energy* **2012**, *37*, 357.

(130) Avasarala, B.; Murray, T.; Li, W.; Haldar, P. *Journal of Materials Chemistry* **2009**, *19*, 1803.

(131) Qi, J.; Jiang, L.; Jiang, Q.; Wang, S.; Sun, G. *The Journal of Physical Chemistry C* **2010**, *114*, 18159.

(132) Ganin, A. Y.; Kienle, L.; Vajenine, G. V. *Journal of Solid State Chemistry* **2006**, *179*, 2339.

(133) Marchand, R.; Tessier, F.; J. DiSalvo, F. *Journal of Materials Chemistry* **1999**, *9*, 297.

(134) Bem, D. S.; Olsen, H. P.; zur Loye, H.-C. *Chemistry of Materials* **1995**, *7*, 1824.

(135) Pourbaix, M. *Atlas of electrochemical equilibria in aqueous solutions*; Pergamon Press: Oxford; New York, 1966.

(136) Kojima, R.; Aika, K.-i. *Applied Catalysis A: General* **2001**, *219*, 141.

(137) Bull, C. L.; Kawashima, T.; McMillan, P. F.; Machon, D.; Shebanova, O.; Daisenberger, D.; Soignard, E.; Takayama-Muromachi, E.; Chapon, L. C. *Journal of Solid State Chemistry* **2006**, *179*, 1762.

(138) Sayag, C.; Bugli, G.; Havil, P.; DjegaMariadassou, G. *J. Catal.* **1997**, *167*, 372.

(139) Lengauer, W. *Journal of Crystal Growth* **1988**, *87*, 295.

(140) Bull, C. L.; McMillan, P. F.; Soignard, E.; Leinenweber, K. *Journal of Solid State Chemistry* **2004**, *177*, 1488.

(141) Bezinge, A.; Yvon, K.; Muller, J.; Lengaeur, W.; Ettmayer, P. *Solid state communications* **1987**, *63*, 141.

(142) Jehn, H. In *Mo Molybdenum*; Springer: 1989, p 1.

(143) Leineweber, A.; Mittemeijer, E. *Advances in X-ray Analysis* **2003**, *46*, 43.

(144) Bem, D. S.; Lampe-Önnerud, C. M.; Olsen, H. P.; zur Loye, H.-C. *Inorganic Chemistry* **1996**, *35*, 581.

(145) Giordano, C.; Erpen, C.; Yao, W.; Antonietti, M. *Nano Letters* **2008**, *8*, 4659.

(146) Inumaru, K.; Baba, K.; Yamanaka, S. *Physica B: Condensed Matter* **2006**, *383*, 84.

(147) Kawashima, T.; Takayama-Muromachi, E.; McMillan, P. F. *Physica C: Superconductivity* **2007**, *460*, 651.

(148) Gajbhiye, N.; Ningthoujam, R. *physica status solidi (c)* **2004**, *1*, 3449.

(149) Kanoun, M.; Goumri-Said, S.; Jaouen, M. *Physical Review B* **2007**, *76*, 134109.

(150) Papaconstantopoulos, D.; Pickett, W.; Klein, B.; Boyer, L. *Physical Review B* **1985**, *31*, 752.

(151) Walter, M. G.; Warren, E. L.; McKone, J. R.; Boettcher, S. W.; Mi, Q.; Santori, E. A.; Lewis, N. S. *Chemical Reviews* **2010**, *110*, 6446.

(152) Lewis, N. S.; Nocera, D. G. *Proceedings of the National Academy of Sciences* **2006**, *103*, 15729.

(153) Holladay, J. D.; Hu, J.; King, D. L.; Wang, Y. *Catal. Today* **2009**, *139*, 244.

(154) Subbaraman, R.; Tripkovic, D.; Strmcnik, D.; Chang, K.-C.; Uchimura, M.; Paulikas, A. P.; Stamenkovic, V.; Markovic, N. M. *Science* **2011**, *334*, 1256.

(155) Bhattacharyya, S.; Kurian, S.; Shivaprasad, S. M.; Gajbhiye, N. S. *Journal of Nanoparticle Research* **2010**, *12*, 1107.

(156) Shannon, R. *Acta Crystallographica Section A* **1976**, *32*, 751.

(157) Elder, S. H.; Doerrer, L. H.; DiSalvo, F. J.; Parise, J. B.; Guyomard, D.; Tarascon, J. M. *Chemistry of Materials* **1992**, *4*, 928.

(158) McIntyre, N. S.; Cook, M. G. *Analytical Chemistry* **1975**, *47*, 2208.

(159) Inoue, H.; Wang, J. X.; Sasaki, K.; Adzic, R. R. *Journal of Electroanalytical Chemistry* **2003**, *554–555*, 77.

(160) Vrubel, H.; Hu, X. *Angewandte Chemie* **2012**, *124*, 12875.

(161) Nishijima, M.; Takeda, Y.; Imanishi, N.; Yamamoto, O.; Takano, M. *Journal of Solid State Chemistry* **1994**, *113*, 205.

(162) Houmes, J. D.; Deo, S.; zur Loye, H.-C. *Journal of Solid State Chemistry* **1997**, *131*, 374.

(163) Brese, N. E.; O'Keeffe, M. *Acta Crystallographica Section B* **1991**, *47*, 192.

(164) Miura, A.; Wen, X.-D.; Abe, H.; Yau, G.; DiSalvo, F. J. *Journal of Solid State Chemistry* **2010**, *183*, 327.

(165) Chhina, H.; Campbell, S.; Kesler, O. *J. Power Sources* **2008**, *179*, 50.